Vol. 5 No. II Tahun 2022

P-ISSN : 2621-0215
E-ISSN : 2621-489X

Al-Fiziya

Journal of Materials Science, Geophysics, Instrumentation and Theoretical Physics

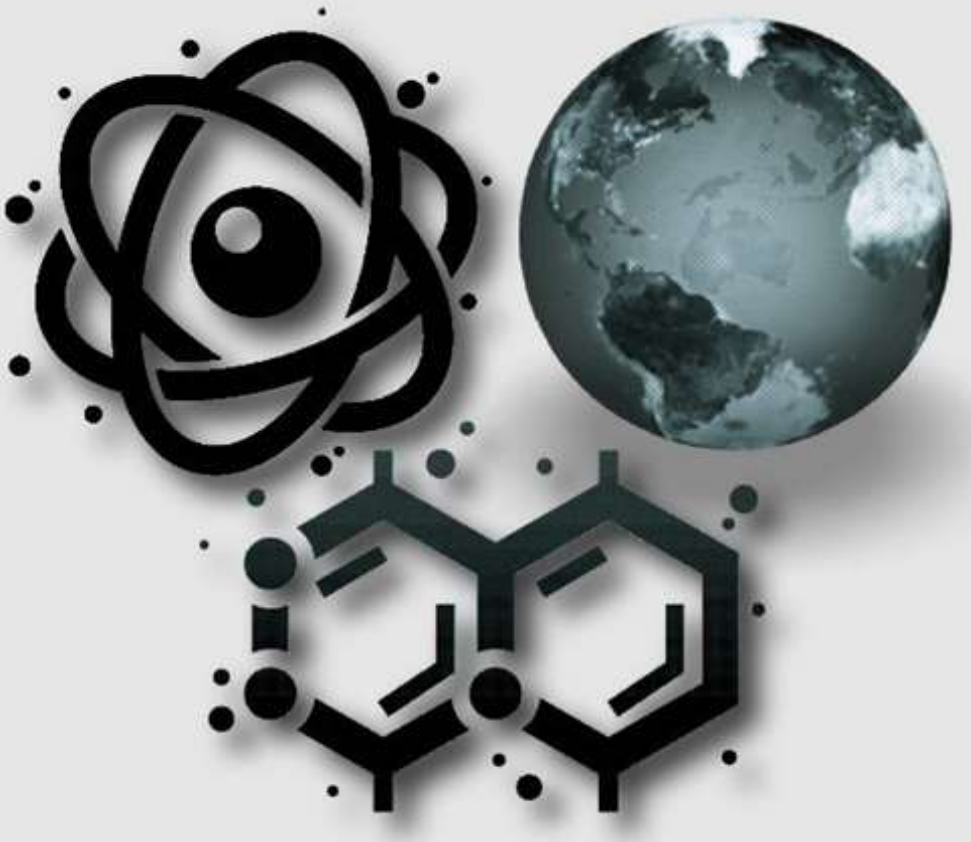

Published by
Program Studi Fisika
Fakultas Sains dan Teknologi
Universitas Islam Negeri Syarif Hidayatullah Jakarta

AL-FIZIYA:

Journal of Materials Science, Geophysics, Instrumentation, and Theoretical Physics

Vol. 5, No. II, Tahun 2022

EDITORIAL IN CHIEF
Dr. Sitti Ahmiatri Saptari

MANAGING EDITOR
Muhammad Nafian, M.Si

REVIEWER
Sabar
Melany Febrina
Abdul Harris
Agus Riyanto
Yusuf Wicaksono
Deni Khaerudini
Muhammad Aziz Majidi
Adam Badra Cahaya
Imam Wahyutama
Eng. Supriyanto, M.Si.
Rina Dwi Inndriana
Ikhwan Nur Rahman
Erina Hertati
Suharno
Eni Sugiarti

SECTION EDITOR
Elvan Yuniarti, M.Si.
Ambran Hartono, M.Si.
Biaunik Niski Kumila, M.Sc.
Praditiyo Ryadi, M.Si

LAYOUT EDITOR
Ryan Rizaldy, M.Si.

Alamat Redaksi
Gedung Fakultas Sains dan Teknologi Lt. 3
Jl. Ir. H Juanda No.95 Ciputat 15412 Tangerang
Telp. (6221)743731, (6221)7493315
Email: al-fiziya@uinjkt.ac.id

Published by
Program Studi Fisika, Fakultas Sains dan Teknologi
Universitas Islam Negeri Syarif Hidayatullah Jakarta

PENGANTAR REDAKSI

Assalamu'alaikum, Wr. Wb.

Puji Syukur kita panjatkan kehadirat Allah SWT, dengan terbitnya Al-Fiziya: Journal of Materials Science, Geophysics, Instrumentation, and Theoretical Physics Vol 5, No. II, Tahun 2022 dengan nomor ISSN: 2621-0215 dan E-ISSN: 2621-489X sebagai jurnal penelitian dan pengembangan ilmu fisika yang diterbitkan oleh Program Studi Fisika Fakultas Sains dan Teknologi UIN Syarif Hidayatullah Jakarta. Jurnal ini menyajikan artikel-artikel penelitian dan pengembangan terkini baik dalam Bahasa Indonesia maupun Bahasa Inggris di bidang fisika murni dan terapan, antara lain bidang fisika material, geofisika, fisika instrumentasi, dan fisika teori. Jurnal ini merupakan sarana publikasi bagi dosen dan para peneliti yang bergerak di bidang penelitian dan pengembangan ilmu fisika. Dengan demikian, melalui penerbitan jurnal ini kami memberikan kesempatan seluas-luasnya bagi siapapun yang ingi berpartisipasi dalam menyampaikan buah pikirannya melalui tulisan atau artikel yang akan kami muat pada edisi berikutnya.

Artikel yang masuk akan melalui proses seleksi oleh dewan editor dan *review* yang melibatkan mitra bestari baik dari para dosen ahli dibidangnya berdasarkan kesesuaian isi dan bobot karya ilmiah. Untuk informasi lengkap submit dan tata cara penulisan dalam Al-Fiziya: *Journal of Material Science, Geophysics, Instrumentation, and heoretical Physics* dapat dilihat pada pedoman penulisan artikel di halaman akhir penerbitan atau dapat mengakses website kami di http://journal.uinjkt.ac.id/index.php/al-fiziya. Atas nama dewan redaksi, kami mengucapkan terimakasih atas dukungan dan partisipasi dari semua pihak hingga terbitnya Al-Fiziya: *Journal of Materials Science, Geophysics, Instrumentation, and Theoretical Physics.*

Editorial in chief
SITTI AHMIATRI SAPTARI

Daftar Isi

Vol. 5, No. II Tahun 2022

Available online at:
Al-Fiziya: Journal of Materials Science, Geophysics, Instrumentation and Theoretical Physics
Website: http://journal.uinjkt.ac.id/index.php/al-fiziya
Vol.5 No. II Tahun 2022, 77 - 86

Identification of Iron Ore Deposit in Sub-Surface using Resistivity and Induced Polarization Methods at Sarakaman, Sebuku Island, South Kalimantan

Merry Nur Rakhmawati [1,†], Sutrisno [1], Yanto Sudiyanto[2], Wahyu Hidayat[2]

[1]Physics Study Program, Faculty of Sciences and Technology, State Islamic University Syarif Hidayatullah Jakarta, Ir. H. Djuanda Street No.95, Cempaka Putih, Ciputat, South Tangerang, Banten 15412, Indonesia
[2]Center for Mineral Resources Development Technology (PTPSM) of the Agency for the Assessment and Application of Technology Indonesia (BPPT), Puspiptek Area Street, Muncul, Setu, South Tangerang, Banten 15314, Indonesia

[†]merry.nur16@mhs.uinjkt.ac.id

Submitted: Agustus 2022; Revised: September 2022; Approved: Oktober 2022; Available Online: Desember 2022

Abstract. Iron is the second most abundant metal on earth. Sebuku Island is one of the areas in Indonesia that has potential for laterite iron ore. This study aims to detect the presence of mineralized zones and estimate the volume of iron ore. Therefore, geophysical research was carried out using the resistivity method and the Induced Polarization methods with the Wenner-Schlumberger configuration. The research was carried out in 4 paths along 475 m with a space between the electrodes of 5 meters. Based on modeling, 20 iron ore deposits were found in the study area on all trajectories characterized by high chargeability values ranging from 251,55 – 810,55 ms which correlated with low resistivity values of 4,02 – 124,41 m. Then it was found that the direction of the distribution of iron ore deposits in the study area was north-south and there was no continuous zone of iron ore deposits due to the long distance of the path. The amount of deposits of iron ore in the study area in an area of ±39 hectares is approximated to be around 1.807.614 m3 with total reserves of iron ore deposits of 7.230.456 tons.

Keywords: *Induced Polarization (IP), Iron Ore, Resistivity, Sebuku, Wenner-Schlumberger.*
DOI : *10.15408/fiziya.v5i2.25648*

INTRODUCTION

Based on data from the Geological Agency as of the end of 2014, the largest iron ore reserves in Indonesia were in South Kalimantan Province, amounting to 480.698.847 tons [1]. Geophysics is a science that plays an important role in interpreting the distribution of iron ore minerals and other metal ores under the earth's surface, one of which is using the geoelectrical resistivity method and Induced Polarization (IP) method which is the development of the resistivity geoelectric method.

Iron (Fe) is the second most abundant metal on earth. Rock with iron or iron deposits is known as iron ore. The character of iron deposits can be in the form of metal

Copyright©2019, Published by **Al-Fiziya: Journal of Materials Science, Geophysics, Instrumentation and Theoretical Physics**
P-ISSN: 2621-0215, E-ISSN: 2621-489X

deposits that stand alone but are often associated with other metal minerals [2]. Iron ore deposits can occur either initially or laterally. Magmatic, contact metasomatic, and hydrothermal processes can all contribute to the formation of the iron ore primary deposit. Additionally, secondary deposits are caused by the processes of weathering, transportation, and sedimentation [3]. Economical deposits are generally magnetite, hematite, limonite, and siderite [4]. Resistivity method is one of the geophysical methods used to investigate subsurface conditions. Work principle of the resistivity method is to flow an electric current into the earth through two current electrodes, then measure the potential distribution formed through two potential electrodes [5]. Geoelectric measurements are carried out by injecting electric current (I) into the earth through two current electrodes, As indicated in Fig. 1, the potential difference (V) that arises between C1 and C2 is then measured using P1 and P2, two potential electrodes. Equation may be used to derive resistivity value from the collected readings. [6].

$$\rho_a = K\frac{V}{I} \tag{1}$$

where K is a geometric variable that relies on how the four electrodes are arranged. the Wenner-Schlumberger configuration is defined as the ratio of distance between the C1-P1 electrodes (or C2-P2) to the space between the P1-P2 electrodes. This configuration has a set of constant spacing criteria. [12]. The geometric factors of this configuration are:

$$K = \pi n\,(n+1)a \tag{2}$$

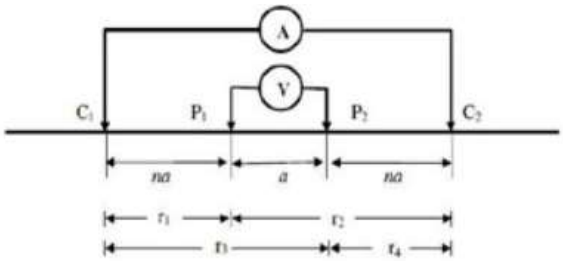

Figure 1. Wenner-Schlumberger Configuration Electrode Arrangement [6].

Induced Polarization (IP)

When a current is introduced and then cut off, the phenomenon of induced polarization takes place. The ions in the granite pores will be dispersed from a stable location to an unstable position when the current is injected. When the current is stopped, the potential difference should instantly be zero, however in some media, since the medium acts like a capacitor and stores electrical energy, the potential difference does not immediately become zero. Overvoltage decay is the gradual approach of the measured potential to zero. Chargeability is the ratio of the voltage when the current is shut off to the voltage when the current is injected [7].

$$M = \frac{1}{Vp}\int_{t1}^{t2} Vs\ (t_1) \tag{5}$$

Result of polarization effect can be caused by membrane polarization and electrode polarization. Membrane polarization is caused by the narrowing of the pores due to the presence of very large negatively charged clay particles causing positive ions in the electrolyte fluid to be attracted towards the negatively charged clay particles. This process creates positive clouds (membranes) on side of rock pores. While the electrode

Vol.5 No. II Tahun 2022, 77 - 86
P-ISSN: 2621-0215, E-ISSN: 2621-489X

polarization is caused by the presence of metallic minerals in the rock that block the flow of current when passing through the rock so that a chemical reaction will occur at the metal mineral boundary area which causes an extra potential or overvoltage [7].

Regional Geology

Sebuku Island is part of the regional geological map sheet Kotabaru, South Kalimantan, where the rock units found in the area consist of ultramafic rocks (Mub), Haruyan Formation (Kvh), Pitap Formation (Ksp), Tanjung Formation (Tet), and alluvium (Qa) deposits [8].

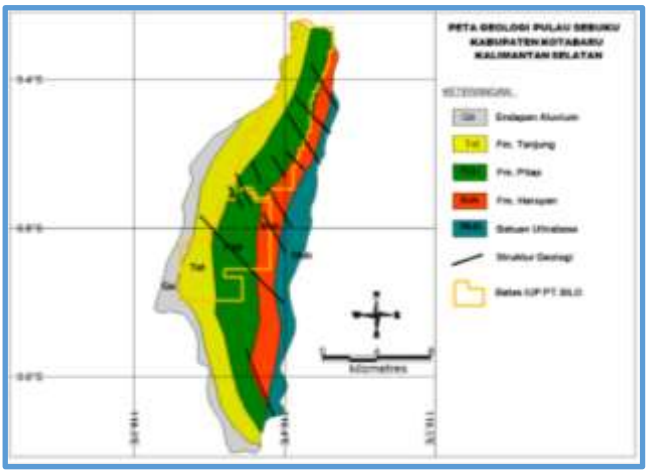

Figure 2. Geology Map of Sebuku Island [9].

Sebuku Island has 3 phases of iron oxide with significant Fe content, namely magnetite, hematite, and goethite. In the research area, the resource that has the potential to contain a lot of Fe is laterite deposits. Laterite deposits are deposits produced by the weathering process of bedrock. In the Serakaman area, generally under lateritic iron ore deposits, there are ultramafic rocks of the type of dunite and harzburgite, so it can be assumed that in this Serakaman area, the bedrock is dominated by ultramafic rocks. The characteristics of iron ore found in the Sebuku Area are as follows, lateritic iron ore deposits, blackish brown-reddish in color, fine sand size-lumps, rather hard, massive, sometimes in the form of lenses and laminates, spreading in a lateral direction almost north-south, the average thickness is approximately 5 m; types of iron ore are dominated by hematite and goethite, in some places there is magnetite; the presence of lateritic iron ore deposits are generally scattered in highland areas on the top soil [9].

METHODS

The research using Sarakaman, Sebuku Island, South Kalimantan using resistivity and IP data with the Wenner-Schulmberger configuration data from Center for Mineral Resources Development Technology (PTPSM-BPPT). In This study consists of 4 tracks, each of which is 475 m long with a space between the electrodes of 5 m and distance between the tracks, namely the L-01 track to the L-02 track along ±138 m, the L-02 track to the L-03 track. along ±160 m and the L-03 track to the L-04 track ±150 m.

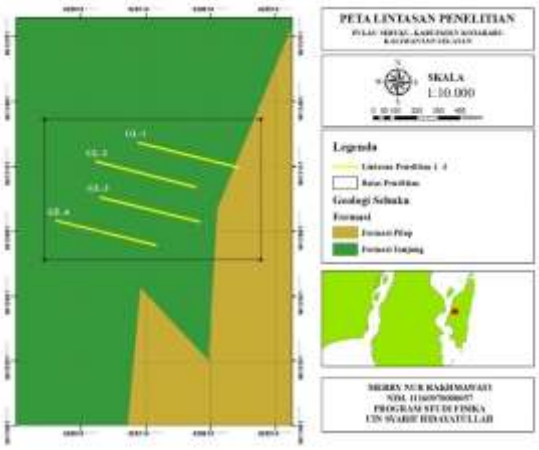

Figure 3. Resistivity and Induced Polarization (IP) Survey Design Map in Sarakaman Area, Sebuku Island, South Kalimantan [9].

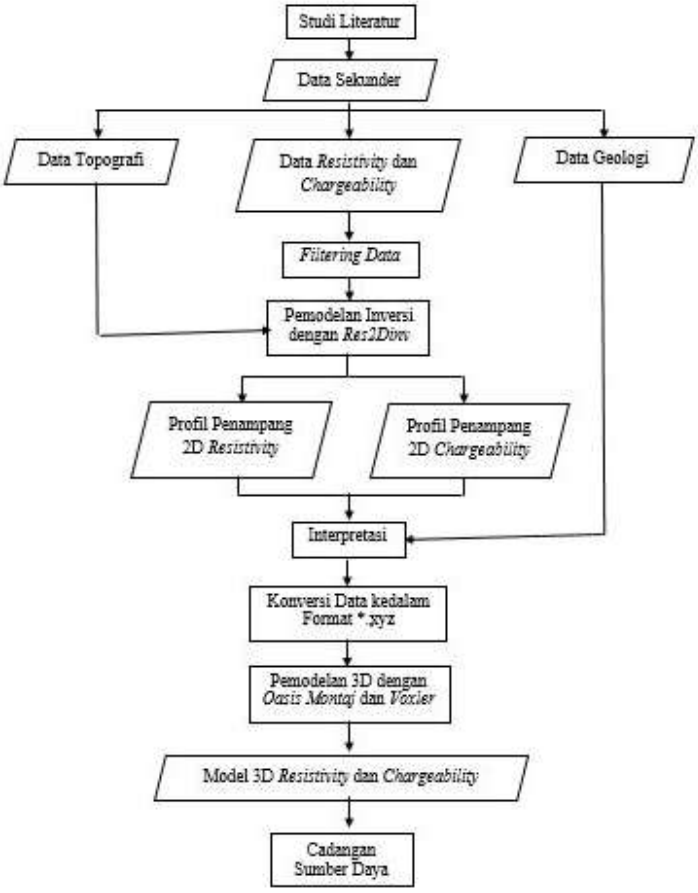

Figure 4. Research Flow Chart

The data obtained is processed and interpretated in 2-Dimensional IP data is carried out by looking at the characteristics or trends in resistivity and chargeability values, which are then correlated with existing geological information. Estimation of the presence of iron ore will be directed at a low resistivity value with a high chargeability value. At 3-Dimensional modeling using Geosoft Oasis Montaj software. It is used to show the distribution of iron ore deposits below the surface and to see whether or not there is a continuity zone for iron ore deposits by correlating the chargeability values of the entire track. Furthermore, Voxler software is used for calculating iron ore resources

in the research area. This calculation utilizes the Isosurface module which is a representation of the distribution of data values in 3D (actual chargeability). Determination of the volume of iron ore deposits is done by entering the smallest chargeability limit value of isovalue. The following is a research flow chart, showed as:

RESULTS AND DISCUSSION

Results and Discussion of 2D Inversion Modeling

The 2D cross-section of resistivity and chargeability from all inversion models is then correlated with the geological data of the research area, then interpretation can be made to indicate the zone of presence of iron ore deposits on each lines, as follows.

Line L-01

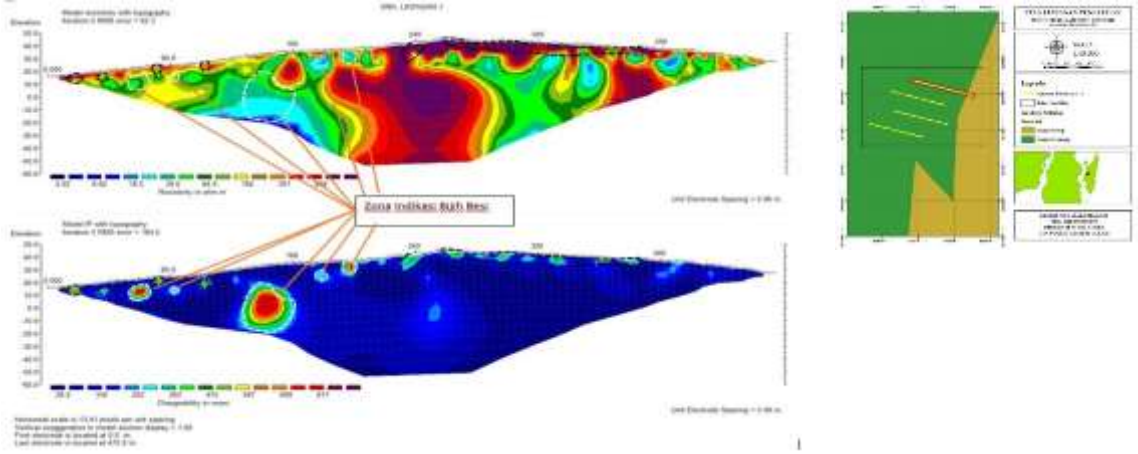

Figure 5. Inversion Model and Interpretation of Resistivity and Chargeability Sections on the Line L-01.

Based on analysis of the image (Fig. 5), the resistivity value obtained on the line L-01 is between 8,26 – 1.226,76 m while the chargeability value is between 27,95 – 810,55 ms. In the 2-Dimensional section of Induced Polarization (IP) data, the chargeability value contrasts with a value range of 251,55 to 810,55 ms, which correlates with a resistivity value range of 8,62 – 124,41 m which is interpreted as iron ore deposits. So it can be seen that on the line L-01 there are 5 iron ore deposits which are marked with white dotted lines.

Table 1. Distribution of Iron Ore Deposits on the Line L-01.

Depth (mdpl)	Length (m)	Resistivity (Ohm m)	Chargeability (ms)	Description
20 – 10	15 – 20	124,41 – 1.226,76	251,55 – 698,75	Anomaly
15 – 10	35 – 40	39,62 – 266,78	251,55 – 363,35	Anomaly
20 – 5	55 – 70	58,01 – 124,41	251,55 – 810,55	Iron Ore
25 – 20	70 – 75	124,41 – 390,66	251,55 – 642,95	Anomaly
10 – 5	80 – 85	84,95 – 124,41	251,55 – 363,35	Iron Ore
20 – 15	100 – 105	124,41 – 390,66	251,55 – 586, 95	Anomaly
20 – (-20)	125 – 160	8,62 – 124,41	251,55 – 810,55	Iron Ore
25 – 20	175 – 180	8,62 – 27,05	251,55 – 363,35	Iron Ore
35 – 25	190 – 200	12,62 – 58,01	251,55 – 754,65	Iron Ore
40 – 25	230 – 245	124,41 – 1.226,76	251,55 – 475,15	Anomaly

40 – 30	255 - 385	124,41 – 1.226,76	251,55 – 475,15	Anomaly

Line L-02

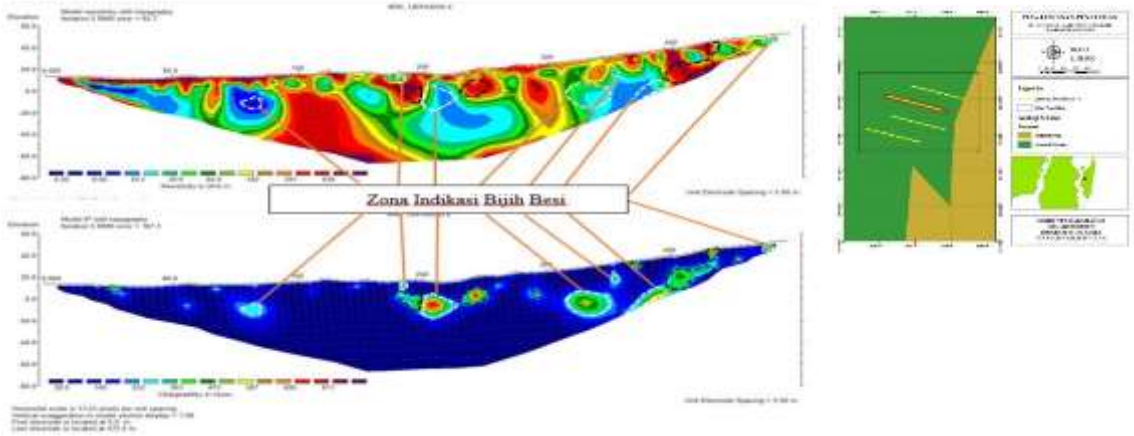

Figure 6. Inversion Model and Interpretation of Resistivity and Chargeability Sections on the Line L-02.

Based on analysis of the image (Fig. 6), the resistivity value obtained on the line L-02 is between 8,62 – 1.226,76 m, while the chargeability value is between 27,95 – 754,65 ms. In the 2-Dimensional section of Induced Polarization (IP) data, the chargeability value contrasts with a value range of 251,55 to 754,65 ms, which is interpreted as an iron ore deposit which is correlated with a resistivity value range of 8,62 – 124,41 m. So it can be seen that on the line L-02 there are 7 iron ore deposits which are marked with white dotted lines.

Table 2. Distribution of Iron Ore Deposits on the Line L-02.

Depth (mdpl)	Length (m)	Resistivity (Ohm.m)	Chargeability (ms)	Description
10 - 5	40 – 45	390,66 – 837,74	251,55 – 586,95	Anomaly
-5 – (-15)	125 – 135	8,62 – 12,62	251,55 – 307,45	Iron Ore
5 – (-10)	220 – 240	390,66 – 1.226,76	251,55 – 531,05	Anomaly
10 – 5	225 – 230	27,05 – 58,01	251,55 – 307,45	Iron Ore
5 – (-15)	240 – 260	12,62 – 124,41	251,55 – 754,65	Iron Ore
10 – (-5)	260 – 280	124,41 – 837,74	251,55 – 754,65	Anomaly
5 – 0	310 – 315	390,66 – 837,74	251,55 – 307,45	Anomaly
0 – (-20)	330 – 355	18,47 – 84,95	251,55 – 586,95	Iron Ore
20 – 10	360 – 365	18,47 – 84,95	251,55 – 363,35	Iron Ore
20 – 15	375 – 380	124,41 – 572,08	251,55 – 586,95	Anomaly
5 – (-15)	365 – 390	12,62 – 84,95	251,55 – 642,85	Iron Ore
20 – 0	395 – 425	124,41 – 1.226,76	251,55 – 475,15	Anomaly
40 – 30	420 – 430	124,41 – 1.226,76	251,55 – 754,65	Anomaly
35 – 30	440 – 445	84,95 – 182,18	251,55 – 307,45	Anomaly
40 – 35	460 – 465	18,47 – 39,62	251,55 – 586,95	Iron Ore

Line L-03

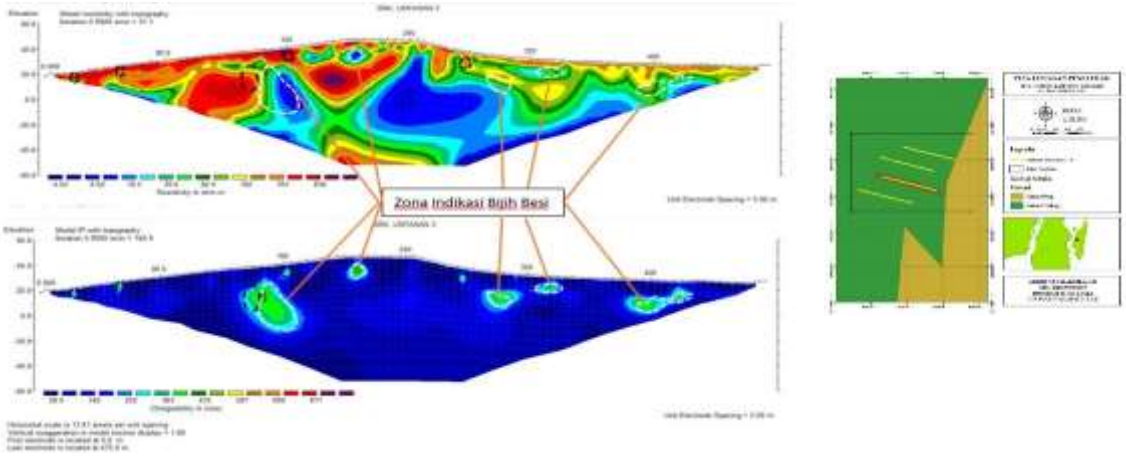

Figure 7. Inversion Model and Interpretation of Resistivity and Chargeability Sections on the Line L-03.

Based on analysis of the image (Fig. 7), the resistivity value obtained on the L-03 path is between 5,88 – 837,34 m while the chargeability value is between 27,95 – 475,15 ms. In the 2-Dimensional section of Induced Polarization (IP) data, the chargeability value contrasts with a value range of 251,55 to 475,15 ms, which is interpreted as an iron ore deposit which is correlated with a resistivity value range of 5,88 – 124,41 m. So it can be seen that on the L-03 line there are 5 iron ore deposits which are marked with white dotted lines.

Table 3. Distribution of Iron Ore Deposits on the Line L-03.

Depth (mdpl)	Length (m)	Resistivity (Ohm.m)	Chargeability (ms)	Description
20 – 15	20 – 25	266,78 – 837,74	251,55 – 363,35	Anomaly
23 – 18	50 – 55	266,78 – 837,74	251,55 – 363,35	Anomaly
20 – 5	125 – 140	124,41 – 572,08	251,55 – 419,25	Anomaly
25 – (-10)	140 – 170	5,88 – 124,41	251,55 – 475,15	Iron Ore
35 – 25	160 – 165	390,66 – 837,34	251,55 – 363,35	Anomaly
40 – 30	200 – 215	5,88 – 27,05	251,55 – 475,15	Iron Ore
20 – 15	275 – 280	124,41 – 182,18	251,55 – 307,45	Anomaly
15 – 5	295 – 310	18,47 – 124,41	251,55 – 419,25	Iron Ore
25 – 15	325 – 340	12,62 – 84,95	251,55 – 363,35	Iron Ore
20 – 0	385 – 425	27,05 – 124,41	251,55 – 419,25	Iron Ore

Line L-04

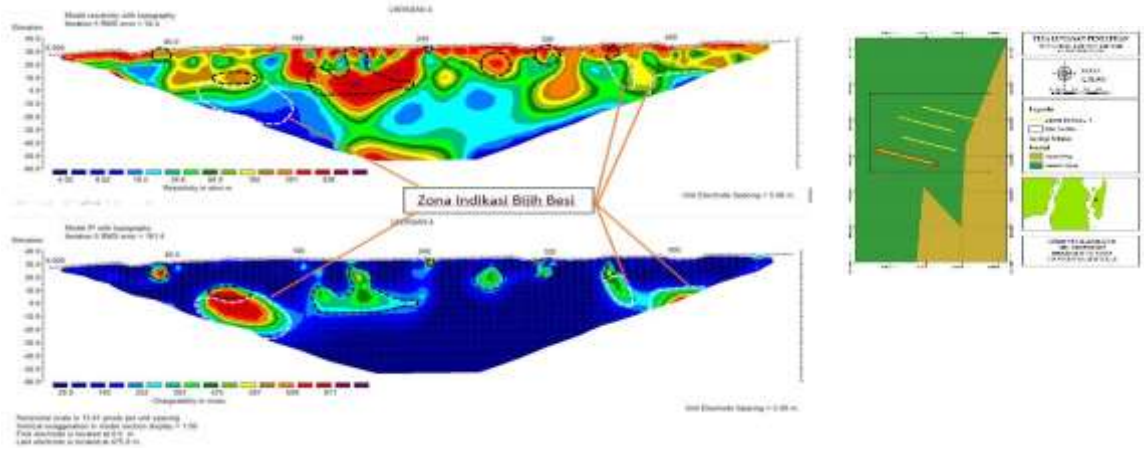

Figure 8. Inversion Model and Interpretation of Resistivity and Chargeability Sections on the Line L-04.

Based on analysis of the image (Fig. 8), the resistivity value obtained on the L-04 path is between 4,02 – 1.226,76 m while the chargeability value is between 27,95 – 810,55 ms. In the 2-Dimensional section of Induced Polarization (IP) data, the chargeability value contrasts with a value range of 251,55 to 810,55 ms, which is interpreted as an iron ore deposit which is correlated with a resistivity value range of 4,02 – 124,41 m. So it can be seen that on the line L-04 there are 3 iron ore deposits which are marked with white dotted lines.

Table 4. Distribution of Iron Ore Deposits on the Line L-04.

Depth (mdpl)	Length (m)	Resistivity (Ohm.m)	Chargeability (ms)	Description
30 – 20	65 – 75	39,62 – 390,66	251,55 – 810,55	Anomaly
5 – (-30)	95 – 155	4,02 – 124,41	251,55 – 810,55	Iron Ore
15 – 5	100 – 130	124,41 – 390,66	251,55 – 810,55	Anomaly
25 – (-5)	165 – 235	39,62 – 1226,76	251,55 – 586,95	Anomaly
35 – 30	240 - 245	124,41 – 390,66	251,55 – 698,75	Anomaly
30 – 10	270 – 290	124,41 – 572,08	251,55 – 531,05	Anomaly
30 – 20	310 – 325	39,62 – 837,34	251,55 – 586,95	Anomaly
30 - 20	350 - 360	182,18 – 387,74	251,55 – 586,95	Anomaly
20 – (-5)	350 – 370	27,05 – 124,41	251,55 – 475,15	Iron Ore
10 – (-10)	385 - 420	12,62 – 124,41	251,55 – 698,75	Iron Ore

Based on tables 1 – 4, it can be seen that there are high resistivity anomalies in line L-01 – L-04 which are resistive, they have values ranging from 124,41 m to 1.226,76 m and are not interpreted as resistivity values. iron ore minerals, because theoretically metal ore minerals including iron ore are conductors which have low resistivity values, especially in massive iron ores, not as fragments in other rock matrices. In conditions where high resistivity values are estimated to occur due to the presence of cavities

between fragments and iron ore fragments filled with air. And, generally iron ore in this area is dominated by hematite iron ore.

Distribution of Subsurface Iron Ore Deposits

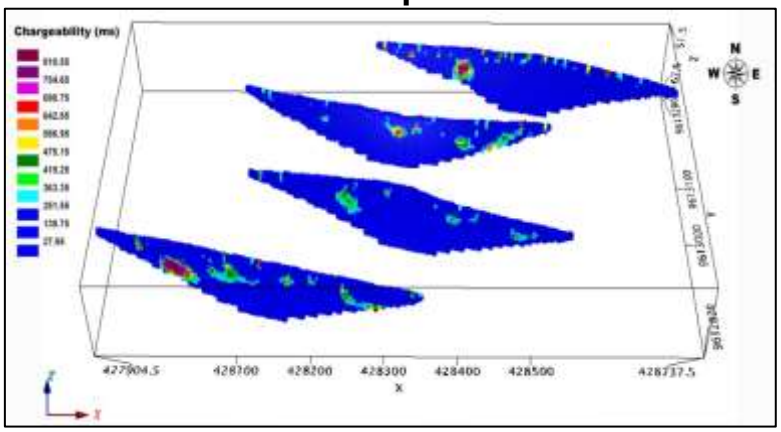

Figure 9. 3D Model from Correlation of Chargeability Inversion Results of All Lines.

Based on the correlation of the IP (chargeability) values in the form of a 3D model (Fig. 9), iron ore deposits are scattered in certain locations in the form of iron ore fragments in a matrix of dunite and harzburgite ultramafic rocks and in the form of iron ore chunks with a north-south direction. And, there is also no continuous zone of iron ore deposits found. This is because the distance between the tracks is quite far, namely the L-01 track to the L-02 track along ±138 m, the L-02 track to the L-03 track ±160 m and the L-03 track to the L-04 track ±150 m.

Calculation of Iron Ore Resources

The volume of the iron ore deposits zone, which has a chargeability value of 251,55 ms in the research region within an area of around ±39 hectares, is estimated to be roughly 1.807.614 m3 based on (Fig.11), the findings of 3D isosurface modeling using Voxler software. The mass estimated reserves of ore deposits in a region of around ±39 hectares are given if the iron ore density is considered to be 4 g/cm3

Mass = volume x density
= 1.807.614 m^3 x 4.000 kg/m^3
= 7.230.456 tons

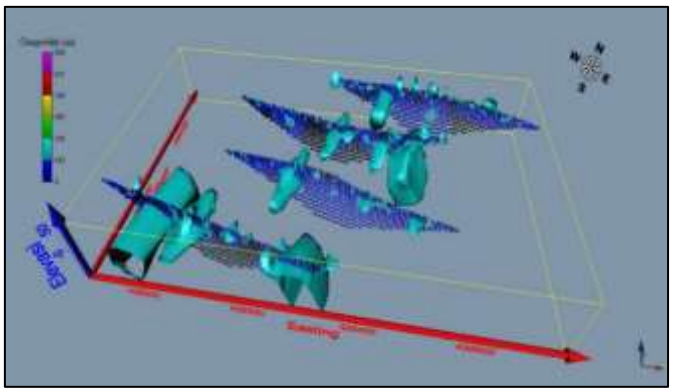

Figure 10. Distribution of Iron Ore Deposits.

CONCLUSIONS

Based on the results and discussion, it can be concluded that the distribution of the resistivity value and the chargeability value below the surface is, the L-01 track with a resistivity value of 4,02 – 1.266,76 m and chargeability value of 27,95 – 810,55 ms. The L-02 track has a resistivity value of 8,62 – 1.226,76 m and a chargeability value of 27,95 – 754,65 ms. The L-03 track has a resistivity value of 5,88 – 837,34 m and a chargeability value of 27,95 – 475,15 ms. The L-04 track has a resistivity value of 4.02 – 1.226,76 m and a chargeability value of 27,95 – 810,55 ms. Iron ore deposits in the study area were found on all tracks, namely at L-01 as many as 5 deposits, L-02 as many as 7 deposits, L-03 as many as 5 deposits, and L-04 as many as 3 deposits based on a low resistivity value of 124,41 m and a high chargeability value of 251,55 ms. The distribution of iron ore deposits in the study area is in a north-south direction and no continuity zone for iron ore deposits is found due to the long distance between the trajectories. The resource of iron ore deposits in the research area with an area of ±39 hectares is 7.230.456 tons which is dominated by hematite iron ore.

REFERENCES

[1] ESDM. (2015). *Dampak Pembatasan Ekspor Bijih Besi Terhadap Penerimaan Sektor ESDM dan Perekonomian_Nasional*. Pusat data dan teknologi informasi energi dan sumber daya mineral.

[2] Ferial, D., Natalisanto, A., & Lazar, P. (2019). Identifikasi Sebaran Mineral Bijih Besi Dengan Menggunakan Metode Resistivitas dan Induced Polarizatiom di Kecamatan Muara Uya, Kabupaten Tabalong, Provinsi Kalimantan Selatan. *Jurnal Geosains Kutai Basin Vol. 2 No. 2*.

[3] Sudiyanto, Y. (2010). Pemodelan 3 Dimensi Endapan Bijih Besi Menggunakan Metode Resistivity dan Induced Polarization (IP)" Tesis S2 Jurusan Fisika Fakultas Matematika dan Ilmu Pengetahuan Alam Universitas Indonesia.

[4] Karyanto, N. H., Iskandar, & Rohima. (2009). Studi Tahanan Jenis Batuan Untuk Idntifikasi Mineral Bijih Besi di Tegineneng Limau Tanggamus. *Sains MIPA Vol. 15 No. 1*, 51-58.

[5] Hendrajaya, L., & Arif. (1990). *Geolistrik Tahanan Jenis. Monograf Metode Eksplorasi*. Bandung: Laboratorium Fisika Bumi ITB.

[6] Loke, M. (2000). *Electrical imaging survey for environmental and engineering Studies. A practical guide to 2D and 3D survey*.

[7] Kearey, P., Michael, Brooks, & Hill, l. (2002). *An Introduction Geophysical Eploration Third Edition*. Blackwell Science Ltd.

[8] Ristandi, Nila, P., Sanyoto, & Margono. (1995). *Peta Geologi Lembar Kotabaru, Kalimantan Selatan*. Bandung: Pusat Penelitian dan Pengembangan Geologi (P3G), Ditjen Geologi dan SDM.

[9] BPPT, T. (2015). *Hasil Survei Metode Geolistrik dan IP di Daerah Sarakaman, Pulau Sebuku, Kalimantan Selatan*. Tangerang Selatan: BPPT.

Available online at:
Al-Fiziya: Journal of Materials Science, Geophysics, Instrumentation and Theoretical Physics
Website: http://journal.uinjkt.ac.id/index.php/al-fiziya
Vol.5 No. II Tahun 2022, 87 - 94

Utilization of Lightning Energy As a Lightning Power Plant to Optimize Lightning Potential in Medan City

Rizky Agassy Sihombing[1,†], Jennie Febrina Hutagalung[1], Jenita Tambunan[1]

[1]Natural Science Education Study Program, Faculty of Mathematics and Natural Sciences, State University of Medan, Indonesia

[†]rizkyagassy@mhs.unimed.ac.id

Submitted: Agustus 2022; Revised: September 2022; Approved: Oktober 2022; Available Online: Desember 2022

Abstract. In addition to solar, wind, and water waves, there are other sources of energy that are renewable. Researchers are currently testing the use of these energies with a device that can draw electricity from the air. The new energy is electricity in the air that triggers the formation of lightning & lightning. The need for electrical energy is increasing day by day. Electrical energy supply in Indonesia itself is usually supplied from power plants such as Hydroelectric Power (PLTA), Air (PLTU), Solar (PLTS), Diesel (PLTD), and Geothermal (PLTG) whose existence still does not meet electricity needs. The type of research used is descriptive qualitative research by literature study use 10 journals. The purpose of this work is to utilize lightning as an energy source in order to maximize the potential of Indonesia's natural resources, especially in the city of Medan. The results show that lightning can be used as an alternative energy source, because lightning is a renewable energy and will not run out even if it is used continuously.

Keywords: *Lightning, Potential, Power Generation, Energy*

DOI : *10.15408/fiziya.v5i2.25926*

INTRODUCTION

The need for electrical energy is increasing every day. Electrical energy supply in Indonesia itself is usually supplied from power plants such as Hydroelectric Power Plant (PLTA), Air (PLTU), Solar (PLTS), Diesel (PLTD), and Geothermal (PLTG) whose existence still does not meet electricity needs. Country. Based on data quoted from events that occurred in North Sumatra, the community must be harmed because of rotating power cuts that take up to 4 hours every day. The reason is the electricity deficit which reaches 400MW. This is due to the growth in the number of electricity users reaching 15% while the planned development is only 7.5%.

Copyright©2019, Published by **Al-Fiziya: Journal of Materials Science, Geophysics, Instrumentation and Theoretical Physics**
P-ISSN: 2621-0215, E-ISSN: 2621-489X

Based on the above problems, it is necessary to have alternative electrical energy to meet the electricity needs in an area. In addition to solar, wind, and water waves, there are other sources of energy that are renewable. The alternative energy source comes from lightning. Lightning is a common natural occurrence during the rainy season when the sky emits a brief burst of dazzling light. after that, there was a thundering roar. Lightning occurs due to a jump in static electricity in the ionosphere. Electric charge jumps occur when electric charges move together. This event is called discharge of static electricity. The emptying was indicated by a lightning strike. Electric charge can be dissipated by discharging. Discharge occurs when there is a way for electrons to flow from one charged object to another. The transfer of static electric charge from one object to another is called neutralization or discharge of static charge. Discharging is also known as grounding, because the charge is often discharged by means of channeling it to the ground. Discharge of static charge in the air can be so great that it creates the terrible sound we call thunder [1].

Physically, lightning is a phenomena that we may compare to a massive capacitor, with the earth serving as the second plate and the cloud acting as the first plate (which may be positive or negative). As we all know, a capacitor is a passive part of an electrical circuit that has the ability to store immediate energy. Intercloud lightning can also happen when two positively and negatively charged clouds are in close proximity to one another. Because of the potential difference between the cloud and the ground or with other clouds, lightning happens [2]. The process of the occurrence of charge on the cloud is because the particles that make up the cloud move continuously on a regular basis additionally, as they move, they will contact with other clouds, causing negative charges to accumulate on one side (either up or down) and positive charges to accumulate on the other. Negative charges (electrons) will discharge from the cloud to the ground or vice versa to attain equilibrium if the potential difference between the cloud and the earth is great enough. In this discharge process, air serves as the electrons' medium of passage. A sound explosion happens when electrons are able to cross the air insulation threshold. [2].

The rainy season is when lightning strikes most frequently because the air has a larger water content, which lowers the insulating power and facilitates easier current passage. Lightning may happen between clouds of differing charges because there are positively charged clouds and negatively charged clouds [4]. As previously stated, if the electric field between the cloud and the ground exceeds the penetrating power of the air, a charge will be released. This can be seen from the following formula:

$$E = kQ/r^2 \quad (1)$$

Where:

- Q = lightning tongue charge (Coulumbs)
- r = strike range from cloud to air
- k = constant

The potential difference of an electric charge at a point around the charge is expressed as absolute potential or simply electric potential. The electric potential of an electric charge q at a point a distance r from the charge can be expressed as follows:

$$V = kq/r \quad (2)$$

From the above equation it appears that the electric potential can be expressed in terms of the electric field strength, namely:

$$E = kq/r^2 \quad (3)$$
$$E = k\ q/r\ 1/r \quad (4)$$
$$E = v\ 1/r \quad (5)$$
$$V = E\ r \quad (6)$$

The greater the charge, the potential difference between the cloud and the ground will increase so that the greater the electric field that occurs. If the electric field generated exceeds the strength of the air-to-ground penetrating field, there will be a discharge (discharge) at that time, lightning or lightning strikes [5].

Seeing the above phenomenon, the use of lightning can be done as an alternative energy source, because lightning is renewable energy and will not run out even if it is used continuously. If the amount of water that comes from the cloud is known, then the total energy of a thunderstorm can be calculated. In a moderate thunderstorm, the energy released is up to 10,000,000 kilowatt hours (3.6×10^{13}) joules, which is equal to the power of a 20 kiloton nuclear bomb. Huge thunderstorms can be 10 to 100 times more powerful. An average-sized lightning strike has the energy to power a 100-watt light bulb for more than 3 months. An average-sized lightning strike contains an electrical power of 20,000 amps. A welder uses 250-400 amps to weld steel. Lightning travels at 150,000 km/s, or half the speed of light, and is 100,000 times faster than the speed of sound. This voltage difference in the flow of electricity between the cloud and the ground has an electric current of millions of volts. A single lightning strike has an energy of approximately 20,000 Ampere [6].

This enormous lightning electrical energy has the potential to be developed as an alternative power plant. The discovery of lightning as an electric current was first popularized by Benjamin Franklin in 1752 through his controversial kite experiment proposal. Franklin proposed hanging a Leyden vessel, a device for storing electric current, on the silk of a kite that was flown when the weather was thunderstorm. The development of technology and human life has allowed many theories and technologies for the development of the use of lightning as an alternative energy source [7]. Therefore, the author makes a research study to determine the use of lightning and the working principle of lightning utilization technology so that lightning can be utilized optimally.

METHODS

Method Approach

The research method used by researchers in this study is a qualitative approach with a descriptive method. "Research methodology is a regularly structured method or technique used by a researcher to collect data/information in conducting research that is tailored to the subject/object being studied" [8].

Sugiyono [9] defines qualitative research methods as those that examine natural objects with the researcher serving as the primary instrument, combining various data collection techniques, conducting inductive data analysis, and emphasizing meaning rather than generalization in the results.

With the help of the researcher as a crucial tool, qualitative research aims to disclose a holistic-contextual phenomena by collecting data from natural settings. When doing qualitative research, a different study strategy is used, and the results are not calculated or produced by statistical methods. We emphasize the process of qualitative

research as well as its relevance from the viewpoint of the issue since it is descriptive in character and typically uses an inductive style of analysis. [10].

Data Collection Technique

The type of research used in this study is a literature study by reviewing 10 journals related to the usefulness of lightning as power generation energy. The results of various literature reviews will be used to identify what benefits, and what should be done in an effort to use lightning as a power generator, especially in the city of Medan.

The data obtained will be analyzed by descriptive analysis method. Descriptive analysis method is done by compiling the data and facts obtained and then analyzed so as to provide the required information.

RESULTS AND DISCUSSION

Power Crisis and Benefits of Lightining Power

Massive electrostatic discharges, such as lightning, occur between electrically charged areas of clouds or between a cloud and the Earth's surface. A lightning flash, which is referred to as a strike if it impacts something on the ground, helps the charged regions of the atmosphere momentarily balance themselves. A cloud to another cloud (intra-cloud or IC), a cloud to a cloud (CC), and lastly a cloud to the ground (CG) are the three main varieties. Thunder is usually followed by lightning, however distant lighting may be visible but be too far away to be audible [11].

The world's most pressing concern is the power crisis. There have been several inventions and ideas, but those innovations have been in danger due to the lack of energy supplies. One such choice that nature provides for us is the power of lightning. Lightning is known to create enormous amounts of electricity [12].

The need for electrical energy continues to increase so that it is necessary to provide electrical energy from renewable energy sources. Medan City is a metropolitan city that demands sufficient energy supply. Electrical energy has become an important part of humans. Almost all lines of human life require electrical energy to facilitate everything, which is supported by increasingly rapid technological developments. Electrical energy so far mostly uses non-renewable energy, namely from fossils [13].

Models for New Energy Production

This work has provided two suggestions for an experimental power plant design that need further investigation, in addition to emphasizing some minor practical uses. Both of them mimic power production after natural processes. [14].

Benjamin Franklin invented the lightning rod concept in 1749 and made significant advancements toward a dependable system about 1760. A lightning rod's main function is to deflect lightning strikes and create a low-resistance path to the earth [12]. Application of voltage pulses to the lightning rod's tip with the assumption that their results will increase the conductor's attractive radius [15].

Particle Collisions for Charge Separation

Through interactions between different-sized ice particles and supercooled water, thunderstorm clouds actively produce high electrical charge separation. Collisions and induction are involved in this process. Thunderstorms efficiently transform some of the kinetic energy of the wind into electrical energy over the course of many hours to days.

As it can only catch a portion of each blow, an induction system may provide a limited amount of flexibility. The option of catching electricity resulting from a storm's regional shift in surface voltage rather than the hit itself also exists. There would be a lot of inducting stations put up for regional storm collection. Each would only be able to catch a little quantity of power, but if there were many more locations, that may be beneficial [16].

Both volcanic eruptions and thunderstorms are examples of natural events that use interactions between wind and materials to separate charges in order to function as power producers. Particle collision generators are one possible design for a charge separator that take use of the wind and particle environment..

Dusty Plasma Fusion Reactor

Ball lightning is a dusty or grain plasma. Fusion of lighter elements likely occurs inside ball lightning. More work could be done to explore artificial ball lightning formation and properties, especially what lends it stability, what forms its shell and how different chemistries of included material influence its properties.

Electricity Tapped by Lightning Arrester

Devices like horns and arresters for transmission lines that aid open and stop circuits in the event of an overvoltage are examples of infrastructure protection against lightning [14]. Sources of lightning provide more electricity than other types of energy. It will be profitable to exploit this renewable lightning energy source for human needs. In general, natural disasters like lightning are a frequent concern in my area. Because lightning produces such a high voltage, it is squandered in the earth. For our daily needs, we must utilise this energy as electricity.

Fit several lightning or catchers to the roofs of tall buildings, trees, and towers, among other places. Each lightning arrester is connected to a common transducer that is positioned at a specific location by a copper wire of suitable thickness. When lightning strikes, a large amount of electricity is captured by the lightning arrester and is sent through the circuit's conducting feeder or cable. Then, the capacitors C1, C2, and C3 are supplied with this DC voltage. These capacitors, which are utilized in HT lines, have a large capacitance range. As a result, the charged batteries or capacitors serve as a DC voltage source and supply the load with electricity for daily use [12].

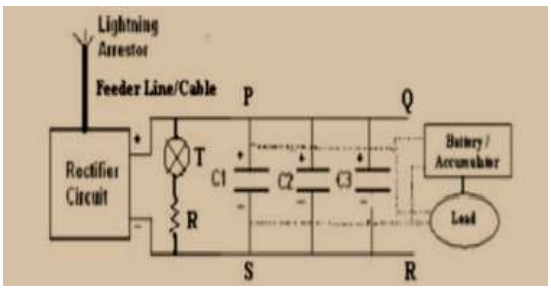

Figure 3.1. Electricity Tapped By Lighting Arrester [12]

Power of Lightning

There are around 1,200 thunderstorms active on Earth at any given time, and 100 lightning strikes are thought to occur over our globe every second. An average lightning bolt has a voltage of over 15 million volts, which rapidly warms the air around it to over 60,000 degrees, and in some cases, over 100,000 degrees. Because of this, a strong thunderstorm's overall energy can be more than the energy produced during an atomic explosion [12]. Lightning that occurs in general has several parameters, including; [17].

a. The local load displaced is 150-300 Coulomb.
b. The peak current achieved is 100–200 kA
c. Lightning charge 50–100 Coulomb.
d. Current rise steepness (in/s) 100–200 kA/ms.

Harvesting Lightning Energy

Due of the difficulties in measuring it, indirect approaches are utilized to estimate the electrical energy produced by lightning. The energy discharged by lightning has been estimated using a variety of ways in the past. The first method uses estimates of the electrostatic charge transferred, potential difference, and the charge regions that each individual lightning flash crossed, respectively [18].

Energy harvesting as a field looks at modest amounts of energy stored for low energy applications, for example, in wearable electronics. Three of the five authors found in this category are coauthors on a single paper related to alternating current (AC) energy capture in systems with mechanical or radiofrequency (RF) transducers [14].

We need a device that can sustain such high voltage in order to capture and harvest lightning energy, which is nearly impossible because the capacitor would be destroyed by the high voltage. It is necessary to convert these high voltage currents first into low voltage current. Numerous step-down transformers can be used to accomplish this. The basic function of step down transformers is to convert high voltage current to low voltage. The capacitor can then be used to store the current voltage once it has been lowered [19].

Building A Lightning Harnessing Power Plant

This concept may not be as practical as it once was. The main limiting factor in implementing a lightning arrester scheme like this is the inability to be able to store large amounts of electricity for later use. However, new Utility Scale Battery technology or other energy storage technologies such as Flywheel or Capacitors can be used to store large amounts of electricity captured from lightning, for later grid use. Obviously, lightning rod power generation will only be practical in areas that frequently experience thunderstorms, such as in Indonesia.

How difficult is it to build a lightning rod circuit to capture lightning storm electricity periodically? Making a power generation system that could resist the powerful waves produced by lightning strikes would really be the largest challenge, but even that appears doable with current technology and materials. Engineers in electrical and architectural design can find innovative ways to make it work.

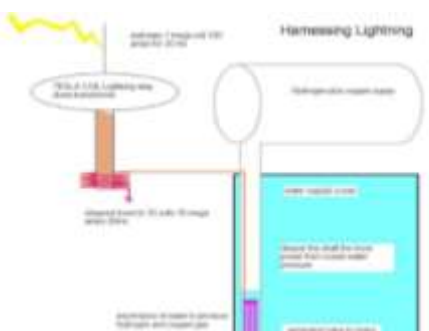

Figure 3.2. A Lightning Harnessing Power Plant [11]

Past Examples

Steve LeRoy is one person who has tried to harness the energy of thunderstorms. He was able to use the energy from a brief artificial lightning flash produced by the alternative energy company AEHI to power a 60-watt light bulb for 20 minutes, but he was unable to store the energy for later use. The energy in a thunderstorm is similar to that of an atomic bomb, according to research by Martin A. Uman, co-director of the Lightning Research Laboratory at the University of Florida, yet attempts to harness lightning energy from the ground are "hopeless" (Komolafe, Akinnubi & Olabisi, 2017).

Issues Faced

Another big challenge when trying to harvest energy from lightning is the impossibility of predicting when and where a thunderstorm will occur. Even during a storm, it's hard to tell exactly where the lightning will strike. A relatively easy method is direct harvesting of atmospheric charge before it turns into lightning. However, to collect a reasonable amount of energy requires a very large construction, and it is relatively difficult to take advantage of the very high voltages generated with reasonable efficiency.

CONCLUSION

Massive electrostatic discharges, such as lightning, occur between electrically charged areas of clouds or between a cloud and the Earth's surface. Utilizing lightning can be done as an alternative energy source, because lightning is renewable energy and will not run out even if it is used continuously. There are various alternatives in capturing electricity into a useful energy source for our lives. For example, with Building A Lightning Harnessing Power Plant, and so on that are considered capable of Harnessing Power Plants with lightning.

ACKNOWLEDGEMENT

Praise be to God who has given His grace and blessing, so that this team can finish writing on time. Thank you to Medan State University as a place for students to study and explore. Thank you to Ma'am. Khairiza Lubis, S.Si., M.Sc., Ph.D., as the supporting lecturer. Thank you to the NSESP 2019. Thank you to the people of Medan in particular who have taken the time and place to carry out research. We thank you, without your help this research could not be completed.

REFERENCES

[1] Septiadi, D., Hadi, S., & Tyasono, B. 2011. Karakteristik Petir dari Awan ke Bumi dan Hubungannya dengan Curah Hujan. *Jurnal Sains Dirgantara*. 8 (2):129-138.
[2] Horvath, T. 2006. *Understanding Lightning and Lightning Protection*. John Wiley & Sons, Ltd: England.
[3] Baba, Y., & Rakov, V. A. 2016. *Electromagnetic Computation Methods For Lightning Surge Protection Studies*. John & Wiley, Ltd: Singapore.
[4] Cooray, V. 2015. *An Introduction to Lightning*. Springer: Sweden
[5] Elsom, D. M. 2015. *Lightning: Nature and Culture*. Reaktion Book Ltd: London.
[6] Rakov, V. A., & Uman, M. A. 2013. *Lightning: Physics and Effects*. Cambridge University Press.
[7] Komofale, D. A., Akinnubi R, T., & Olabisi, I. O. 2017. Thunderstorm Energy: An Alternative Energy Resource In The Humid Tropical Region Of West Africa. *Science and Technology*. 3 (9):54-58.
[8] Rizka, A. U. 2018. *Makna Metodologi Penelitian*. Social Sciences. 1-3.
[9] Prasanti, D. 2018. Penggunaan Media Komunikasi Bagi Remaja Perempuan Dalam Pencarian Informasi Kesehatan. *Jurnal Lontar*. 6 (1):13-21.
[10] Fadli, M. R. 2021. Memahami Desain Metode Penelitian Kualitatif. *Humanika: Kajian Ilmiah Mata Kuliah Umum*. 21 (1):33-54.
[11] Malavika, S., & Vishal, S. 2013. Harnessing Electrical Energy From Lightning. *International Journal of Application or Innovation in Engineering & Management (IJAIEM*). 2 (9):23-27.
[12] Dongre, M. S, Desmukh, M. B & Nagdewate, P. A 2017. Renewable Energy Source From Lightning Strokes. *International Research Journal of Engineering and Technology (IRJET)*. 04 (01):1420-1422.
[13] Agfanny, F., Djayus., & Supriyanto. 2020. Tren Sambaran Petir Cloud To Ground Kota Balikpapan Tahun 2016-2018. *Jurnal Geosains Kutai Basin*. 3 (2):1-6.
[14] Helman, D. 2020. Lightning for Energy and Material Uses: A Structured Review. *Global Challenge*. 4:1-17.
[15] Cooray, V. 2018. The Similarity of the Action of Franklin and ESE Lightning Rods under Natural Conditions. *Atmosphere*. 9 (225):1-6
[16] Helman, D. 2011. Summary Article: Catching Lightning for Alternative Energy. *Renewable Energy*. 1-11.
[17] Lubis, Z., Aryza, S., & Annisa, S. 2019. Metode Terbaru Perancangan Proteksi Petir Eksternal Pada Pembangkit Listrik. *Journal of Electrical Technology*. 4 (1): 26-34.
[18] Salinas, V., Bruning, E., Mansell, E., & Brothers, M. 2021. Modeling the Electrical Energy Discharged by Lightning Flashes Using Capacitors for Application with Lightning Datasets. *Journal Of The Atmospheric Science*. 78:3909-3924.
[19] Anupam, A. 2020. Trapping & Harvesting Lightning Energy. *International Journal of Engineering Research & Science (IJOER)*. 6 (4):45-48.

Available online at:
Al-Fiziya: Journal of Materials Science, Geophysics, Instrumentation and Theoretical Physics
Website: http://journal.uinjkt.ac.id/index.php/al-fiziya
Vol.5 No. II Tahun 2022, 95 - 100

The radial wave function of 2D and 3D quantum harmonic oscillator

Adam Badra Cahaya [1]

Universitas Indonesia, Jakarta, Indonesia

Submitted: Agustus 2022; Revised: September 2022; Approved: Oktober 2022; Available Online: Desember 2022

Abstract. One dimensional quantum harmonic oscillator is well studied in elementary textbooks of quantum mechanics. The wave function of one-dimensional oscillator harmonic can be written in term of Hermite polynomial. Due to the symmetry of the spring energy, the wave functions of two-dimensional and three-dimensional harmonic oscillators can be written as products of the one-dimensional case. Because of that, the wave functions of two- and three-dimensional cases are focused on cartesian coordinates. In this article, we utilize polar and spherical coordinates to describe the wave function of two- and three-dimensional harmonic oscillators, respectively. The radial part of the wave functions can be written in term of associated Laguerre polynomials.

Keywords: *associated Laguerre polynomials, quantum harmonic oscillator, radial wave function, two dimension quantum harmonic oscillator, three dimension quantum harmonic oscillator.*

DOI : *10.15408/fiziya.v5i2.26172*

INTRODUCTION

In elementary textbooks of quantum mechanics, one dimensional quantum harmonic oscillator is well studied using a potential energy analogous to classical harmonic oscillator

$$V(x) = \frac{1}{2}M\omega^2 x^2. \tag{1}$$

Here M is mass of the particle, ω is the characteristic radial frequency. The eigen wave function of the Schrödinger equation $(p^2/(2m) + V(x))\psi = i\hbar\dot{\psi}$ can be written in term of Hermite polynomials H_n [1]

$$\psi_{1\mathrm{d}} = e^{-\frac{i}{\hbar}E_n t}\sqrt{\frac{\alpha}{2^n n!\sqrt{\pi}}}e^{-\frac{1}{2}\alpha^2 x^2}H_n(\alpha x). \tag{2}$$

Here $\alpha = \sqrt{M\omega/\hbar}$, and $E_n = \left(n + \frac{1}{2}\right)\hbar\omega$ is the quantized energy.

However, the potential is a central potential $V(\vec{r}) = \frac{1}{2}m\omega^2 r^2$ and therefore the eigen wave functions should be able to be written as a product of radial and angular wave functions [2]. The angular wave functions of two- and three-dimensional potentials wit central symmetry are well-described using sinusoidal and spherical harmonics

Copyright©2019, Published by **Al-Fiziya: Journal of Materials Science, Geophysics, Instrumentation and Theoretical Physics**
P-ISSN: 2621-0215, E-ISSN: 2621-489X

functions, respectively [3]. However, studies of higher dimension quantum oscillators elude the discussion of radial wave function [4]–[8].

It may be due to the additive property of the norm of $\vec{r}$. Because of that, the generalization of the potential energy into two and three dimensions is straightforward

$$V(\vec{r}) = \begin{cases} \frac{1}{2}M\omega^2(x^2+y^2), & \text{for 2d,} \\ \frac{1}{2}M\omega^2(x^2+y^2+z^2), & \text{for 3d.} \end{cases} \tag{3}$$

Because of this symmetry, the wave functions of two- and three-dimensional cases are focused on cartesian coordinates

$$\begin{cases} \psi_{2\mathrm{d}} = e^{-i(n_x+n_y+1)\omega t}\left(\frac{\alpha}{2^n n!\sqrt{\pi}}\right) e^{-\frac{1}{2}\alpha^2(x^2+y^2)} H_{n_x}(\alpha x) H_{n_v}(\alpha y), \\ \psi_{3\mathrm{d}} = e^{-i\left(n_x+n_y+n_z+\frac{3}{2}\right)\omega t}\left(\frac{\alpha}{2^n n!\sqrt{\pi}}\right)^{\frac{3}{2}} e^{-\frac{1}{2}\alpha^2(x^2+y^2+z^2)} H_{n_x}(\alpha x) H_{n_v}(\alpha y) H_{n_z}(\alpha z). \end{cases} \tag{4}$$

Coefficient of time-dependent exponential indicates that the energy eigenvalues also have the additive properties.

$$E_n = \begin{cases} \hbar\omega\left(n_x+n_y+1\right), & \text{for 2d,} \\ \hbar\omega\left(n_x+n_y+n_z+\frac{3}{2}\right), & \text{for 3d.} \end{cases} \tag{5}$$

In this article, we utilize polar and spherical coordinates to describe the wave function of two- and three-dimensional harmonic oscillators, respectively. The understanding of radial wave function should provide better insight on the mathematical physics of basic quantum mechanics.

VARIABLES SEPARATIONS OF SCHRÖDINGER EQUATION

Schrodinger equation of quantum particle under the influence of central potential energy

$$\left(-\frac{\hbar^2}{2M}\nabla^2 + \frac{1}{2}m\omega^2 r^2\right)\psi(\vec{r},t) = i\hbar\frac{\partial}{\partial t}\psi(\vec{r},t), \tag{6}$$

can be rewritten using variable separation with energy's eigen values E

$$\frac{1}{u(\vec{r})}\left(-\frac{\hbar^2}{2M}\nabla^2 + \frac{1}{2}m\omega^2 r^2\right)u(\vec{r}) = E = \frac{i\hbar}{T(t)}\frac{\partial T(t)}{\partial t}, \tag{7}$$

to arrive at the time-independent wave function $u(\vec{r})$ and space-independent $T(t)$. One can show that straight-forwardly shows that

$$T(t) = e^{-\frac{1}{\hbar}Et}. \tag{8}$$

The Laplacian ∇^2 in polar (r,θ) and spherical (r,θ,ϕ) coordinates is

$$\nabla^2 = \begin{cases} \frac{\partial^2}{\partial r^2} + \frac{1}{r}\frac{\partial}{\partial r} + \frac{1}{r^2}\frac{\partial^2}{\partial\theta^2}, & \text{for 2d,} \\ \frac{\partial^2}{\partial r^2} + \frac{2}{r}\frac{\partial}{\partial r} + \frac{1}{r^2}\left(\frac{1}{\sin\theta}\frac{\partial}{\partial\theta}\left(\sin\theta\frac{\partial}{\partial\theta}\right) + \frac{1}{\sin^2\theta}\frac{\partial^2}{\partial\phi^2}\right), & \text{for 3d.} \end{cases} \tag{9}$$

In the following subsections the time-independent wave function is further separated into radial and angular wave functions. In particular, the radial wave equation can be written as associated Laguerre differential equation [9]

$$\left(x\frac{d^2}{dx^2}+(\nu+1-x)\frac{d}{dx}+\lambda\right)L_\lambda^\nu(x), \tag{10}$$

where $L_\lambda^\nu(x)$ is the associated Laguerre polynomial [10]. For non-integer ν, L_λ^ν is also called generalized Laguerre function [11].

Two-dimensional quantum harmonic oscillator in polar coordinate

Substituting $u(\vec{r})=R(r)\Theta(\theta)$

$$\frac{1}{R(r)}\left(\frac{d^2}{dr^2}+\frac{1}{r}\frac{d}{dr}+\frac{1}{r^2}\left[\frac{1}{\Theta(\theta)}\frac{d^2\Theta(\theta)}{d\theta^2}\right]\right)R(r)=E \tag{11}$$

we can arrive at the equation for radial $R(r)$ and angular wave function $\Theta(\theta)$

$$\frac{1}{R(r)}\left(\frac{d^2}{dr^2}+\frac{1}{r}\frac{d}{dr}-\frac{l^2}{r^2}\right)R(r)=E, \tag{12a}$$

$$\frac{1}{\Theta(\theta)}\frac{d^2\Theta(\theta)}{d\theta^2}=-l^2. \tag{12b}$$

The solution of Eq. (12b)

$$\Theta(\theta)=\frac{1}{\sqrt{2\pi}}e^{il\theta}. \tag{13}$$

Setting $R(r)=r^l e^{-\frac{1}{2}\alpha^2r^2}f(\alpha^2r^2)$, substitution Eq. (12a) can be written in similar form to Eq. (10)

$$\left(u\frac{d^2}{du^2}+(l+1-u)\frac{d}{du}+\frac{E}{2\hbar\omega}-\frac{(l+1)}{2}\right)f(u), \tag{14}$$

Therefore

$$R(r)\propto r^l e^{-\frac{1}{2}\alpha^2r^2}L_n^l(\alpha^2r^2), \tag{15}$$

and the quantization of eigen energy is similar to Eq. (5)

$$E_\nu=\hbar\omega(2n+l+1). \tag{16}$$

Three-dimensional quantum harmonic oscillator in spherical coordinate

Substituting $u(\vec{r})=R(r)\Theta(\theta)\Phi(\phi)$

$$\frac{1}{R(r)}\left(\frac{d^2}{dr^2}+\frac{2}{r}\frac{d}{dr}+\frac{1}{r^2}\left[\frac{1}{r^2\sin\theta}\frac{\partial}{\partial\theta}\left(\sin\theta\frac{\partial}{\partial\theta}\right)+\frac{1}{r^2\sin^2\theta}\frac{\partial^2}{\partial\phi^2}\right]\right)R(r)=E \tag{17}$$

we can arrive at the equation for radial $R(r)$ and angular wave function $\Theta(\theta)$

$$\frac{1}{R(r)}\left(\frac{d^2}{dr^2}+\frac{2}{r}\frac{d}{dr}-\frac{\hbar l(l+1)}{r^2}\right)R(r)=E, \tag{18a}$$

$$\frac{1}{\Theta(\theta)}\left(\frac{1}{\sin\theta}\frac{\partial}{\partial\theta}\left(\sin\theta\frac{\partial}{\partial\theta}\right)-\frac{m^2}{\sin^2\theta}\right)\Theta(\theta)=-l(l+1), \tag{18b}$$

$$\frac{1}{\Phi(\phi)}\frac{d^2\Phi(\phi)}{d\phi^2}=-m^2. \tag{18c}$$

The solution of Eq. (17b) and (17c) is the spherical harmonics function [12], [13]

$$\Theta(\theta)\Phi(\phi)=Y_{lm}(\theta,\phi). \tag{19}$$

Setting $R(r) = r^l e^{-\frac{1}{2}\alpha^2 r^2} g(\alpha^2 r^2)$, substitution Eq. (12a) can be written in similar form to Eq. (10)

$$\left(u\frac{d^2}{du^2} + \left(l + \frac{3}{2} - u\right)\frac{d}{du} + \frac{E}{2\hbar\omega} - \frac{(l+3/2)}{2}\right) g(u), \tag{20}$$

Therefore

$$R(r) \propto r^l e^{-\frac{1}{2}\alpha^2 r^2} L_n^{l+\frac{1}{2}}(\alpha^2 r^2), \tag{21}$$

and the quantization of eigen energy is similar to Eq. (5)

$$E_v = \hbar\omega\left(2n + l + \frac{3}{2}\right). \tag{22}$$

RADIAL AND ANGULAR WAVE FUNCTIONS

Eq. (51) and (21) show that the radial wave functions can be written in term of associated Laguerre polynomials. The normalization factors that satisfy

$$1 = \begin{cases} \int_0^\infty [R(r)]^2\, r dr, & \text{for 2d,} \\ \int_0^\infty [R(r)]^2\, r^2 dr, & \text{for 3d,} \end{cases} \tag{23}$$

can be found using the orthogonality of associated Laguerre polynomials

$$\int_0^\infty x^k e^{-x} L_v^k(x) L_w^k(x)\, dx = \frac{\Gamma(v+k+1)}{v!}\delta_{vw} \tag{24}$$

Such that

$$R(\vec{r}) = \begin{cases} \sqrt{\frac{n!\, 2(a)^{2l+2}}{(n+l)!}}\, r^l e^{-\frac{1}{2}\alpha^2 r^2} L_n^l(\alpha^2 r^2), & \text{for 2d,} \\ \sqrt{\frac{n!\, 2(a)^{2l+3}}{\Gamma\left(n+l+\frac{3}{2}\right)}}\, r^l e^{-\frac{1}{2}\alpha^2 r^2} L_n^{l+\frac{1}{2}}(\alpha^2 r^2) & \text{for 3d.} \end{cases} \tag{23}$$

Here $\Gamma(x)$ is the Gamma function.

Concerning the angular wave function Eqs. (12b) and (18b-c) can be associated with the eigen equations of the angular momentum in two and three dimensions, respectively [14]. Eq. (12b) is equivalent with the eigen equation

$$\vec{L}_{2\mathrm{d}}\Theta(\theta) = \hbar l \Theta(\theta) \tag{24}$$

of the two-dimensional angular momentum

$$\vec{L}_{2\mathrm{d}} = -i\hbar\frac{\partial}{\partial\theta}. \tag{25}$$

Meanwhile, Eq. (18b) is equivalent with the eigen equations

$$\begin{aligned} L_{3\mathrm{d}}^2 \mathrm{Y}_{lm}(\theta,\phi) &= \hbar^2 l(l+1)\mathrm{Y}_{lm}(\theta,\phi) \\ \hat{z}\cdot\vec{L}_{3d}\mathrm{Y}_{lm}(\theta,\phi) &= \hbar m \mathrm{Y}_{lm}(\theta,\phi) \end{aligned} \tag{26}$$

of the three-dimensional angular momentum

$$\begin{aligned} \vec{L}_{3\mathrm{d}} = -i\hbar\Big[\hat{x}\left(-\sin\phi\frac{\partial}{\partial\theta} - \cot\theta\cos\phi\frac{\partial}{\partial\phi}\right) + \hat{y}\left(\cos\phi\frac{\partial}{\partial\theta} - \cot\theta\sin\phi\frac{\partial}{\partial\phi}\right) \\ + \hat{z}\frac{\partial}{\partial\phi}\Big]. \end{aligned} \tag{27}$$

Finally, the full time-space dependent eigen wave function is

$$\psi = \begin{cases} \sqrt{\dfrac{n!\,(a)^{2l+2}}{\pi(n+l)!}}\, r^l e^{-\frac{1}{2}\alpha^2 r^2} L_n^l(\alpha^2 r^2) e^{il\theta} e^{-i(2n+l+1)\omega t}, & \text{for 2d,} \\ \sqrt{\dfrac{n!\,2(a)^{2l+3}}{\Gamma\left(n+l+\frac{3}{2}\right)}}\, r^l e^{-\frac{1}{2}\alpha^2 r^2} L_\nu^{l+\frac{1}{2}}(\alpha^2 r^2) Y_{lm}(\theta,\phi) e^{-i\left(2n+l+\frac{3}{2}\right)\omega t}, & \text{for 3d.} \end{cases} \quad (28)$$

CONCLUSION

Two- and three-dimensional quantum oscillator harmonics is discussed in terms of radial and angular eigen wave functions. The angular wave functions are well-described using sinusoidal and spherical harmonics functions, respectively. Using appropriate ansatz, it is shown that the radial wave function is proportional to $r^l e^{-\frac{1}{2}\alpha^2 r^2} L_n^k(\alpha^2 r^2)$, where l is related to the eigenvalues of angular momentum operators and L_n^k is generalized/associated Laguerre polynomials.

REFERENCES

[1] S. Gasiorowicz, *Quantum Physics*, 3rd ed. Nashville, TN: John Wiley & Sons, 2003.
[2] M. Albert, "Quantum Mechanics Vol. 1." Amsterdam: North-Holland, 1961.
[3] L. M. B. C. Campos and M. J. S. Silva, "On hyperspherical associated Legendre functions: the extension of spherical harmonics to N dimensions." arXiv, 2020. doi: 10.48550/ARXIV.2005.09603.
[4] S. F. Viñas and F. Vega, "Magnetic properties of a Fermi gas in a noncommutative phase space." arXiv, 2016. doi: 10.48550/ARXIV.1606.03487.
[5] S. Biswas, P. Nandi, and B. Chakraborty, "Emergence of a geometric phase shift in planar noncommutative quantum mechanics," *Physical Review A*, vol. 102, no. 2, p. 22231, Aug. 2020, doi: 10.1103/PhysRevA.102.022231.
[6] V. P. Nair and A. P. Polychronakos, "Quantum mechanics on the noncommutative plane and sphere," *Physics Letters B*, vol. 505, no. 1, pp. 267–274, 2001, doi: https://doi.org/10.1016/S0370-2693(01)00339-2.
[7] A. Smailagic and E. Spallucci, "Isotropic representation of the noncommutative 2D harmonic oscillator," *Physical Review D*, vol. 65, no. 10, p. 107701, Apr. 2002, doi: 10.1103/PhysRevD.65.107701.
[8] A. Hatzinikitas and I. Smyrnakis, "The noncommutative harmonic oscillator in more than one dimension," *Journal of Mathematical Physics*, vol. 43, no. 1, pp. 113–125, Dec. 2001, doi: 10.1063/1.1416196.
[9] E. W. Weisstein, "Laguerre Differential Equation," *MathWorld--A Wolfram Web Resource. https://mathworld.wolfram.com/LaguerreDifferentialEquation.html*.
[10] G. B. Arfken, H. J. Weber, and F. E. Harris, "Chapter 18 - More Special Functions," in *Mathematical Methods for Physicists (Seventh Edition)*, G. B. Arfken, H. J. Weber, and F. E. Harris, Eds. Boston: Academic Press, 2013, pp. 871–933. doi: https://doi.org/10.1016/B978-0-12-384654-9.00018-9.
[11] E. W. Weisstein, "Associated Laguerre Polynomial," *MathWorld--A Wolfram Web Resource. https://mathworld.wolfram.com/AssociatedLaguerrePolynomial.html*.

[12] G. B. Arfken, H. J. Weber, and F. E. Harris, "Chapter 15 - Legendre Functions," in *Mathematical Methods for Physicists (Seventh Edition)*, G. B. Arfken, H. J. Weber, and F. E. Harris, Eds. Boston: Academic Press, 2013, pp. 715–772. doi: https://doi.org/10.1016/B978-0-12-384654-9.00015-3.

[13] M. L. Boas, *Mathematical methods in the physical sciences*, 3rd ed. Nashville, TN: John Wiley & Sons, 2005.

[14] J. Zhang, "Fractional angular momentum in non-commutative spaces," *Physics Letters B*, vol. 584, no. 1, pp. 204–209, 2004, doi: https://doi.org/10.1016/j.physletb.2004.01.049.

Available online at:
Al-Fiziya: Journal of Materials Science, Geophysics, Instrumentation and Theoretical Physics
Website: http://journal.uinjkt.ac.id/index.php/al-fiziya
Vol.5 No. II Tahun 2022, 101 - 110

CHARACTERISTICS OF ANTI-TERMITE PARTICLE BOARD FROM BINTARO FRUIT FIBER WITH BINTARO FRUIT SEED EXTRACT COATING USING SPRAY COATING METHOD

Delovita Ginting, M.Si[1+], Karnila Sukma[1]

[1] Physics Study Program, Faculty of Mathematics, Natural Sciences and Health, University of Muhammadiyah Riau, Tuanku Tambusai street, Pekanbaru City, Pekanbaru 28291, Indonesia

†delovita@umri.ac.id

Submitted: Agustus 2022; Revised: September 2022; Approved: Oktober 2022; Available Online: Desember 2022

Abstract. Termites are pests that damage wooden furniture. Termite attacks on wooden furniture are getting higher and broader, so the value of losses due to termite attacks on furniture is increasing from year to year. This research has succeeded in making particle boards from bintaro fruit fibers as fillers and urea formaldehyde resin (UF) as a matrix with a composition of filler mass fractions: the matrix of the particle board to be made is 30:70. The particle board that has been made is then coated using bintaro seed extract and UF resin using the spray coating method. The extract mass fractions of bintaro seeds and UF resins in this study were sample 1 (90:10), sample 2 (80:20), sample 3 (70:30), sample 4 (60:40) and sample 5 (50:50). The physical characterization of particleboard includes density, water absorption, and moisture content. The mechanical characterization of particle boards is the bending strength and characterization of particle boards to resistance to termite attacks. The results of this study show that particle boards with optimum values are sample particle boards 1 with a density value of 0.864 gr / cm^3, water absorption of 4.28%, which has met SNI 03-2105-2006 and the results of testing the resistance to termites 3.45% have met SNI 01-7207-2006. Because the structure influences the manufacture of particle boards and the physical shape of the raw materials used.

Keywords: *Bintaro Fruit, Natural Fiber, Extract, UF Resin, Biocomposite*
DOI : *10.15408/fiziya.v5i2.31241*

INTRODUCTION

Termites are pests that damage wooden furniture. Termite attacks on wooden parapets are getting higher and broader, so the value of losses due to termite attacks on furniture increases yearly [1]. Economic losses due to termite attacks on residential furniture in Indonesia have reached 1.67 trillion rupiah. Damage to residential furniture is caused by the disruption of the natural habitat of termites on agricultural land, plantations, and forests that turn into residential areas [2].

Furniture is usually made of several materials, one of which is particle board. Particle board is in great demand by consumers because it is made of environmentally friendly natural fibers. Particle board consists of fiber as a filler and matrix as a binder. The filler material for manufacturing particle boards is a natural fiber with lignin and

Copyright©2019, Published by **Al-Fiziya: Journal of Materials Science, Geophysics, Instrumentation and Theoretical Physics**
P-ISSN: 2621-0215, E-ISSN: 2621-489X

cellulose [3]. Many studies on natural fibers have been carried out including areca nut fiber, empty palm oil bunches, coconut fiber, and water hyacinth [2];[4];[5];[6].

Many studies on furniture damage have been carried out, including [7] regarding adding a matrix of citric acid to particle boards. The resistance to termite attack by dry wood was 57-78%. [8] produced research that ironwood extract as a matrix on particle boards increased the number of dead termites by 4−6%. The next method is particle board coating, which uses spray coating. The spray coating method can protect the particle board surface against scratches, stains, and weather resistance and give a glossy and satin effect [9]. Research [10] also used the spray coating method to see the differences between single and two layers. The two-layer coating is better than a single layer.

Research [11] says that bintaro fruit contains cellulose (56.76%) and lignin (28.30%), so bintaro fruit fiber can be used as fiber for particle board. Bintaro plants in Riau Province are usually used as ornamental plants on the side of the road and as shade plants. Bintaro has strong roots to prevent erosion when it rains, while the fruit can be used as a rat repellent. Research [12] states that bintaro fruit seeds contain saponins and pephenol compounds which are toxic and can be used as termite exterminators.

Bintaro's enormous potential from both fiber and seeds can be utilized for the furniture industry, one of which is as particle board. In this study bintaro fiber as fiber and urea formaldehyde as matrix. This study used a coating on particle board by utilizing Bintaro fruit seed extract using the spray coating method . The particle board to be made will be tested for physical, mechanical and termite resistance based on SNI 03-2105-2006 standards.

RESEARCH METHOD

Research Tools and Materials

The tools used in this study are mixers , calipers , digital balances, material containers, Sieve 100 mesh , Beaker glass , Steel mold size (21 x 21 x 2) cm , Cold press , Oven , Greending Machine , Grinding Machine and Aluminum Foil . The materials used in this research were bintaro fruit fiber , bintaro fruit seeds , urea formadehid resin , water and ethanol .

Preparation of Bintaro Fruit Fiber

Bintaro fruit that has been collected is dried in the sun to dry . Bintaro fruit that has been dried in half . then separated between the fiber and the shell of the Bintaro seeds . Bintaro fruit fiber that has been separated from the shell is ground using a greending machine until smooth. Bintaro fruit fiber that has been refined is filtered using a 50 mesh sieve [13].

Particle board manufacturing process

The materials used for the manufacture of particle board are bintaro fruit fiber as a filler (fiber) and urea formaldehyde (UF) resin as an adhesive (matrix) in the manufacture of particle board with a ratio (35% water : 35% UF resin : 30% bintaro fruit fiber) . Prepare UF resin and water in a container then stir until combined. The crushed Bintaro fruit fiber and UF resin are mixed with stirring using a mixer for 10 minutes so that they are evenly mixed. The mixed Bintaro fruit fiber and resin are put into a particle board mold

measuring (21 x 21 x 3) cm and covered with aluminum foil . The fiber and UF resin that has been put into the mold are leveled so that there are no parts of the mold that are not filled and then compressed using a cold press with a pressure of 5 bar for 2 hours [13] , so that 2 cm is obtained for the thickness of the particle board. Lift the felt cover and gently pick up the printed particle board . Particle board that has been taken from the mold is left for up to 5 days to dry completely [14].

Preparation of Bintaro Fruit Seeds

Bintaro seeds that have been separated from their shells are sun-dried for 1 week and baked for 1 hour at 40°C [15]. The dried Bintaro seeds were crushed using a grinding machine with a fineness of 50 mesh [13] .

The Process of Making Bintaro Fruit Seed Extract

Bintaro seeds that have been refined soaked in 96% ethanol solution with ratio (1:3), so to produce 3 liters of extract, 1 kg of bintaro seeds and 3 liters of ethanol are needed, soaked for 3 x 24 hours, then filtered using a buchiner funnel covered with coarse filter paper . Bintaro seed extract is stored in the refrigerator (≤40 C) before use [15].

Particle Board Coating Process Using Bintaro Seed Extract

Bintaro seed extract and UF resin were mixed in the ratio as shown in Table 1. The particle board was made in 5 variations , each variation containing 3 samples. The mixture of UF extract and resin was sprayed onto the particle board using a double layer spray gun , at a distance of 30 cm from the surface of the particle board. The drying process was carried out at 21°C for 48 hours based on research [10].

Table 1. Comparison of Bintaro Seed Extract and Urea Formaldehyde Resin

Variation	Made Samples	Bintaro Fruit Seed Extract (%)	Urea Formaldehyde Resin (%)
Variation 1	3 pieces	90	10
Variation 2	3 pieces	80	20
Variation 3	3 pieces	70	30
Variation 4	3 pieces	60	40
Variation 5	3 pieces	50	50

Testing Process

Density Test

The density or compactness of a particle in a sheet depends on the density of the fiber and the amount of pressure exerted during the particleboard manufacturing process. Density is calculated based on the weight and dry volume of the air sample. Test sample measuring 10 cm x 10 cm according to SNI 03-2105-2006 The amount of density can be calculated by Equation (1) [16] .

$$\rho = \frac{B}{V} \quad (1)$$

Note: ρ= Density (gr/cm^3) ; B= Weight of test sample (g) ; V= Volume of test sample (cm3)

Water Absorption Test

The water absorption test is intended to determine the ability of the composite to absorb water to the maximum extent. Testing the board's water absorption is calculated by measuring the difference in weight before and after soaking for 24 hours. The test sample measuring 5 cm x 5 cm x 2 cm according to SNI 03-2105-2006 . The value of water absorption is calculated by Equation (2) [16] .

$$\text{DSA}\ (\%) = \frac{\text{B1} - \text{B0}}{\text{B0}} \text{x}\ 100\% \qquad (2)$$

Information: DSA = Water absorption (%) ; B0 = Weight of sample before immersion (g) ; B1 = weight of sample after immersion (g) .

Water Content Test

The water content test is intended to determine the weight of water contained in the particle board expressed in percent (%) of the dry weight of the particle board. Testing the board's moisture content is calculated by measuring the difference in weight before and after being in the oven. Test sample measuring 10 cm x 10 cm x 2 cm according to SNI 03-2105-2006 The value of water absorption is calculated by Equation (3) [16].

$$\text{kadar air}\ (\%) = \frac{\text{Ba} - \text{Bk}}{\text{Bk}} \text{x}\ 100\% \qquad (3)$$

Information: Ba= weight of sample before oven (g) ; Bk = Weight of the test sample after being in the oven (g)

Strength Test

Flexural strength is the ability of a material to withstand a bending force applied in a direction perpendicular to the sample cross section. Usually the flexural strength of the test sample measuring 20 cm x 1.27 cm x 1.27 cm with reference to the SNI 03-2105-2006 standard, the flexural strength value can be calculated using Equation (4) [16] .

$$\sigma\text{b} = \frac{3\text{PL}}{2\text{bd}^2} \qquad (4)$$

Information : σ: bending strength (Kgf/cm ^{2}); d: applied load (Kgf) ; b : sample thickness (cm) ; P : support distance (cm) ; L: specification width (cm)

Termite Resistance Test

To determine the success of research on anti-termite particleboard, calculations are needed about the effect of particleboard on termites, so calculations are needed when the test sample loses its weight at the end of exposure after observation. Testing for termite attack uses the SNI 01-2707-2006 standard using Equation (5) [17].

$$\text{P} = \frac{\text{w1} - \text{w2}}{\text{w2}} \text{x}\ 100 \qquad (5)$$

Information : Q : Weight loss; W1 : wood weight before testing (grams); W2 : weight of wood after testing (grams).

RESULTS AND DISCUSSION

Density

Density testing was carried out to see the effect of the density value produced by the particle board. This sample was calculated using the SNI 03-2105-2006 testing

standard. The results of the density test can be seen in Figure 1 which shows the relationship between the density value and the coating composition of the Bintaro fruit seed extract used. The sample that has the highest density value is sample 1 (extract 90: UF 10 resin) with a density value of 0.864 gr/cm^3. The lowest density value was found in sample 5 (extract 50: UF 50 resin) of 0.541 gr/cm^3. The addition of Bintaro fruit seed extract coating on the composition of particle board affects the density value. The results of the particle board density test decreased in each sample, this is because the less extract used, the density value also decreased. Research [18] states that the density depends on the constituent materials which can cause absorption or entry of more extracts into the pores of the particle board, the higher the resulting density value. Research on the density value of particle board has been carried out [19] stating that the density of particle board is affected by the structure of the physical form of the particle raw material used. The results of the regression equation analysis show that the addition of fiber composition results in a lower density value.

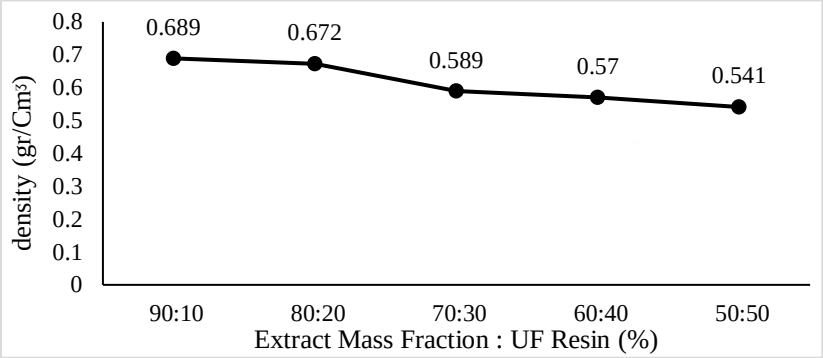

Figure 1. Results of Termite Particle Board Density Test

Water Absorbency

The water absorption test aims to determine the ability of particle board to absorb water during immersion in water for 24 hours. The water absorption test refers to research [20]. The test graph can be seen in Figure 2 which shows the relationship between the value of water absorption and the coating composition of the Bintaro fruit seed extract used. The sample that has the highest water absorption value is sample 5 (extract 50: UF 50 resin) with an absorption value of 53.64% . The lowest density value was found in sample 1 (extract 90: UF 10 resin) of 34.49%. The addition of Bintaro fruit seed extract coating to the composition for making particle board affects the value of water absorption. The results of the water absorption test are higher for each sample, this is because the more UF resin used, the more water absorption capacity will be produced. UF resin has binding properties that cause water to enter the composite [21]. Research [22] states that the high value of water absorption is due to the hygroscopic nature of particle board because it contains lignin and cellulose, and all materials containing lignin and cellulose are very easy to absorb and release water.

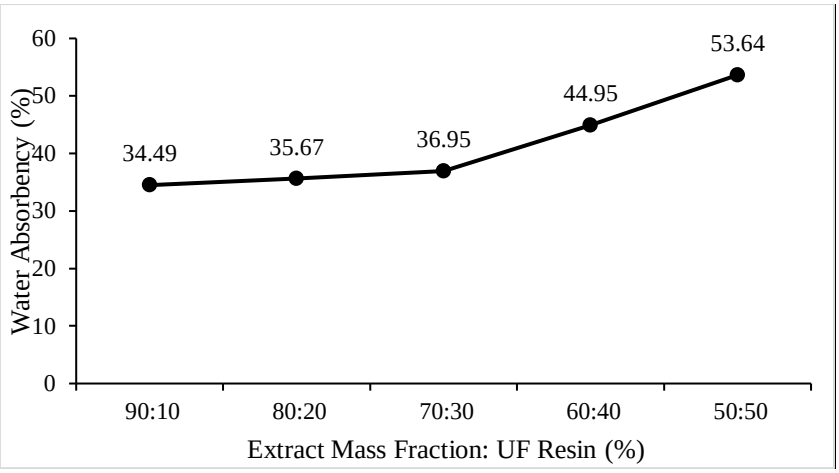

Figure 2. Test Results of Termite Particle Board Water Absorbency

Water Content Test

Testing the water content aims to determine the water content contained in the particle board. This test refers to the SNI 03-2105-2006 standard. The results of testing the water content test values can be seen in Figure 3 which shows the effect of the composition of the Bintaro fruit seed extract and UF resin on the water content values on particle board. The highest water content value was in sample 5 (50 extract: UF 50 resin) with a water content value of 6.75%. The lowest water content value was in sample 1 (extract 90: UF 10 resin) with a water content value of 4.28%. The addition of Bintaro fruit seed extract coating to the composition for making particle board affects the value of the water content. The sample has a higher water absorption value for each sample, this is because the more extracts used, the lower the water content value. The extract used contains water and alcohol which, if heated at 100°C, will evaporate, thus affecting the water content in the test object [23]. [24] stated that during conditioning, particle board composed of sawdust wood particles still has hygroscopic properties, meaning it can absorb or release water from its environment.

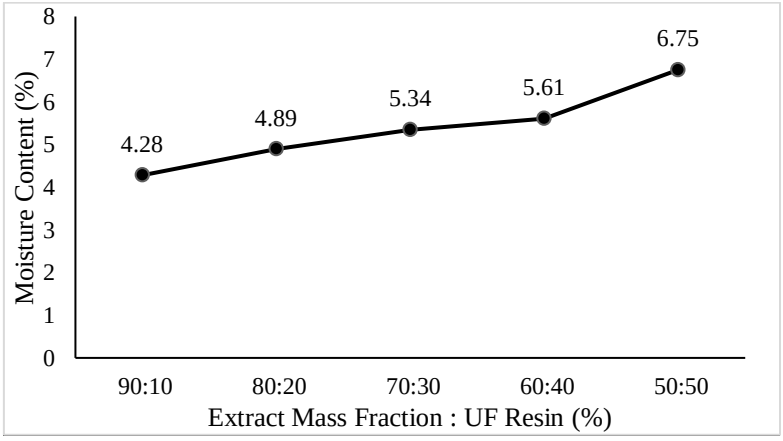

Figure 3. Moisture Test Results for Anti-Termite Particle Boards

Flexural Strength Test

The flexural strength test was carried out to determine the elasticity of the sample by applying a bending load slowly until the sample breaks. Flexural strength testing is carried out with reference to the SNI 03-2105-2006 standard. The test results can be seen

Vol.5 No. II Tahun 2022, 101 - 110
P-ISSN: 2621-0215, E-ISSN: 2621-489X

in Figure 4 which shows the relationship between the value of the flexural strength of particle board and the extract of bintaro fruit seeds as a coating. The particle board sample that had the highest flexural strength value was sample 5 (extract 50: UF 50 resin) with a flexural strength value of 25.18Mpa. The lowest flexural strength value is sample 1 (extract 90: UF 10 resin) with a flexural strength value of 15.09 Mpa. The addition of Bintaro fruit seed extract coating to the composition for making particle board affects the value of flexural strength. The value of flexural strength is higher in each sample because the more resin is used, the more flexural strength will be produced, UF resin has binding and hardness properties, this makes the test object increase in the value of flexibility on particle board [25]. classification results which means that particle board with coating gives good and optimal results can cover the surface of the board so that no particle board bond is released on the surface and what is released is only the paint material [26].

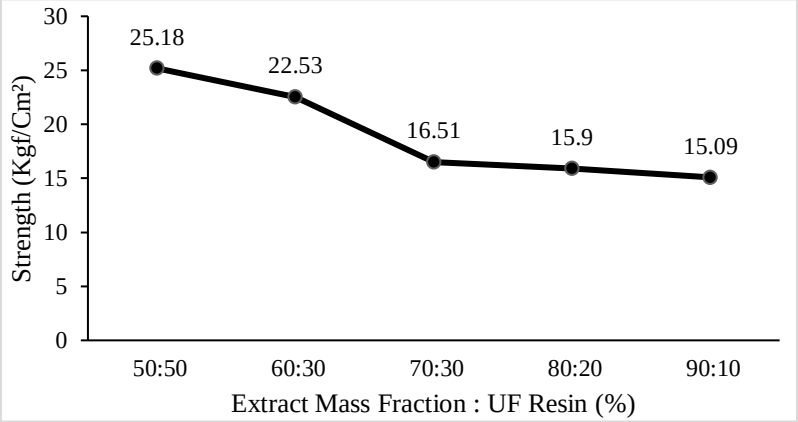

Figure 4. Flexural Strength Test Results for Anti-Termite Particle Boards

Termite Resistance

Termite resistance testing aims to determine the effect of Bintaro fruit seed extract contained in the particle board layer. This test refers to the SNI 01-7207-2006 standard. the effect of the composition of bintaro fruit seed extract and UF resin the resistance value of particle board to termites can be seen in Figure 5 which shows the relationship between the value of termite resistance on particle board with bintaro fruit seed extract as a coating. The particle board sample that had the highest termite resistance value was sample 5 (extract 50: UF 50 resin) with a termite resistance value of 0.86%. The lowest termite resistance value was sample 1 (extract 90: UF 10 resin) with a termite resistance value of 0.41%. The addition of Bintaro fruit seed extract coating to the composition of particle board manufacture affects the value of termite resistance. The value of termite resistance is higher for each sample, this is because the Bintaro fruit seed extract contains polyphenols and saponins which are toxic which function as termite exterminators , the more extracts used, the higher the resistance to termites [12] . Efforts to increase the resistance of particle board to termite attack are also carried out by providing a coating material on the surface of the particle board, besides aiming to improve the surface appearance of the board it also aims to protect this board from changes in humidity and attack by destructive organisms. According to [26].

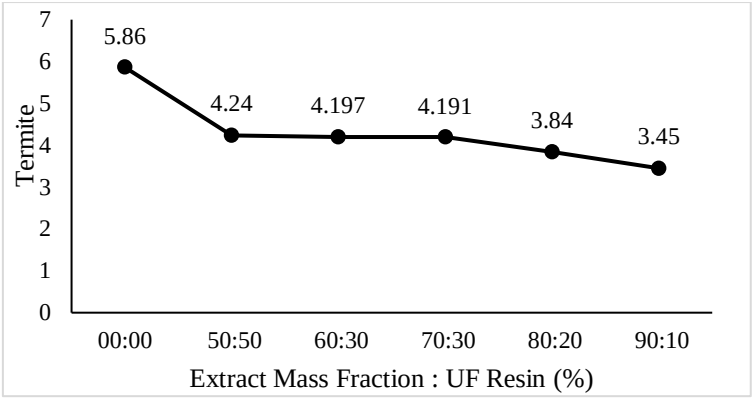

Figure 5. Test Results for Termite Resistance to Termite Particle Boards

CONCLUSION

Based on the research that has been done regarding the manufacture of particle board made from bintaro fruit fiber, UF resin and bintaro fruit seed extract as a particle board coating, it can be concluded that the effect of coating variations on bintaro fruit seed extract and UF resin on particle board on the physical properties test of density and water content complies with SNI 03-2105-2006 standards with a density value of 0.40% - 0.90% gr/cm^3 and the value of water content is not more than 14%. The effect of coating variations on bintaro fruit seed extract and UF resin on particle board on the mechanical properties test for flexural strength did not meet the SNI 03-2105-2006 standard with a flexural strength value of 82 Kgf/cm^2. Effect of coating variations on bintaro fruit seed extract and UF resin on particle board on termite resistance testing according to SNI 01-7207-2006 standards which are class 1 resistant category with a value of 2.0% -4.4%.

SUGGESTION

The flexural strength in the research that has been carried out does not meet the SNI 03-2105-2006 standard because the more extracts used in the coating, the lower the flexibility of the particle board. It is possible that adding more UF resin will add flexural strength to the particle board, because the resin UF has binding and hardness properties.

REFERENCE

[1] Yuliawati, S., Martini, M., & Savitri, A. (2016). Keanekaragaman Jenis Rayap Tanah Dan Dampak Serangan Pada Bangunan Rumah Di Perumahan Kawasan Mijen Kota Semarang. Jurnal Kesehatan Masyarakat (E-Journal). Volume 4, Nomor 1, Januari 2016 (ISSN: 2356-3346) Http://Ejournal-S1.Undip.Ac.Id/Index.Php/Jkm

[2] Purba, D. A. 2018. Sifat Fisis Dan Mekanis Papan Partikel Dari Beberapa Bahan Berlignoselulosa Dengan Perekat Isosianat Program Studi Teknologi Hasil Hutan. Skripsi. Fakultas Kehutanan.

[3] Raharjo, M. L, Amaliyah, D. M. 2020. Pengaruh Ekstrak Kayu Ulin (Eusideroxylon Zwageri) Terhadap Serangan Rayap Kayu Kering (Cryptotermes Cynocephalus Light). Jurnal Penelitian Hasil Hutan Vol. 38 No. 1, Maret 2020: 25-32.

[4] Yuliana, O, Y., Dan Alimin, M. 2020. Analisis Komposisi Serat Pinang Dan Serat Eceng (mendeley)Gondok Terdap Sifat Mekanik Komposit Hibridib Polipropena Degan Pati Talas. Jurnal Fisika Unand. Vol, 9. No, 1.Hal 24-30.

[5] Mahmuda. 2016. Hidrolisis Tandan Kosong Kelapa Sawit (Tkks) Oleh Aspergillus Sp. (Vtm1) Dan Pestalotiopsis Sp. (Vm9) Sebagai Media Tumbuh Pst Saccharomyces Cerevissiae. Skripsi. Universitas Jember.

[6] Sari, D. E., & Mahyudin, A. 2017. Pengaruh Persentase Serat Eceng Gondok Terhadap Sifat Fisik Dan Mekanik Papan Beton Busa. Jurnal Fisika Unand, 6(4), 381–386. Https://Doi.Org/10.25077/Jfu.6.4.381-386.2017.

[7] Lukmandaru, G., & Prayitno, (2015). Sifat Fisika Mekanika Dan Ketahanan Papan Partikel Bambun Dengan Perekat Asam Sitrat Terhadap Serangan Rayap Kayu Kering. Jurnal Keilmuan. Vol. 9. No 1

[8] Raharjo, M. L, Amaliyah, D. M. (2020). Pemanfaatan Limbah Tandan Kosong Kelapa Sawit Sebagai Bahan Pengganti Alternatif Papan Partikel Issn 2655 4887 (Print), Issn 2655 1624 (Online) Issn 2655 4887 (Print), Issn 2655 1624 (Online). 2(2), 1–9.

[9] Eko Puji Haryanto. 2016. Analisa Pelapisan Material Abs Dan Cat Uvilon Menggunakan Metode Uv Coating Untuk Mengetahui Karakteristik Dan Sifat Mekanis Lapisan. Skripsi. Jurusan Tehnik Mesin Lintas Jalur Universitas Muhammadiyah Semarang.

[10] Kholid, Widyastuti, & Fajarin, R. (2017). Pengaruh Variasi Komposisi Bam/Pani Matriks Cat Epoxy Pada Pelapisan Single Layer Dengan Metode Spray Coating Untuk Aplikasi Material Penyerap Radar. Jurnal Teknik Its, 6(2). Https://Doi.Org/10.12962/J23373539.V6i2.23832

[11] Setiawan, B. 2008. Kualitas Papan Partikel Sekam Padi. Skripsi. Departemen Hasil Hutan. Fakultas Kehutanan. Institut Pertanian Bogor. Bogor. Sostrohamidjo.

[12] Utami, S. 2010. Terhadap Hama Eurema Spp. Pada Skala Laboratorium Activities Of Bintaro (Cerbera Odollam Gaertn) Insecticide On Eurema Spp . Pest In Laboratory Scale. Jurnal Penelitian Hutan Tanaman, 7(4), 211–220.

[13] Ginting, D. dan Wulandari. Pengaruh Perlakuan Filler Serat Kulit Buah Pinang Menggunakan *Silane Coupling Agent* Terhadap Sifat Fisis dan Mekanis Papan Partikel. Program Studi Fisika, Fakultas MIPA dan Kesehatan, Universitas Muhammadiyah Riau, Indonesia. jurnal photon vol. 12 no 2.

[14] Sari, N. H., Taufan, A, & Yudhyadi, I. 2012. Ketahanan Bending Komposit Hybrid Serat Batang Kelapa/Serat Gelas Dengan Formaldehyde. Jurnal Energi Dan Manufaktur. 5(1), 91–97.

[15] Prayuda, Eka Yoga. 2014. Efikasi Ekstrak Biji Bintaro (Cerbera Manghas) Sebagai Larvasida Pada Larva Aedes Aegypti L.Instar Iii/Iv. Skripsi. Jakarta: Fakultas Kedokteran Dan Ilmu Kesehatan Uin Syarif Hidayatullah.

[16] Badan Standarisasi Nasional. (2006). Papan Partikel. *Standar Nasional Indonesia (Papan Serat)*, 1-23.

[17] Standar Nasional Indonesia [SNI], 2006, Uji Ketahanan Kayu dan Produk Kayu Terhadap Organisme Perusak Kayu. Jakarta: Badan Standarisasi Nasional 1-12

[18] Alghiffari, A.F. 2008. Pengaruh Kadar Resin Perekat Urea Formaldehida Terhadap Sifatsifat Papan Partikel dari Ampas Tebu.Skripsi. IPB. Bogor

[19] Abdurachman dan Nurwati, H. (2011). Sifat Papan Partikel dari Kulit Kayu Manis. Jurnal Penelitian Hasil Hutan. 29(2):128 - 141.

[20] Ainun Rohanah. 2017. Pembuatan Papan Partikel Berbahan Dasar Sabut Kelapa (Cocos

Nucifera L.). Fakultas Oertanian Usu. J. Rekayasa Pangan Dan Pert. Vol 5. No 3.

[21] Nasmi Herlina Sari, Sinarep, Ahmad Taufan, Ignk Yudhyadi. 2012. Ketahanan Bending Komposit Hybrid Serat Batang Kelapa/Serat Gelas Dengan Matrik Urea Formaldehyde. Fakultas Teknik Universitas Mataram. Jurnal Ilmiah Teknik Mesin Vol. 5 No.1. April 2011 (91- 97)

[22] Iswanto, A.H., Z. Coto dan K. Effendi. 2007.Pengaruh Perendaman Partikel terhadapSifat Fisis dan Mekanis Papan Partikel dari Ampas tebu (Saccarum officinarum). Jurnal Perennial. 4 (1), 6-9.

[23] Sadir, Muhammad,Ardiantari, Lale Dini Wanesi, Baiq Mawangi, Angguna Wulandari, Febriana Tri Studi. 2018. Program Universitas, Kehutanan Mataram. Jurnal Sangkareang Mataram. Vol 4. No. 2.

[24] Nuryawan, A, I Risnasari, PS Sinaga. 2009. Sifat-Fisis Mekanis Papan Partikel dari Limbah Pemanenan Kayu. Jurnal Ilmu dan Teknologi Hasil Hutan. Vol 2 (2): 57-63

[25] Rowell, R. M. 2005. Handbook Of Wood Chemistry And Wood Composites. Crc Press.New York.

[26] Lusita Wardani, Muhamad Yusram Massijaya. dkk. 2016. Kelas Keawetan Papan Zephyr Pelepah Sawit sebagai Bahan Bangunan dari Serangan Rayap. Jurnal Teknik Sipil ITB.

[27] Williams, R.S., 1999, Finishing of Wood, Wood Handbook: Wood as an Engineering Material, Madison: U.S. Department of Agriculture, 15- 37

Available online at:
Al-Fiziya: Journal of Materials Science, Geophysics, Instrumentation and Theoretical Physics
Website: http://journal.uinjkt.ac.id/index.php/al-fiziya
Vol.5 No. II Tahun 2022, 111 - 120

Calculating InN/GaN Transmission Coefficient from Single Barrier to Five Barriers with Propagation Matrix and Transfer Matrix Methods

Ishmah Ulya [1], Russell Ong [2], Yuan Alfinsyah Sihombing [1†]
[1]Department of Physics, Faculty of Mathematics and Natural Sciences, Universitas Sumatera Utara Medan, Jl. Dr. T. Mansur No.9, Padang Bulan, Kec. Medan Baru, Kota Medan, Sumatera Utara 20222, Indonesia
[2]Department of Physics, Faculty of Sciences and Technologies, Universitas Islam Negeri Sumatera Utara Medan, Jl. Lapangan Golf, Desa Durian Jangak, Kec. Pancur Batu, Kab. Deli Serdang, Sumatera Utara, 20353, Indonesia
[†]yuan@usu.ac.id

Submitted: Agustus 2022; Revised: September 2022; Approved: Oktober 2022; Available Online: Desember 2022

Abstract. In this study, the value of transmission coefficient on InN/GaN semiconductor from a single barrier to five barriers was determined by using the propagation matrix method and the transfer matrix method. This study aims to see the effect of adding a barrier to the number of resonance tunneling that occurs, to see the difference in transmission coefficient values which was obtained with the two methods, and to determine the effectiveness of the program execution process time from the propagation matrix and transfer matrix methods using Matlab programming. The results obtained indicated that the value of the transmission coefficient obtained from the two methods was the same. As the number of barriers increases, the number of resonance tunneling that occurs will increase. These two matrix methods had differences in terms of the effectiveness of the program execution process time and calculation process. The propagation matrix method was considered more effective than the transfer matrix method.

Keywords: *InN/GaN, Propagation Matrix Method, The Tunneling Effect, Transfer Matrix Method, Transmission Coefficient.*

DOI : *10.15408/fiziya.v5i2.28549*

INTRODUCTION

The tunneling effect is a microscopic phenomenon in which a particle can break through the barrier potential so that the particle can move freely after penetrating the barrier. This quantum phenomenon was applied widely to semiconductors. The probability that a particle can penetrate the barrier is expressed in terms of the transmission coefficient (*T*) [1]. Many studies have been carried out on the analysis of the transmission coefficient of various semiconductor materials with various numbers and types of barriers through various calculation methods. Agustin *et al.* have analyzed the tunneling effect of InN from a single barrier to three barriers with the conventional analytic method [2]. Huda *et al.* have used the propagation matrix method to analyze the tunneling effect in four barriers of graphene [3]. The propagation matrix method has

Copyright©2019, Published by **Al-Fiziya: Journal of Materials Science, Geophysics, Instrumentation and Theoretical Physics**
P-ISSN: 2621-0215, E-ISSN: 2621-489X

been used by Supriadi *et al*. to determine the transmission coefficient of three potential barriers which consisted of GaN, SiC, and GaAs [4]. Lolo has researched the tunneling resonance effect of $In_xGa_{1-x}As$/InP tensile strained with the method of transfer matrix [5].

The propagation matrix method is a method that is used to determine transmission and reflection coefficients by using matrix form. This method has the advantage that the process is the easiest to solve the problem of potential barriers in large quantities. This advantage appears because the analysis review area at any limit still returns to its initial state [6]. This method can be applied to various types of potential barrier shapes [7]. Another method called the transfer matrix method is a method that is used to solve second-order differential equations by using matrix form. It also can be used to determine transmission coefficient equations and can give efficient simulation that applied in many barriers cases because its implementation process was fast and its result was more accurate [8].

In this study, the equation of transmission coefficient on InN/GaN semiconductor from a single barrier to five barriers was determined by using two different numerical methods, namely the propagation matrix method and the transfer matrix method, and was simulated with Matlab programming. This study aimed to see the effect of adding a barrier to the number of resonance tunneling that occurs, to see the difference in transmission coefficient values which was obtained with the two methods, and to determine the effectiveness of the program execution process time from the propagation matrix and transfer matrix methods using Matlab programming.

RESEARCH METHODS

In this study, InN/GaN heterostructure was used as the barrier potential with the barrier's strength of 2.22 eV. This value was taken by the value of the conduction band offset of the InN/GaN heterostructure [9]. GaN was considered a barrier and InN was considered a well or a gap between barriers. The distance between barriers was taken from InN's lattice constant equal to 0.3533 nm and the width of barrier potential was taken from GaN's lattice constant equal to 0.3189 nm [10]. Effective electron mass inside and outside the barrier were 0.22 m_0 and 0.12 m_0 respectively [11]. The electron energy was smaller than barrier potential ($E < V$) with variation values from 0.003 eV to 2.0 eV. The simulation process was carried out using Matlab programming. The model of the InN/GaN barrier potential structure was shown in Fig. 1.

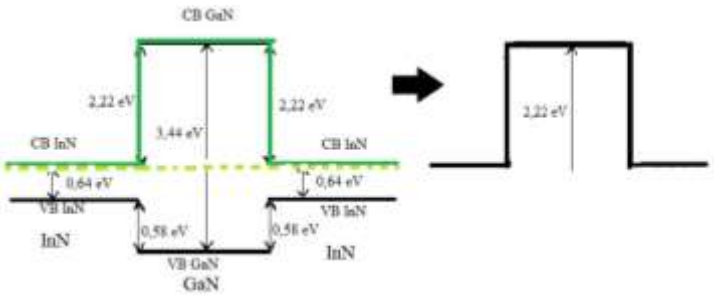

FIGURE 1. The model of an InN/GaN barrier potential structure.

RESULTS AND DISCUSSIONS

Transmission Coefficient Equation with Propagation Matrix Method

A single barrier potential was rectangular with a potential high of V_0 and a barrier width of L was described such as Fig. 2. On a heterostructure semiconductor, effective electron masses were different both inside and outside of the barrier. Effective electron mass inside the barrier was expressed by m_b. Whereas effective electron mass outside the barrier was expressed by m_w.

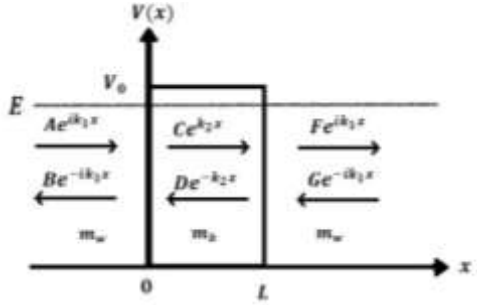

FIGURE 2. The Heterostructure Single Barrier Potential model ($m_w \neq m_b$)

The wave function equations on each area:

$$\psi_I = Ae^{ik_1x} + Be^{-ik_1x} \quad (1)$$

$$\psi_{II} = Ce^{k_2x} + De^{-k_2x} \quad (2)$$

$$\psi_{III} = Fe^{ik_1x} + Ge^{-ik_1x} \quad (3)$$

where $k_1 = \frac{(2m_wE)^{1/2}}{\hbar}$ and $k_2 = \frac{(2m_b(V_0-E))^{1/2}}{\hbar}$.

At the boundary *x=0*, the continuity condition was applied.

$$\psi_I|_{x=0} = \psi_{II}|_{x=0} \quad (4)$$

$$A + B = C + D \quad (5)$$

$$\frac{1}{m_w}\frac{d\psi_I}{dx}\Big|_{x=0} = \frac{1}{m_b}\frac{d\psi_{II}}{dx}\Big|_{x=0} \quad (6)$$

$$\frac{ik_1(A-B)}{m_w} = \frac{k_2(C-D)}{m_b} \quad (7)$$

Eq. (5) and Eq. (7) were converted in matrix form to

$$\begin{bmatrix} A \\ B \end{bmatrix} = \boldsymbol{P_{step-up}} \begin{bmatrix} C \\ D \end{bmatrix} \quad (8)$$

$$\boldsymbol{P_{step-up}} = \frac{1}{2}\begin{bmatrix} 1+\frac{m_wk_2}{m_bik_1} & 1-\frac{m_wk_2}{m_bik_1} \\ 1-\frac{m_wk_2}{m_bik_1} & 1+\frac{m_wk_2}{m_bik_1} \end{bmatrix} \quad (9)$$

Determining the propagation matrix for the propagation of wave function between $x = 0$ and $x = L$ with a barrier width of *L* ($\boldsymbol{P_{free}}$). The wave functions equation in this boundary was formed by Bloch's Theorem.

$$Ce^{k_2L} = F \quad (10)$$

$$De^{-k_2L} = G \quad (11)$$

Eq. (10) and Eq. (11) were converted in matrix form to

$$\begin{bmatrix} C \\ D \end{bmatrix} = \boldsymbol{P_{free}} \begin{bmatrix} F \\ G \end{bmatrix} \tag{12}$$

$$\boldsymbol{P_{free}} = \begin{bmatrix} e^{-k_2 L} & 0 \\ 0 & e^{k_2 L} \end{bmatrix} \tag{13}$$

Determining the propagation matrix on boundary $x = L$ ($\boldsymbol{P_{step-down}}$). This barrier consisted of step-up and step-down. Therefore, to analyze at $x = L$ boundary, it can be viewed back as the initial review when we determined $\boldsymbol{P_{step-up}}$ matrix at $x = 0$ before. $\boldsymbol{P_{step-down}}$ matrix could be obtain easily by replaced $\frac{m_w k_2}{m_b i k_1}$ became $\frac{m_b i k_1}{m_w k_2}$ in $\boldsymbol{P_{step-up}}$ matrix.

$$\boldsymbol{P_{step-down}} = \frac{1}{2}\begin{bmatrix} 1 + \frac{m_b i k_1}{m_w k_2} & 1 - \frac{m_b i k_1}{m_w k_2} \\ 1 - \frac{m_b i k_1}{m_w k_2} & 1 + \frac{m_b i k_1}{m_w k_2} \end{bmatrix} \tag{14}$$

Therefore, the propagation matrix of one unit barrier ($\boldsymbol{P_j}$) was

$$\boldsymbol{P_j} = \boldsymbol{P_{step-up}}\,\boldsymbol{P_{free}}\,\boldsymbol{P_{step-down}} \tag{15}$$

where $\boldsymbol{P_j}$ was 2 × 2 matrix form.

$$\boldsymbol{P_j} = \begin{bmatrix} p_{11} & p_{12} \\ p_{21} & p_{22} \end{bmatrix} \tag{16}$$

Numerically, the value of transmission coefficient could be determined by the equation

$$\begin{aligned} T &= \left|\frac{1}{p_{11}}\right|^2 \\ &= \left[1 + \frac{\left({k_1}^2 {m_b}^2 + {k_2}^2 {m_w}^2\right)^2}{4 {k_1}^2 {k_2}^2 {m_b}^2 {m_w}^2} \sinh^2(k_2 L)\right]^{-1} \end{aligned} \tag{17}$$

This equation was the transmission coefficient equation of single barrier potential case. For many barriers, total propagation matrix equation ($\boldsymbol{P}$) could be calculated by

$$\boldsymbol{P} = \boldsymbol{P_1 P_2} \ldots\ldots = \prod_{\boldsymbol{j=1}}^{\boldsymbol{j=N}} \boldsymbol{P_j} \tag{18}$$

where $\boldsymbol{P_j} = \boldsymbol{P_{step-up\ j}}\,\boldsymbol{P_{free\ j}}\,\boldsymbol{P_{step-down\ j}}$; $j = 1,2,3,4,5$.

Transmission Coefficient Equation with Transfer Matrix Method

With the same barrier model as in Fig. 2, the wave function of each region can be determined and the boundary conditions of each boundary plane can be imposed. Then, the equations that have been obtained can be made into a matrix form.

The matrix equation at *x=0* boundary was

$$\begin{bmatrix} 1 & 1 \\ 1 & -1 \end{bmatrix}\begin{bmatrix} A \\ B \end{bmatrix} = \begin{bmatrix} 1 & 1 \\ \frac{m_w k_2}{m_b i k_1} & -\frac{m_w k_2}{m_b i k_1} \end{bmatrix}\begin{bmatrix} C \\ D \end{bmatrix}$$

$$M_1 \begin{bmatrix} A \\ B \end{bmatrix} = M_2 \begin{bmatrix} C \\ D \end{bmatrix} \tag{19}$$

The matrix equation at *x=L* boundary was

$$\begin{bmatrix} e^{k_2 L} & e^{-k_2 L} \\ e^{k_2 L} & -e^{-k_2 L} \end{bmatrix} \begin{bmatrix} C \\ D \end{bmatrix} = \begin{bmatrix} e^{ik_1 L} & e^{-ik_1 L} \\ \frac{m_b i k_1}{m_w k_2}\, e^{ik_1 L} & -\frac{m_b i k_1}{m_w k_2}\, e^{-ik_1 L} \end{bmatrix} \begin{bmatrix} F \\ G \end{bmatrix}$$

$$M_3 \begin{bmatrix} C \\ D \end{bmatrix} = M_4 \begin{bmatrix} F \\ G \end{bmatrix} \tag{20}$$

Total transfer matrix equation of single barrier was

$$\begin{pmatrix} A \\ B \end{pmatrix} = M_1^{-1} M_2 M_3^{-1} M_4 \begin{pmatrix} F \\ G \end{pmatrix}$$

$$= M \begin{pmatrix} F \\ G \end{pmatrix} \tag{21}$$

Where matrix M was 2×2 matrix form.

$$M = \begin{bmatrix} M_{11} & M_{12} \\ M_{21} & M_{22} \end{bmatrix} \tag{22}$$

Numerically, the value of transmission coefficient could be determined by the equation

$$T = \left| \frac{1}{M_{11}} \right|^2$$

$$= \left[1 + \frac{((m_b k_1)^2 + (m_w k_2)^2)^2}{4 {k_1}^2 {k_2}^2 {m_b}^2 {m_w}^2} \sinh^2(k_2 L) \right]^{-1} \tag{23}$$

In the same way, the transmission coefficient equation for two, three, four, and five barriers can be determined by extending the total transfer matrix equation. We directly show the total transfer matrix for five barriers because one just need to simplify this equation for the less barriers cases. This equation is denoted by

$$\begin{pmatrix} A \\ B \end{pmatrix} = M_1^{-1} M_2 M_3^{-1} M_4 \ldots M_{17}^{-1} M_{18} M_{19}^{-1} M_{20} \begin{pmatrix} Y \\ Z \end{pmatrix} \tag{24}$$

where the model of five barriers was described such as Fig. 3.

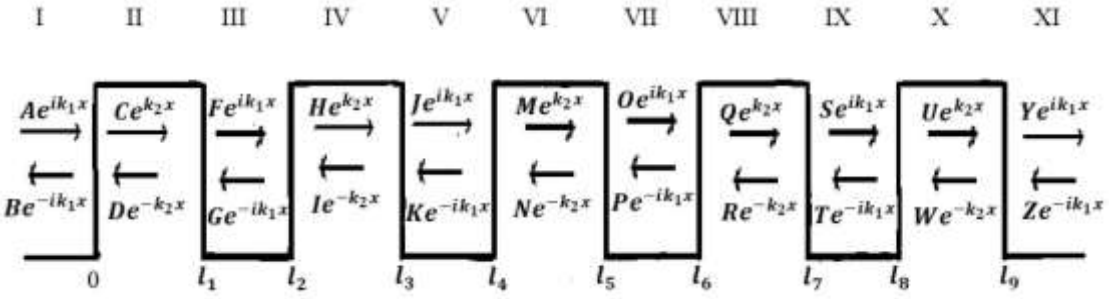

FIGURE 3. The Heterostructure Five Barriers Potential model ($m_w \neq m_b$)

Transmission Coefficient Simulation Results

Simulation of the tunneling effect was carried out on each multiple barriers using the propagation matrix and transfer matrix methods to obtain the transmission coefficient value. In this case, electron was coming from the left to the right of the barrier.

Simulation Result on Single Barrier Potential

Vol.5 No. II Tahun 2022, 111 - 120
P-ISSN: 2621-0215, E-ISSN: 2621-489X

The resulting transmission coefficient value on a single barrier, using the two different methods, was the same. The transmission coefficient increased exponentially up to 0.613 at an electron energy of 2.00 eV as shown in Fig. 4.

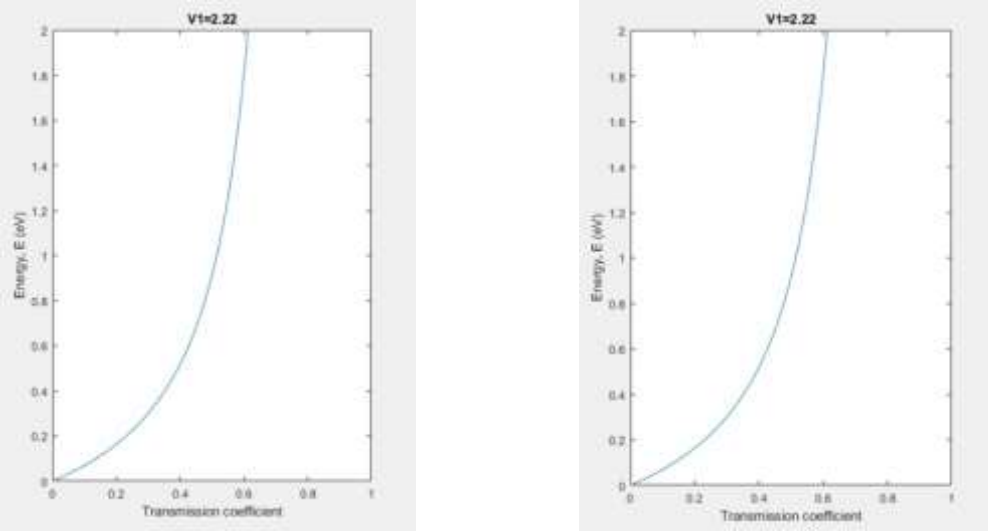

(a) (b)

FIGURE 4. Graph of the relationship between electron energy and transmission coefficient on a single barrier structure with (a) propagation matrix method and (b) transfer matrix method

Simulation Result on Two Barriers Potential

The resulting transmission coefficient value on two barriers, using the two different methods, was the same. The Transmission coefficient increased up to the maximum value of 0.961 at an electron energy of 2.00 eV as shown in Fig. 5.

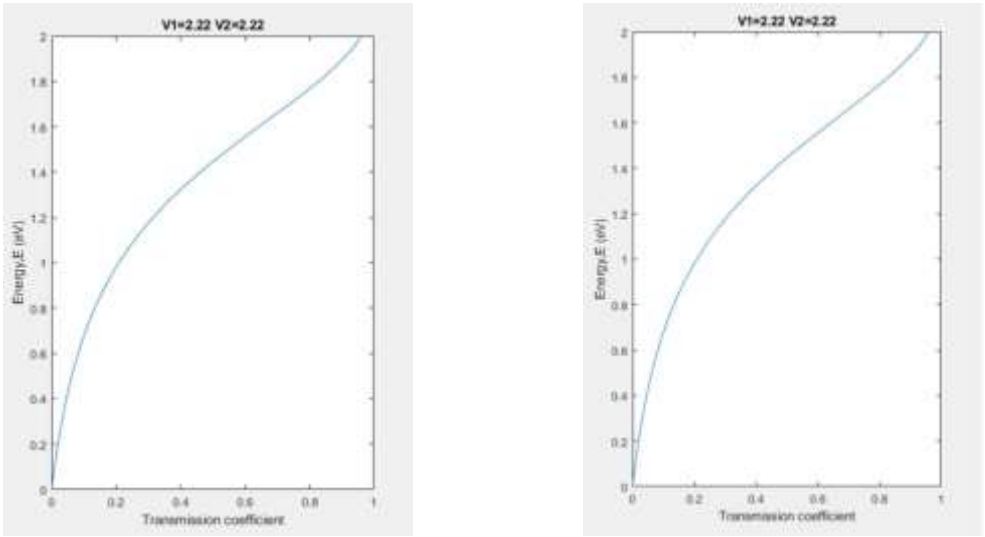

(a) (b)

FIGURE 5. Graph of the relationship between electron energy and transmission coefficient on two barriers structure with (a) propagation matrix method and (b) transfer matrix method

Simulation Result on Three Barriers Potential

Vol.5 No. II Tahun 2022, 111 - 120
P-ISSN: 2621-0215, E-ISSN: 2621-489X

The resulting transmission coefficient value on three barriers, using the two different methods, was the same. The transmission coefficient increased to the maximum value of 1 at an electron energy of 1.532 eV and it decreased to the value of 0.644 at an electron energy of 2.00 eV. The existence of a transmission coefficient value of 1, in this case, indicated that there was one resonance tunneling at an electron energy value of 1.532 eV as shown in Fig. 6.

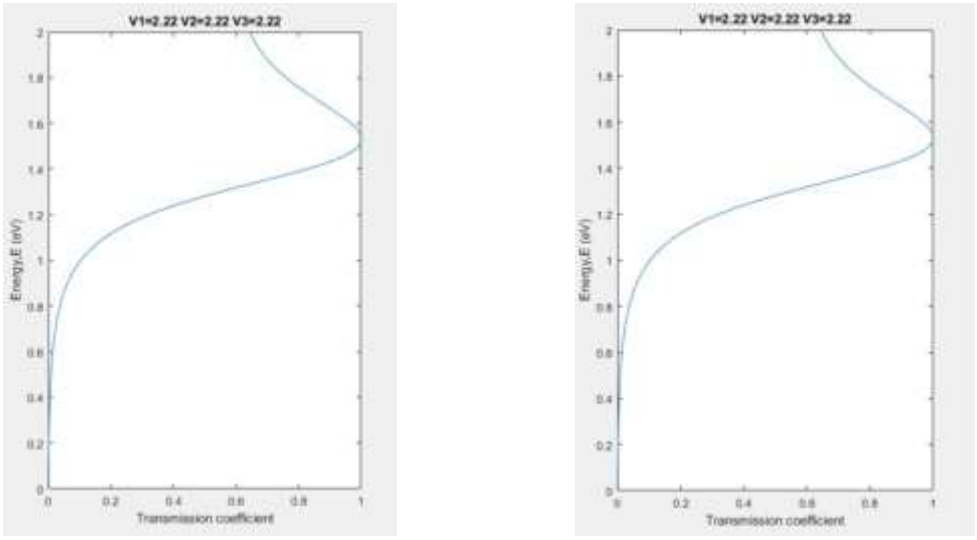

(a) (b)

FIGURE 6. Graph of the relationship between electron energy and transmission coefficient on three barriers structure with (a) propagation matrix method and (b) transfer matrix method

Simulation Result on Four Barriers Potential

The resulting transmission coefficient value on four barriers, using the two different methods, was the same. The transmission coefficient increased to the maximum value of 1 at an electron energy of 1.300 eV and it decreased to the value of 0.547 at an electron energy of 1.600 eV. Then, the transmission coefficient value rose to the value of 0.867 at an electron energy of 2.00 eV as shown in Fig. 7. This result indicated that there was one resonance tunneling at an electron energy value of 1.300 eV and the transmission coefficient value fluctuated with variations of electron energy.

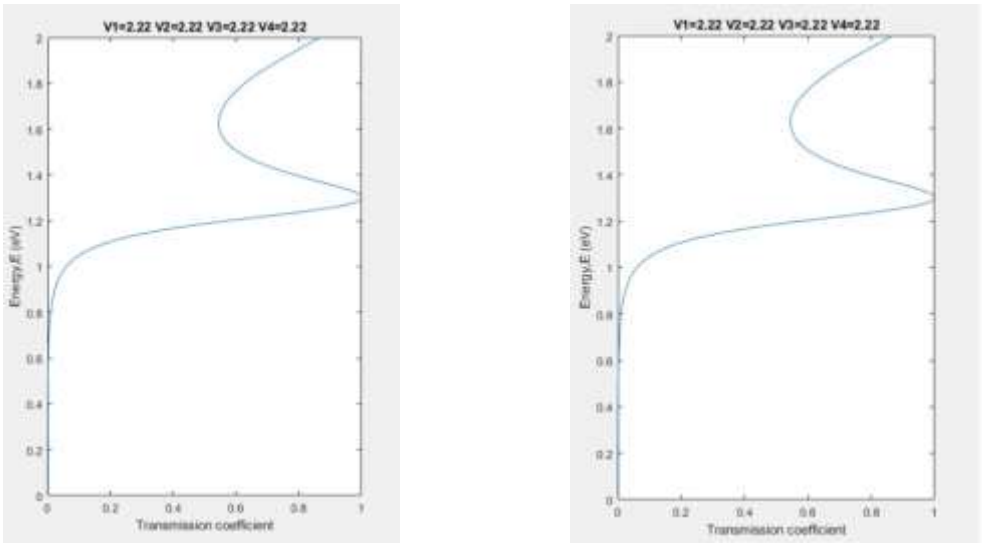

(a) (b)

FIGURE 7. Graph of the relationship between electron energy and transmission coefficient on four barriers structure with (a) propagation matrix method and (b) transfer matrix method

Simulation Result on Five Barriers Potential

The resulting transmission coefficient value on five barriers, using the two different methods, was the same as shown in Fig. 8.

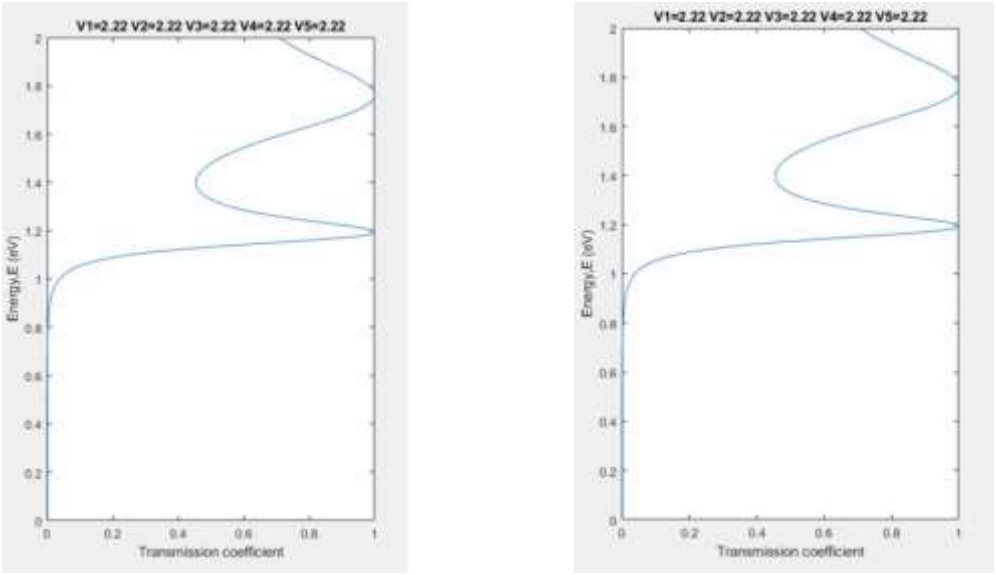

(a) (b)

FIGURE 8. Graph of the relationship between electron energy and transmission coefficient on five barriers structure with (a) propagation matrix method and (b) transfer matrix method

The transmission coefficient increased until it reached a maximum value of 1 at the electron energy value of 1.194 eV. After reached this value, transmission coefficient decreased to the value of 0.454 at an electron energy of 1.400 eV and grew up back to the maximum value of 1 at an electron energy of 1.762 eV before down to the value of

0.707 at an electron energy of 2.00 eV This result indicated that, in this case, resonance tunneling occurred twice at an electron energy value of 1.194 eV and 1.762 eV.

According to these results, it can be seen that transmission coefficient value that obtained from propagation matrix method and transfer matrix method had the same value in each electron energy variation. So that there was no difference in the value of the transmission coefficient between the two methods. Although there was no difference in the value of the transmission coefficient, these two methods had differences based on the effectiveness of the program execution process time and the implementation process in determining matrix equations.

Table 1. Average Program Execution Process Time from Single Barrier to Five barriers by using Propagation Matrix and Transfer Matrix Method

Number of Barriers	Average Program Execution Process Time (seconds)	
	Propagation Matrix Method	**Transfer Matrix Method**
One	$\pm$1.0	$\pm$34.6
Two	$\pm$1.0	$\pm$34.2
Three	$\pm$1.0	$\pm$34.2
Four	$\pm$1.0	$\pm$35.2
Five	$\pm$1.0	$\pm$35.0
Average	**$\pm$1.0**	**$\pm$34.64**

Based on Table 1. It can be seen that program execution process with propagation matrix method took approximately one second. While the transfer matrix method required approximately 34.64 seconds. It can be shown that the propagation matrix method was considered to be more effectively applied in computational simulations than the transfer matrix method.

The addition of the number of barriers affected the amount of resonance tunneling that occurs in InN/GaN semiconductors. The more we add the barriers, the more resonant tunneling will occur at certain energy values. The value of the transmission coefficient fluctuated with variations in electron energy as in the results of previous studies [2].

CONCLUSIONS

The values of the InN/GaN transmission coefficient from a single barrier to five barriers have been obtained by using the propagation matrix method and the transfer matrix method. The more we add the barriers, the more resonant tunneling will occur at certain energy values. There was no difference in transmission coefficient values which was obtained with the two methods. These two matrix methods have differences in terms of the effectiveness of the program execution process time and calculation process. The propagation matrix method was considered more effective than the transfer matrix method.

ACKNOWLEDGMENTS

We gratefully acknowledge Chilwatun Nasiroh, S. Pd., Nur Muhammad Fahmi, S. Si., and Idham Syah Alam, M. Sc., Ph. D. for useful discussions.

REFERENCES

[1] M. K. Huda, "Studi Analisis Quantum Tunneling Tiga Potensial Penghalang Graphene dengan Metode Propagasi Matriks pada Partikel Tunak," Universitas Jember, 2019.

[2] N. C. Agustin, C. I. W. Nugroho, and M. A. Pratama, "Koefisien Transmisi InN (Indium Nitrit) Penghalang Tunggal Hingga Penghalang Tiga dengan Metode Schrodinger," vol. 4, no. 1, pp. 102–106, 2019.

[3] M. K. Huda, S. H. B. Prastowo, and Z. R. Ridlo, "Analisis Efek Terobosan Empat Perintang pada Graphene," *Semin. Nas. Pendidik. Fis. 2018*, vol. 3, no. 2, pp. 153–158, 2018.

[4] B. Supriadi, Z. R. Ridlo, Yushardi, C. I. W. Nugroho, J. Arsanti, and S. Septiana, "Tunnelling Effect on Triple Potential Barriers GaN , SiC, and GaAs," *IOP Conf. Ser. J. Phys.*, pp. 1–8, 2019, doi: 10.1088/1742-6596/1211/1/012034.

[5] J. A. Lolo, "Studi Numerik Efek Resonansi pada Sumur Kuantum (QWs) In x Ga 1-x As / InP Tensile Strained," Universitas Hasanuddin, 2013.

[6] N. Rizky, "Analisis Hubungan Jarak Antar Penghalang Ganda dengan Koefisien Transmisi dan Koefisien Refleksi," Universitas Jember, 2020.

[7] A. F. J. Levi, *Applied Quantum Mechanics*, Second Edi. Cambridge: Cambridge University Press, 2006.

[8] O. Pujol, R. Carles, and J. P. Perez, "Quantum propagation and confinement in 1D systems using the transfer- matrix method," *Eur. J. Phys.*, vol. 35, pp. 1–26, 2014, doi: 10.1088/0143-0807/35/3/035025.

[9] P. D. C. King, T. D. Veal, C. E. Kendrick, L. R. Bailey, S. M. Durbin, and C. F. Mcconville, "InN /GaN Valence Band Offset: High-Resolution X-Ray Photoemission Spectroscopy Measurements," *Phys. Rev. B*, vol. 78, pp. 1–4, 2008, doi: 10.1103/PhysRevB.78.033308.

[10] M. Levinshtein, S. Rumyantsev, and M. Shur, *Properties of Advanced Semiconductor Materials: GaN, AlN, InN, BN, SiC, SiGe*. New York: John Wiley and Sons, Inc., 2001.

[11] L. Chen, K. Chen, and C. Chen, "Group III- and Group IV-Nitride Nanorods and Nanowires," in *Nanowires and Nanobelts: Materials, Properties, and Devices*, vol. 1, Z. L. Wang, Ed. New York: Springer, 2003, pp. 257–315.

Available online at:
Al-Fiziya: Journal of Materials Science, Geophysics, Instrumentation and Theoretical Physics
Website: http://journal.uinjkt.ac.id/index.php/al-fiziya
Vol.5 No. II Tahun 2022, 121 - 133

Analysis of Landslide Potential Using Resistivity, Geology and Climatology Values in Samangki Village, Simbang District, Maros Regency

Ahmad Haan [1], Ayusari Wahyuni [2], Muh. Said L [3], Rahmaniah [4]

[123]Jurusan Fisika, Universitas Islam Negeri Alauddin Makassar, Makassar, Indonesia

ahmadalileah@gmail.com

Submitted: September 2022; Revised: Oktober 2022; Approved: November 2022; Available Online: Desember 2022

Abstract. Research has been carried out that aims to determine the analysis of landslide potential using resistivity, geology, and climatology values in Samangki Village, Simbang District, Maros Regency.This study uses the resistivity method of the wenner configuration on three tracks of 120 meters at a distance between the electrodes of 10 meters. Interpretation results obtained resistivity values on the first track between 61,1-972 Ω.m, on the second trajectory of 58,2 - 666 Ω.m, and on the last track the resistivity value of the range 60,1 - 1105 Ω.m, which indicates the presence of limestone inserts sandstone and aquiver scattered on each track. Then combined with secondary data in the form of rainfall maps, geological maps and soil type maps. The results of the analysis then show that the location of this research is in an area prone to landslides according to primary data or field data and secondary data from the five parameters mentioned above.

Keywords: *Geoelectric, Wenner Configuration, Resistivity*
DOI : *10.15408/fiziya.v5i2.29004*

INTRODUCTION

Indonesia is a country that cannot be separated from natural disasters such as landslides, volcanic eruptions, earthquakes, and floods. Moreover, one that often happens in Indonesia is landslides. A landslide is one of the natural geological disasters that can cause huge losses ranging from material losses such as roads, settlements, agricultural land, bridges, irrigation canals, and other infrastructure to causing fatalities.

Maros Regency is geographically located between 119°30'00''-120°0'0'' East Longitude and 4°50'0''-5°10'0'' South Latitude. The geological conditions of Maros Regency, especially Simbang District, consist of hilly areas with volcanic rock, intrusive rock, igneous rock, and sedimentary rock as their constituent rocks. In this range, the average rainfall for Maros Regency is high, with such geological conditions and rainfall that Samangki Village, Simbang District, Maros Regency is very vulnerable to landslides (RP12-JM, 2014).

Copyright©2019, Published by **Al-Fiziya: Journal of Materials Science, Geophysics, Instrumentation and Theoretical Physics**
P-ISSN: 2621-0215, E-ISSN: 2621-489X

In addition to geological conditions and rainfall, the slope of the slope is a factor that also influences the occurrence of landslides. BMKG Maros data states that Maros Regency, with a slope of > 40% with a percentage of 30%, is located in the east. With this slope, Maros Regency, especially in the east, which is the location of this research, is very prone to landslides. For example, in January 2021, there was a landslide on the Maros-Bone flyover, which is not far from the research area, which caused the disconnection of Maros-Bone road access which had an impact on various factors. This motivates the author to conduct this research to minimize unwanted things in the future.

The concept of geology states that soil is a weathered layer of the earth's crust. Soil is the result of the transformation of mineral and organic substances on the surface of the earth's land, and soil is formed under the influence of environmental factors that work for a very long time. Soil is a heterogeneous and diverse component of soil mixing, namely the solid phase (mineral materials and organic matter), the liquid phase (soil moisture and groundwater), and the gaseous phase (soil air) (Susanto, 2005).

The function of the soil is to distribute food to plants through the roots so they can grow and develop and channel the things plants need to grow, namely substances that accelerate plants, such as vitamins, hormones, acids, etc. Another function is as a place to live for living things below the surface of the soil and provide primary and secondary needs for living things below the surface of the soil. In addition to having a positive impact, on the one hand, it also harms plants, including pests and diseases, both directly and indirectly (Herry, 2016).

Soil also has a classification and morphology, which are part of the pedology. As for the morphological, chemical, physical, and biological properties of the soil, from these properties, the soil is grouped into certain classes and characteristics so that it can be used to describe the soil itself. The results of the classification, then through observation, will produce the final result, namely in the form of a map of the land distribution according to the classification (Rayes, 2017).

METHOD

The tools and materials used in this study were a set of geoelectric tools, geological data for the Simbang sub-district, slope data for the Simbang sub-district, rainfall data for the Sambang sub-district, soil type data and land use data for the Sambang sub-district.

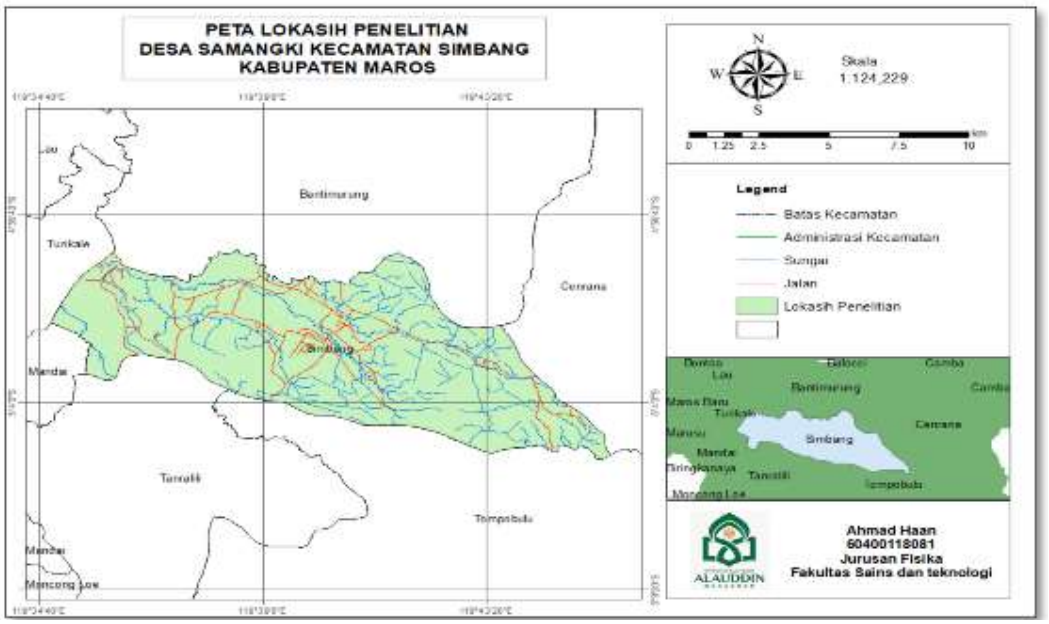

Figure. 1 research sites

The research method was carried out using the resistivity method and the climatological method, while the data between the two methods are as follows:

1. Resistivity Method
   Using the Wenner configuration Resistivity Data
2. Climatological Method
   a. Geological data of the study area
   b. Slope data
   c. Rainfall data
   d. Land use data and
   e. Soil type data

RESULTS AND DISCUSSIONS

a. Resistivity Data Processing

1. First Track

On track 1 it is carried out at coordinate points at South Latitude 08 ˚03'14.0" and West Longitude 119 ˚43'24.4" with an altitude > 1000 meters above sea level. On this track a stretch of 120 m is used with the smallest spacing of 10 m, with a Wenner configuration, on this track there is a low resistivity zone at a distance (x) 25 m to 40 m with a resistivity value of $61.1 < \rho < 135$ Ωm, which indicates the presence of layers of clay, sand and gravel, which indicates the presence of groundwater as a fluid to fill the rock pores. The following is table 4.1 to show more clearly the first track interpretation data:

Table 1: The resistivity value obtained in the first pass

No	Material	Nilai resistivitas (Ω.m)	Kedalaman (m)	Warna
1.	Akuifer	61,1 - 136	7,50 – 12,8	
2.	Batupasir	200 – 441	12,8 – 18,5	
3.	Batugamping sisipan batupasir	655 – 972	18,5 – 24,9	

The results of the 2-D cross-section inversion using Res2dinv software can be seen in the following figure:

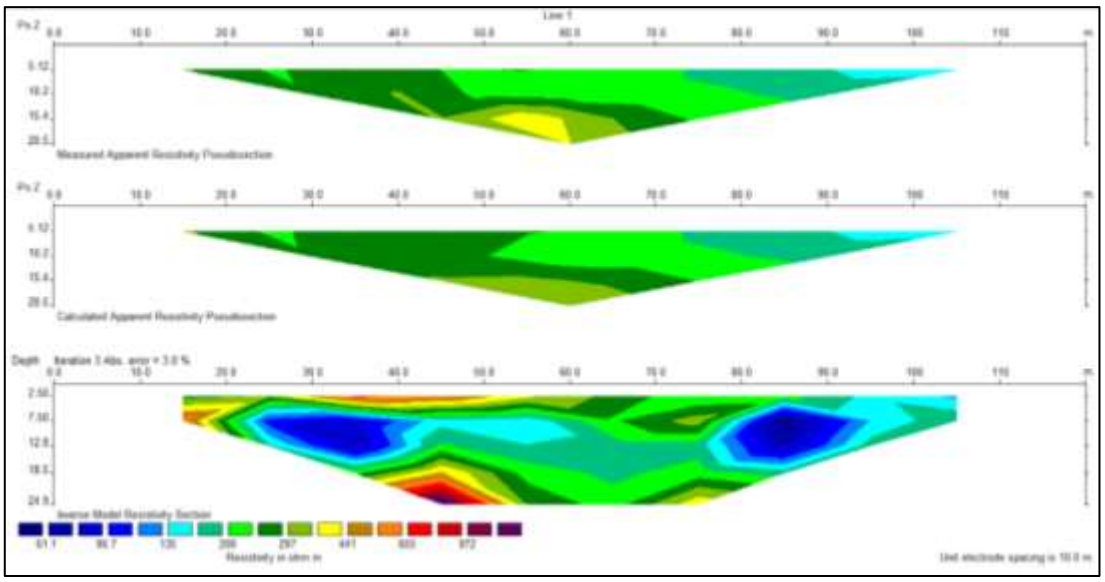

Figure. 8 Resistivity cross-section on track-1

Also, there is a high resistivity zone with a range of resistivity values between 441<ρ<972 Ωm, which indicates the existence of a granitic layer with sand inserts located at a distance of 50 m with a thinning stretch to the east. Maros, the intensity of rainfall at this location is relatively high on this track, while the topographic cross-section on track 1 is as follows:

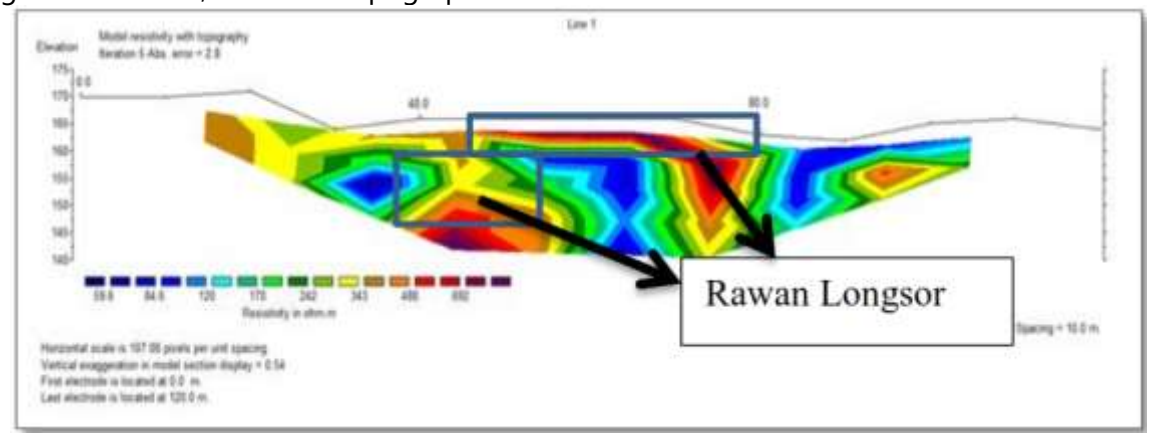

Figure. 9 Topographic cross-section on track-1

Based on the figure in 4.3, the first cross-section has a resistivity value of 61.5 - 972 Ωm, while the red color in the cross-section above is found at a depth of 18.5 - 24.9 m with a length of 40 - 50 m. It is suspected that there is inset limestone and sandstone with a value resistivity between 655 - 972 Ωm, so from the results of the cross-sectional analysis above, this location is suspected of having the potential for landslides. Limestone itself is a sedimentary rock composed chiefly of calcium which comes from the remains of marine organisms such as shells, sea slugs, and dead coral.

2. Second Track

As with the first track, on the second track, there is a high resistivity zone with a resistivity value range between 398<ρ<666 Ωm, which indicates the presence of a granitic layer with sand inserts located at a distance of 50-85 m with a thinning stretch towards east. The following table 4.2 shows more clearly the second path interpretation data:

Table 2: The resistivity value obtained in the second pass

No	Material	Nilai resistivitas (Ω.m)	Kedalaman (m)	Warna
1.	Akuifer	18,2 – 50,8	2,50 – 7,50	
2.	Batupasir	85,0 – 238	7,50 – 12,8	
3.	Batugampingan sisipan batupasir	398 – 666	7,50 – 24,9	

The results of the 2-D cross-section inversion using Res2dinv software can be seen in the following figure:

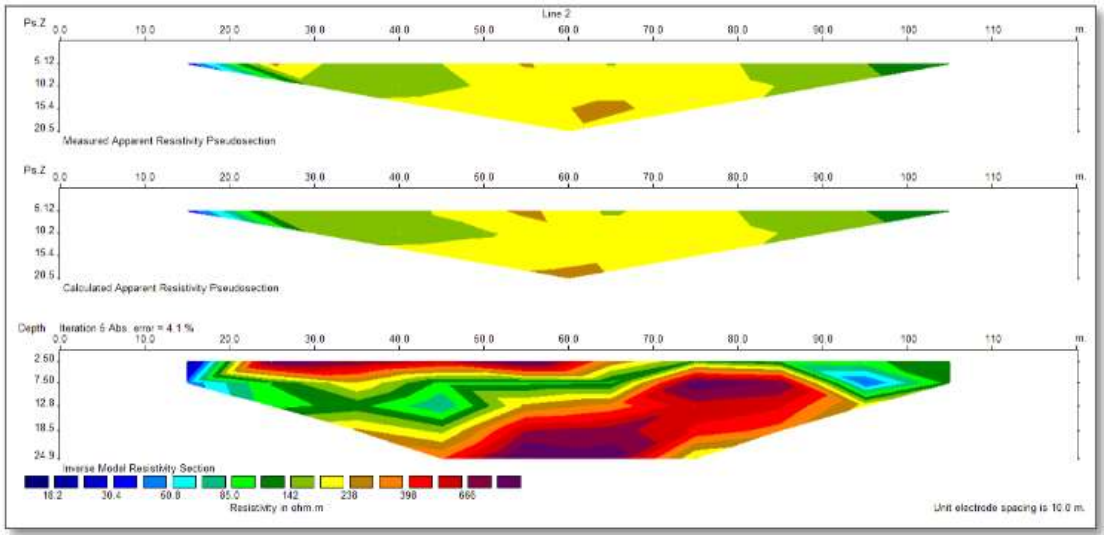

Figure. 10 The resistivity section on track-2

In addition, there is also a low resistivity zone at a distance of (x) 10 m to 20 m with a resistivity value of 18.2<ρ<50.8 Ωm, which indicates the presence of layers of clay, sand, and gravel, which indicates the presence of groundwater as a filling fluid. The rock pores, while the topographic cross-section on track 2 is as follows:

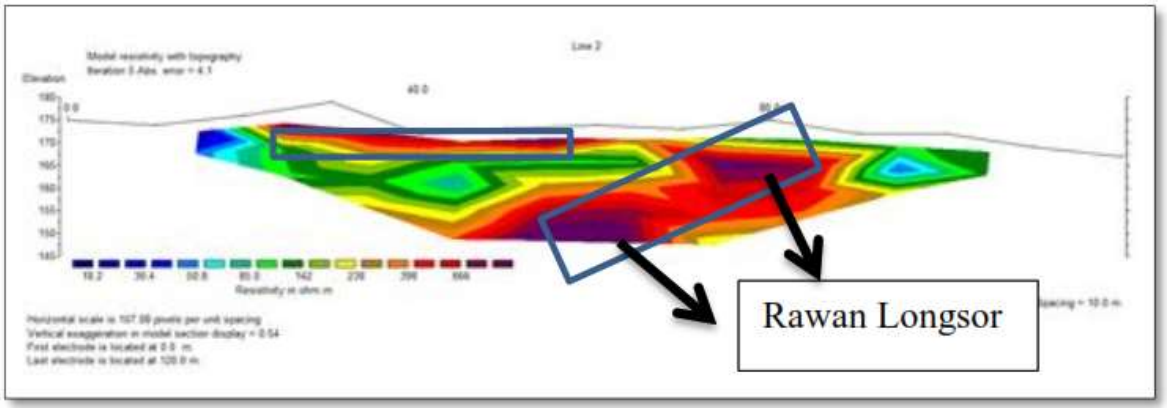

Figure. 11 Topographic cross section on track-2

Based on the figure in 4.4, the second section has a resistivity value of 18.2 - 666 Ωm, while the red color in the section above is found at a depth of 7.50 - 24.9 m with a length of 50 - 90 m. It is suspected that there are inset limestone and sandstone with a value resistivity between 238 - 666 Ωm, so from the results of the cross-sectional analysis above, this location is suspected of having the potential for landslides.

3. Third Track

The third track is different from the previous track on the first and second track because, on this track, there is only a low resistivity zone at a distance of (x) 25 m to 80 m. It is also present at a distance of 90 m to 110 m, with a resistivity value of 60,1<ρ<138 Ωm, which indicates the presence of clay layers. The following is table 4.3 to shows more clearly the interpretation of the third trajectory data:

Table 3: The resistivity value obtained in the third pass

No	Material	Nilai resistivitas (Ω.m)	Kedalaman (m)	Warna
1.	Akuifer	60,1 – 138	2,50 – 18,5	
2.	Batupasir	209 – 481	2,50 – 12,8	
3.	Batugamping sisipan batupasir	729 – 1105	18,5 – 24,9	

The results of the 2-D cross-section inversion using Res2dinv software can be seen in the following figure:

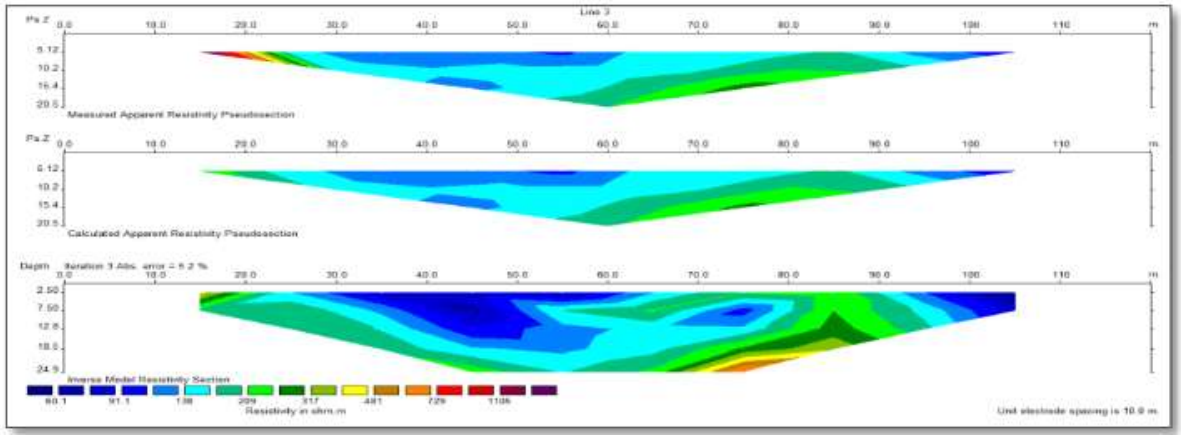

Figure. 12 The resistivity section on track-3

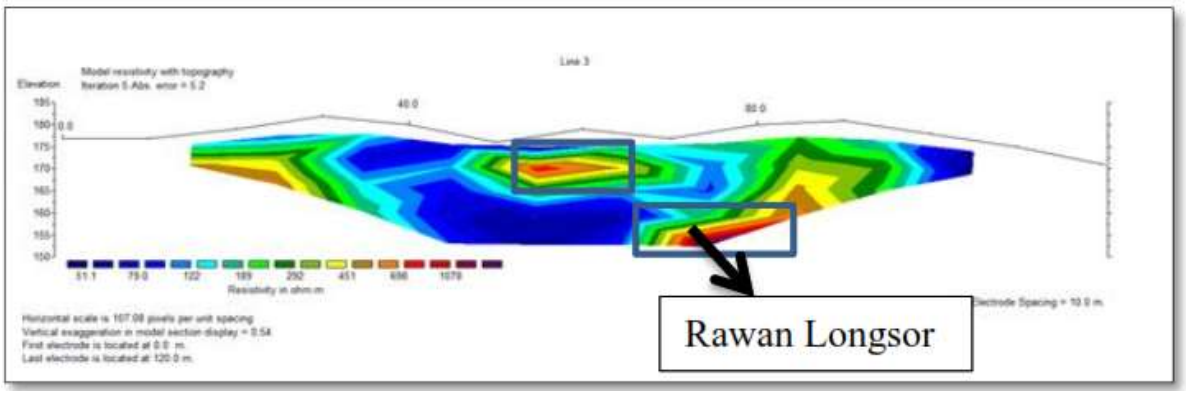

Figure. 13 Topographic cross-section on track-3

Based on the figure in 4.6, the third section has a resistivity value of 51.1 - 1078 Ωm, while the red color in the section above is found at a depth of 18.5 - 24.9 m with a length of 70 - 80 m. It is suspected that there are inset limestone and sandstone with a value the resistivity between 481 - 1105 Ωm, so from the results of the cross-sectional analysis above, this location is suspected of having the potential for landslides because limestone itself is a rock that easily allows water to pass so that the water that escapes easily carries the material in its path and causes landslides.

b. Geology

1. Geological Conditions

The geological map was obtained from the Maros Regency SHP, which was narrowed down to Simbang District. The data was processed in Arcgis so that a geological map could be obtained, which was used to determine the types of rocks in Simbang District.

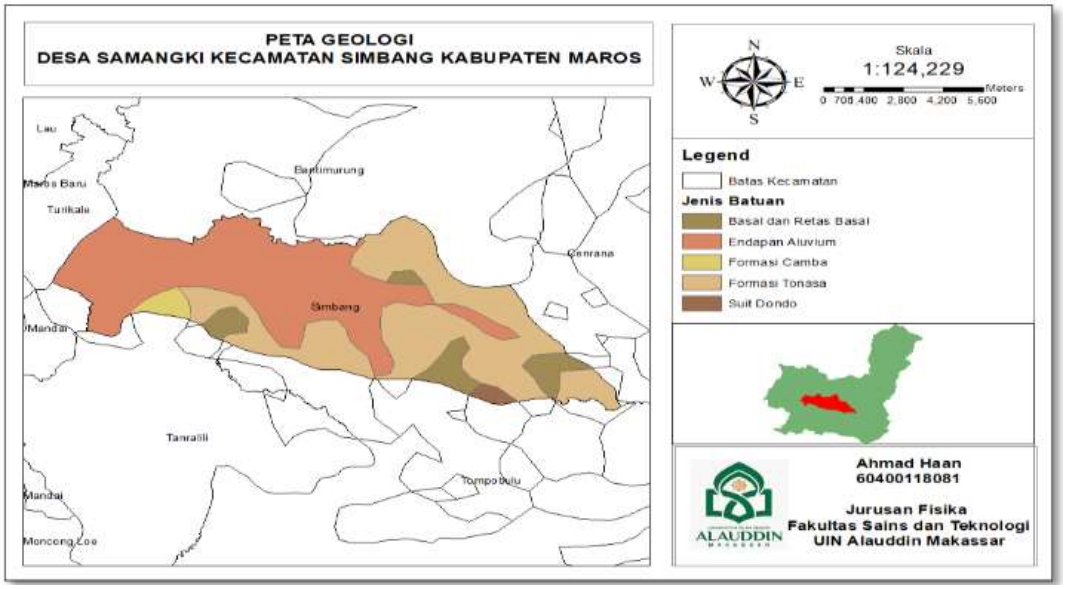

Figure. 14 Geological Map of Sambang District

Based on the attributes of the geological map 5.6 above, there are four types of constituent rocks found in Simbang District, namely basalt rock with a distribution area of 10%, alluvium sedimentary rocks with a distribution area of 50%, camba formation rocks with a percentage of 5%, and tonnage formations with a percentage of 35%.
Based on the data above, the geological structure that makes up the area is sedimentary rock types of limestone and shale. Where these rock types have the potential to cause ground movement because these rocks easily allow water to pass through. Moreover, if the soil or rocks above easily allow water to pass, coupled with the area having a slope, the water will be retained and cause the formation of slip planes which trigger landslides.

2. Slope

The slope map was obtained using the 2021 SHP data. The National Demographic Data used is the National Demographic Data for the province of South Sulawesi, which is then narrowed down to Samangki Village, Simbang District, Maros Regency, then processed in Arcgis.

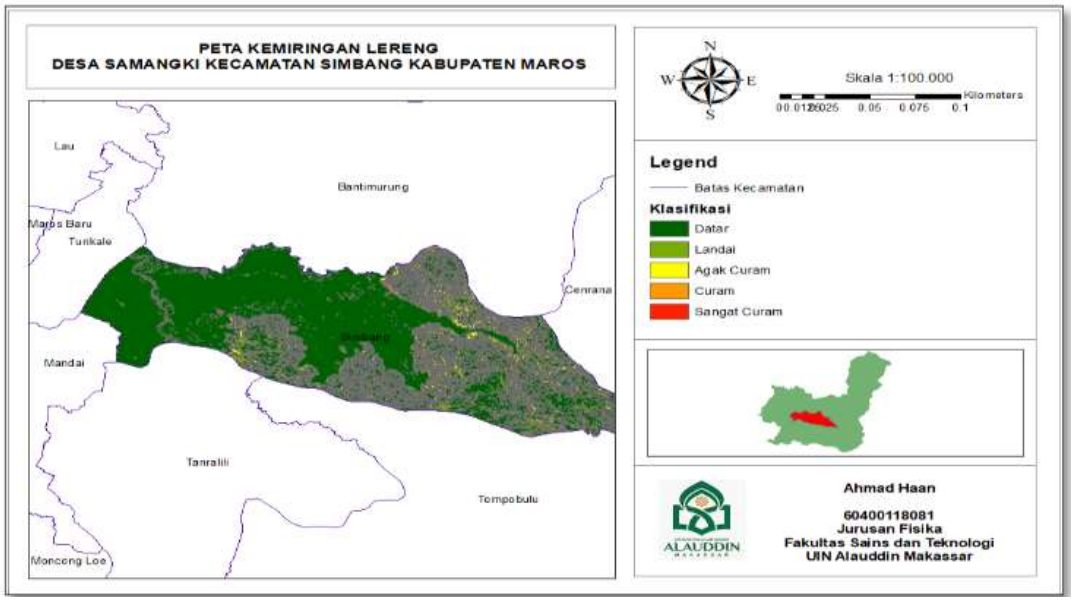

Figure. 15 Slope Map

Based on the attribute results from map 5.5 in Samangki village, Simbang District, Maros Regency, where for a slope of 0 - 8% with a distribution area of 4%, for a slope of 8 - 15%, it has a distribution area of 11%, for a slope of 15 - 25% it has a distribution area namely 25%, for a slope of 25 – 45% it has a distribution area of 20%. The slope map aims to see the general level of the slope of the land, which as a reference, determines the potential for landslides.

3. Type of soil

The soil type map was obtained from the Maros Regency SHP data, which was narrowed down to Simbang District. The data obtained were then processed in Arcgis.

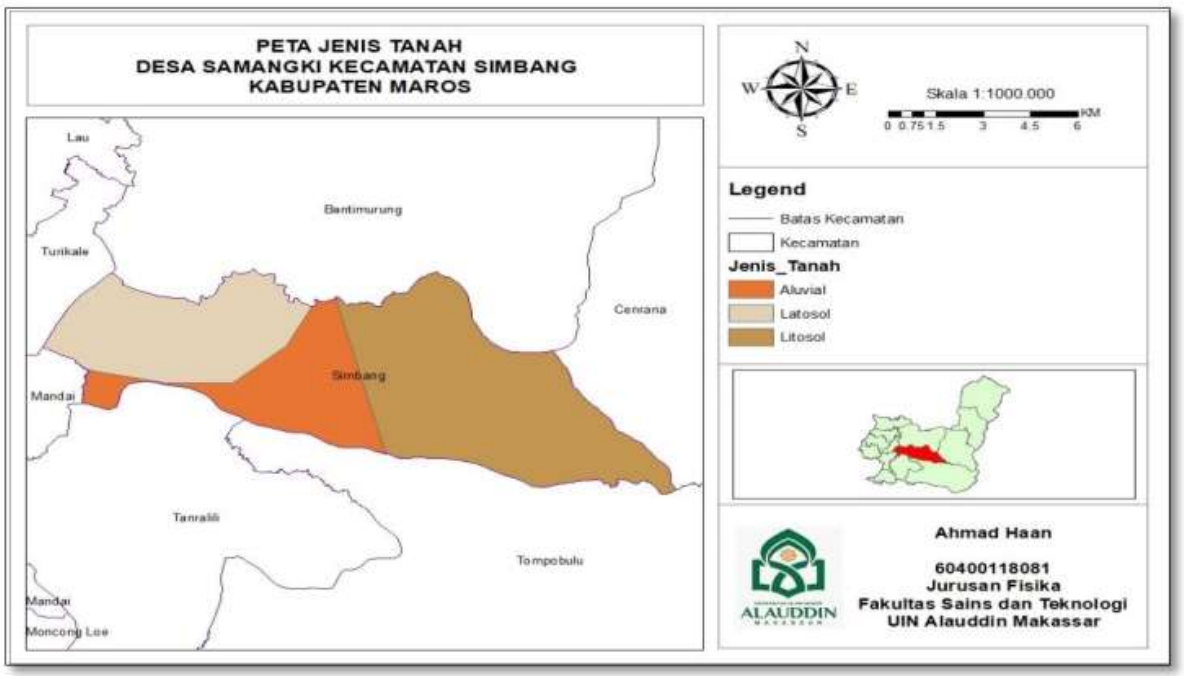

Figure. 16 Map of Soil Types of Simbang District

Based on the results of the data on attribute map 5.7 of the soil types above, it can be obtained that the most extensive soil types in Samanki Village are litosol soils with a distribution of 50%, Alluvial soil types with a distribution area of 20%, and Latosol soil types with a land area of 30%. Where litosol type soil is a type of soil formed from the weathering process of igneous rocks and sediments, litosol soil is characteristic of coarse grains in the form of gravel. In contrast, this type of soil is clay, sand, and silt are very young soil types to allow water to pass through. If this type of soil is above certain rocks or watertight with a particular slope, it can form a slip plane with the potential for landslides.

4. Land Use

The land use map was obtained from the results of an overlay between the SHP of land use in the province of South Sulawesi and the administrative SHP of the Maros Regency.

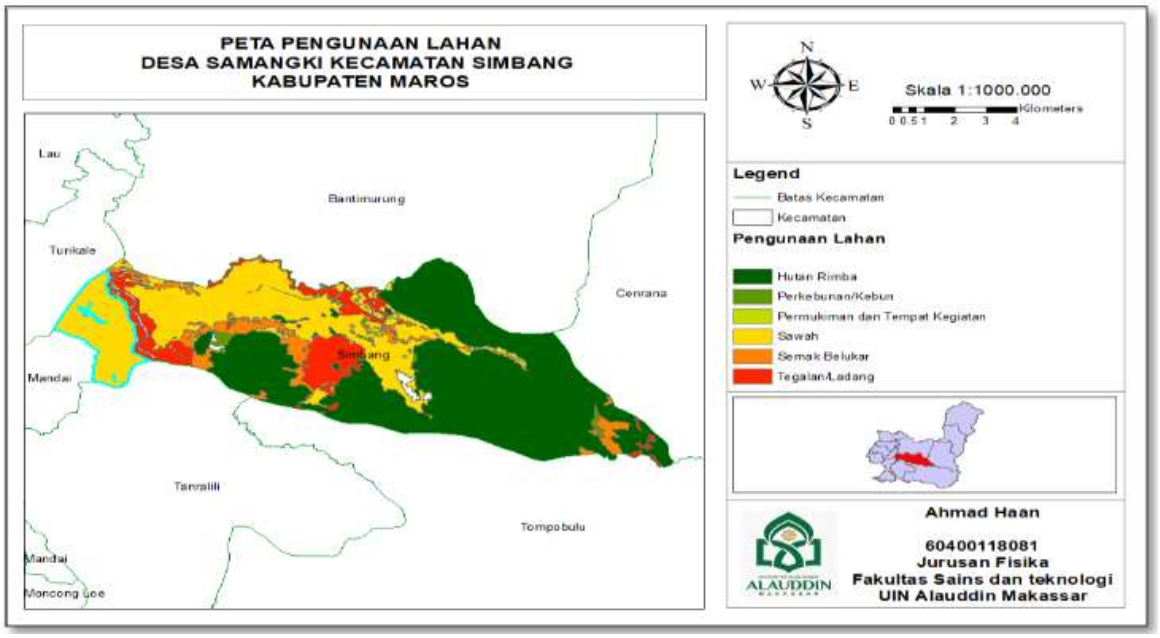

Figure. 17 Land Use Map of Simbang District

Then the two data were cut to produce a land use map for Maros Regency. To determine the level of vulnerability to landslides, a land use map is needed as supporting data. Landslides are prone to occur in areas with open land, rice fields, and cultivation and areas with stagnant water and steep slopes. So to make a landslide risk zone map, land use data is needed. This land use data is a reference to find out how prone the area is to landslides by taking into account the parameters mentioned above.

c. Climatology

Rainfall data were obtained from the BMKG Maros Station for the last five years, from 2017 to 2021. The data sent from the BMKG contained three stations, but this research was located in Maros Regency, so researchers used Maros Regency stations in this thesis. The results obtained are under the theory, where the characteristics of rainfall that trigger landslides have been used to establish a relationship between rain and soil in various parts of the world, including shallow landslides. Rainfall parameters include previous rainfall, intensity, and duration (Hasnawir, 2011).

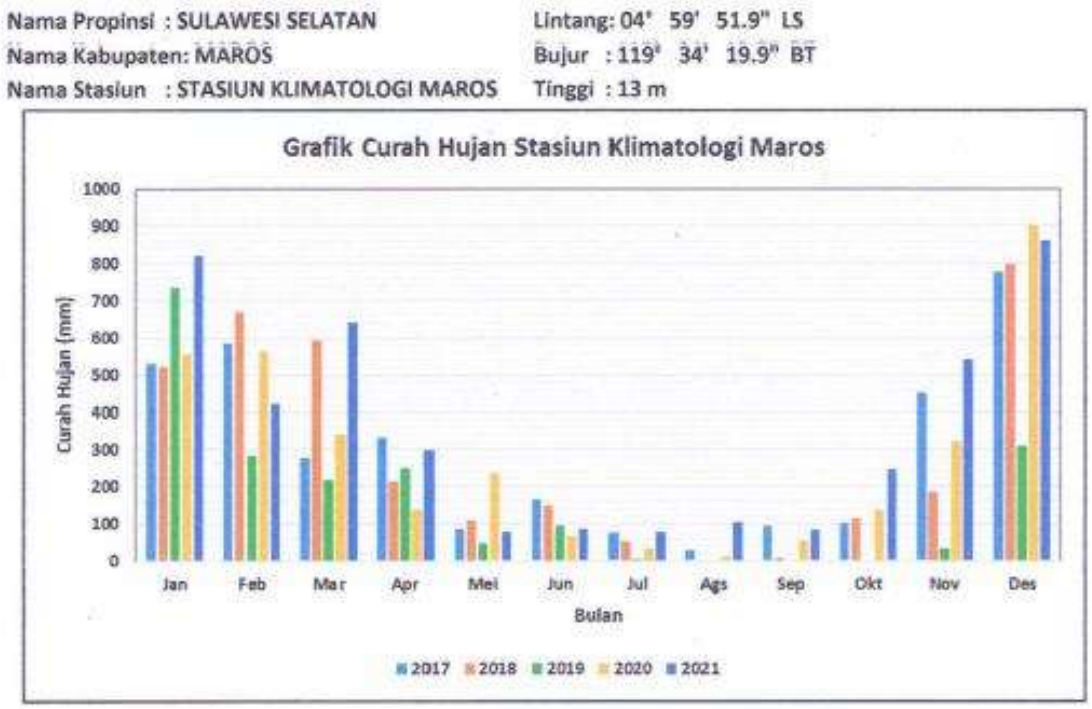

Figure. 18 Graph of Maros Regency rainfall for 2017-2021

Based on the graph above, relatively moderate to high rainfall can have the potential for landslides because it is seen from the type of soil and rock in the study area where the type of soil/rock in the area has high porosity or soil/rock that easily allows water to pass through. These properties cause the soil/rock to gain weight if there is continuous rain, and it is exacerbated by the steep slope conditions, which result in easy landslides.
Based on data from the Maros BMKG station in 2017-2021, Samangki Village, Simbang sub-district, Maros Regency average rainfall is 54 mm each month with 114 rainy days in 2021. The highest rainfall is in December of 900 mm, with a Rain duration is 12 days.

d. Landslide Vulnerability Map

Based on the overlay of the four landslide parameters, a map of the landslide hazard level is obtained using the fuzzy logic method with 4 class classification levels of vulnerability: not prone, low prone, moderate, and high prone. Based on the map of the level of vulnerability to landslides, it can be seen that there is one village that occupies the most significant area with a high vulnerability to landslides, namely Samangki Village, which is the location of this research. Based on the results of the analysis, this is influenced by the six parameters that cause landslides, such as the slope of the slope in the area is very steep, namely > 45%, plus the altitude at ± 1000 meters above sea level, the type of soil in the research location that allows water to pass easily, or easily Landslides occur and the types of rock found at the study site are also very sensitive to erosion (easily landslides).

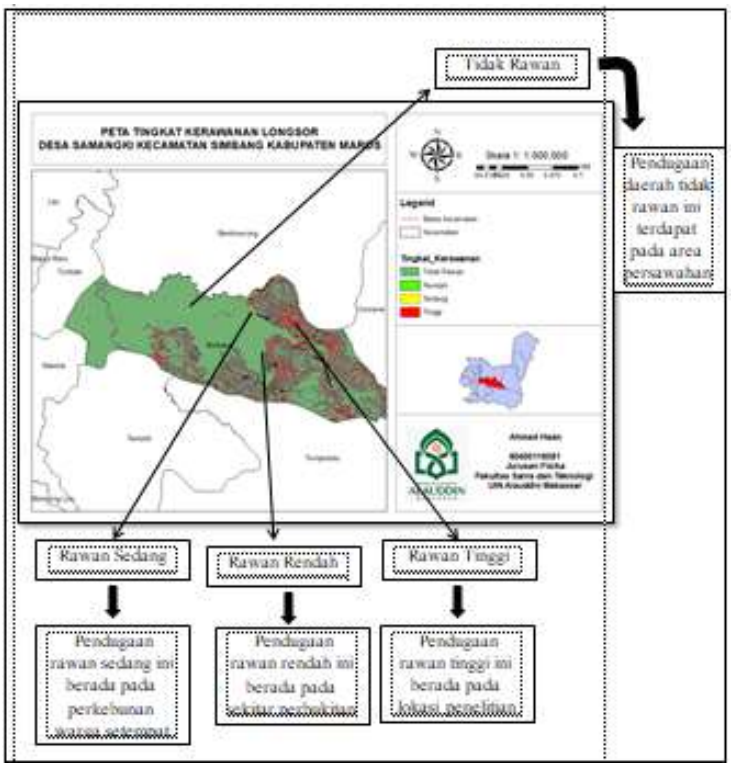

Figure. 19 Map of the landslide vulnerability level of Samangki District

The level of vulnerability of landslides in Simbang sub-district is divided into four classes: non-prone, low, moderate, and high. The classification above shows that the research location area is at a high level of vulnerability marked with red color.

This is due to the nature of the rock/soil, which needs to be well consolidated, high erodibility, and high porosity and permeability followed by high intensity of rainfall at that location with a rainfall rate of 2000-25000 mm/year. According to the Regulation of the Minister of Public Works concerning Guideline 56 on the Utilization of Spatial Areas prone to landslides (2007), high rainfall is rainfall with an annual rainfall intensity of more than 2,500 mm. So areas with rainfall distribution of more than 2,500 mm/year need to be watched out for because the area is prone to landslides and also depends on other physical conditions, as well as land use that is not suitable in the area, such as increased loads that exceed the soil's carrying capacity or shear strength land. This excessive load can be in the form of building loads or trees that are too thick and densely planted on slopes steeper than 40 degrees, and land clearing by residents for plantations and settlements is increasingly being carried out. Judging from the contoured topographical conditions, the community cleared the land not according to its function.

CONCLUSIONS

Based on resistivity, geological and climatological data processing that has been carried out in Samangki Village, Simbang District, Maros Regency, it can be concluded as follows:

1. Based on the results of the interpretation of the resistivity data for lines 1, 2, and 3, the resistivity values are from 500 Ωm to 1050 Ωm which are suspected of containing inset limestone and sandstone. These rocks are included in tonnage formation rocks. Plus, the slope is at a slope of > 25%, and Rainfall according to the BMKG Maros Regency

in 2017-2021, average Rainfall is 54 mm with 114 days in 2021, so this location has excellent potential for ground movement or landslides.

2. Based on the landslide-prone map in Samangki Village, Simbang District, Maros Regency, it is divided into four landslide-prone classes, namely, not prone to 86%, moderate to 2%. Prone by 3% and very vulnerable by 9%, and of the four landslide-prone classes above, the research location is at a very vulnerable point with a percentage of 9%, as shown in map 5.9 above.

REFERENCES

1] Alfian, Nawir, Dkk. 2018, *Analisis Akuifer Air Tanah Kota Makassar,* Makassar: Fakultas Teknologi Industri UMI.

[2] Andhini, Putri, Aulifa. 2018. *Analisis Resiko Dalam Upaya Penangulangan Bencana Tanah Longsor Di Kabupaten Gowa*. Makassar: Jurusan Teknik Geofisika FMIPA UNHAS.

[3] BPS Kota Makassar. 2021. *Kota Makassar Dalam Angka 2021*. Makassar: Badan Pusat Statistik Kota Makassar.

[4] Hanif, Dkk. 2015. *Kerawanan Bencana Tanah Longsor Kabupaten Ponorogo*. Surakarta: Jurusan Teknik Sipil Universitas Sebelas Maret Surakarta.

[5] Irmayanti. 2020. *Aplikasih Sistem Informasi Geografi (SIG) Dan Metode Geolistrik Dalam Pembuatan Peta Rawan Longsor Di Kecamatan Alla Kabupaten Enrekang*. Makassar: Jurusan Fisika Fakultas Sains Dan Teknologi.

[6] Isnaini, Rizkyah. 2019. *Analisis Wilayah Tanah Longsor Di Wilayah Jawa Tengah*. Surabaya: Universitas Airlangga Surabaya.

[7] Kementerian ESDM. 2018. *Gerakan Tanah*. Bandung: Kementerian Energi Dan Sumber Daya Mineral Badan Geologi.

[8] Muttaqin, Mu'ammar. 2020. *Identifikasih Pengaruh Air Tanah Terhadap Tingkat Kerawanan Longsor Dengan Metode Geolistrik Konfigurasi Schlumberger*. Medan: Jurusan Teknik Sipil Universitas Sumatera Utara.

[9] Nusaiba, F. 2018. *Identifikasi Letak Dan Sebaran Akuifer Dengan Metode Geolistrik Resistivitas*. Malang: Jurusan Fisika Fakultas Sains Dan Teknologi UIN Maulana Malik Ibrahim Malang.

[10] Nurfalaq, Aryadi Dkk. 2018. *Identifikasih Aquifer Daerah Pallantikan Kabupaten Jeneponto Dengan Metode Geolistrik*. Jeneponto: Jurusan Fisika Universitas Cokroaminoto Palopo.

Available online at:
Al-Fiziya: Journal of Materials Science, Geophysics, Instrumentation and Theoretical Physics
Website: http://journal.uinjkt.ac.id/index.php/al-fiziya
Vol.5 No. II Tahun 2022, 134 – 146

Manufacture Of UAV Skywalker 1900 Flying Vehicles Made Of Composites

Ferry Setiaawan[1,†], Muhammad Fauzaan Firmansyah [1],Dionisius Irvin Eka Bakti[1], Dhimas Wicaksono[1], Ikbal Rizki Putra[1]

[1]Aerospace Engineering Study Program, Faculty of Aerospace Technology, Sekolah Tinggi Teknologi Kedirgantaraan Yogyakarta, Jl. Parangtritis No. KM. 4,5 Druwo, Bangunharjo, Sewon, Bantul Daerah Istimewa Yogyakarta 55187.
[†]ferry.setiawan@sttkd.ac.id

Submitted: September 2022; Revised: Oktober 2022; Approved: November 2022; Available Online: Desember 2022

Abstract. The purpose of this research is to make a flying vehicle with the SKYWALKER 1900 UAV model for mapping missions with fiber glass reinforced composite materials on the wings and carbon fiber on the fuselage and tail. With composite materials, it is hoped that the structure of the UAV SKYWALKER 1900 will be stronger than previous materials using styrofoam. The method for making flying vehicles in this study uses 3D printing, to print UAV parts such as wings, fuselag and tail. then molding for components is made, and the final stage is manufacturing parts with composites using glass fiber and carbon fiber reinforcement using the vacuum bagging method. the analysis of weight deviation on the fuselag has a value of 70% and the weight deviation on the wings is 52%, the size deviation on the fuselag and wings weight occurs due to the putty process during finishing. the results of the aerodynamic analysis on the fuselag using solid work software, the UAV flight limit is 20 m/s to get the best flight results when flying

Keywords: Fiber glass, Fiber carbon, Composite, Vacuum Bagging, UAV Fixed wing

DOI : *10.15408/fiziya.v5i2.30531*

INTRODUCTION

"Unmanned aircraft have enormous benefits for the countries that have them, especially to support social and military activities. The positive functions of using drones in social activities include, among others, as a means of logistics transportation in remote areas that are difficult to access, mapping pipelines, agricultural uses, firefighting and searching for missing persons. Even now the United States has certified the Northrop Grumman Global Hawk unmanned aircraft to be used as a means of cross-country civil transportation. Unmanned aircraft in carrying out military duties has a very good advantage over other military aircraft technology, namely as a reconnaissance tool. [1]

Composite materials that have been widely used in the industrial world, especially in the aerospace industry. One example of the dominant use of composite materials in aviation can be seen in the structure of the Boeing 787 aircraft which uses composites as much as 50% of the total weight and 80% of composites based on the total volume. This

Copyright©2019, Published by **Al-Fiziya: Journal of Materials Science, Geophysics, Instrumentation and Theoretical Physics**
P-ISSN: 2621-0215, E-ISSN: 2621-489X

is due to the advantages of composite materials which are lighter, stronger and resistant to corrosion.[2]

Wing development for a vehicle is a multi-stage task that includes: wing profile selection, geometric calculations, structural design, material maintenance, numerical analysis and production. One of the main challenges in aviation is how to develop lightweight yet strong structures to withstand the applied loads. This problem can be fatal for pilots. There is a need for materials that can accommodate this.[3]

Vacuum Bag is a method of making composite specimens by pressing using an airtight bag to press a laminate of gelcoat, fiber and other layers on a mold until the layers are fused as a structural composite material. Vacuum Bags use atmospheric pressure as a clamp to press the laminate layers together with equal pressure. The laminate is sealed in an airtight bag.

After the uav has been made, a simulation will be carried out on the wing and body parts to determine the stress and aerodynamics of the uav using the solidworks application. After that, measurements of the dimensions and weight of the UAV were also carried out to find out the differences between the design results and the final results of manufacture, then an analysis of why there was a difference between the design and the final results.

In the references:
[1] (Finda Luthfiany Ustidivanissa*, 2017)
[2] (Alemour et al., 2019)
[3] (Fasel et al., 2020)

LITERATUR REVIEW

1. Drone/UAV

Drones are aircraft without a pilot. The aircraft is controlled automatically through a computer program designed, or via remote control from a pilot on the ground or in another vehicle. Initially, UAVs were remote-controlled aircraft, but now automated systems are being widely applied. Technological developments have also made drones to be widely applied for civilian needs, especially in the fields of business, industry and logistics.[4]

2. Airfoil

a geometric shape which when placed in a fluid flow will produce a lift (lift) more than the drag force. The air flow that passes through the airfoil can cause a vortex (vortex) at each end, the vortex can cause drag or drag that makes the lift or lift force decrease. There are two types of airfoils, namely symmetrical and asymmetrical airfoils, symmetrical airfoils are types where the top and bottom of the airfoil are the same shape, while asymmetric airfoils have different shapes at the top and bottom. [5]

3. Composite

Composites are usually composed of two basic materials, namely fiber and matrix. Fibers are usually flexible, have good tensile strength, but cannot be used at high temperatures while the matrix is usually ductile, soft, elastic and binding when it reaches the point of arrangement.[6]

4. Finite element method

Finite element method is increasingly used in the analysis of aircraft structures, including Unmanned Aerial Vehicles (UAVs). The structural model used for finite element analysis however needs to be validated in order to ensure that it correctly represents the physical behaviour of the actual structure. In this work, a case study of a straight, unswept and untapered wing structure made of composite material subjected to aerodynamic loading was modelled and analysed using finite element method.[7]

5. Vacuum Bagging

Atmospheric pressure compresses all sides of the mold at the same time, even above the surface of the mold. The pressure difference between the inside and outside of the mold determines the force that occurs when pressing the laminate inside the mold. Theoretically, the maximum pressure on the laminate when the vacuum works perfectly and can remove air in the mold on all sides of the mold is 14.7 Psi. So that the pressure difference that occurs in the mold is 6-12.5 Psi.[8]

6. 3D Printing

Numerous options exist for the mass production of lattice structures but they become limited for the production of one-offs or small quantities. The problem becomes even more acute for complex designs with undercuts and overhanging features since very few conventional manufacturing techniques can produce them. For testing purposes, multiple variants may be required for different geometric parameters of the design truss diameter, size of unit cell, density of structure which mean more tooling are needed. AM offers a less expensive and more flexible design and manufacturing option as the layer-by-layer approach allows arbitrary shapes, including lattice structures, to be easily produced directly from computer-aided design (CAD) files.20 Also, the per-unit cost of an AM part is the same regardless whether the machine makes one part or hundreds of parts.[9]

7. Lycal Resin

Lycal resin 1011 which includes Epoxy resin Lycal resin is a type of polyester resin and is made specifically for handicrafts and for its very clear and transparent coating. This lycal resin is also very strong against the sun, the nature of this lycal resin is that it has thicker properties and its use uses a ratio of resin: hardener with a ratio.[10]

8. Manufacturing UAV

Unmanned aircraft design process using Autodesk Inventor Professional 2016 software. The results of this unmanned aircraft design Unmanned aircraft dimension data obtained, as well as flight test data for the unmanned aircraft.[11]

In the references

[4] Arifin, 2021
[5] Muhamad Royan AL Faris, 2019
[6] Susanti, 1981
[7] Kanesan et al., 2014
[8] Rahadiyanto, 2018
[9] Moon et al., 2014
[10] Billy Suugondo et al., 2022
[11] Sirojuddin et al., 2019

Vol.5 No. II Tahun 2022, 134 - 146
P-ISSN: 2621-0215, E-ISSN: 2621-489X

RESEARCH METHODE

This research begins by determining the model of the flying vehicle, namely the UAV Skywalker 1900. Then a technical drawing is carried out using solidwork software and the part printing process is carried out using 3D printing. after the 3D Printing results in the assembly, molding is done for each part of the UAV. The final stage is to manufacture wings, fuselag and tail using composite materials (glass fiber and carbon fiber) using the vacuum bagging method. The work on this research can be seen in the flowchart below Figure 1.

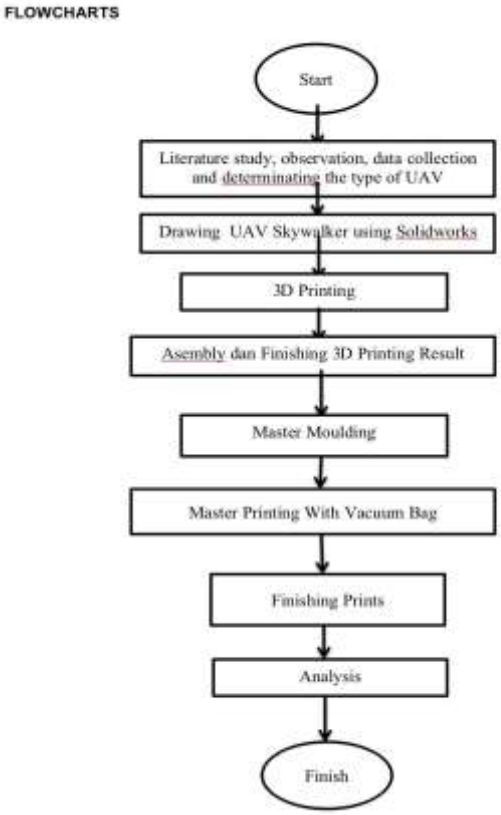

Figure 1. Flowchatrs

DESIGN MATERIALS AND TOOLS

1. Resin, Catalyst, Carbon Fiber
2. Pipe, Plastic bag, Waax, Glass, Spiral
3. 3D printing and Mouding
4. Propeller
5. Flight Control, Flight Main Board Software
6. Camera 5000 MP
7. Dynamo motor, power distribution cable, battery
8. Materials for Drone Frames (Carbon fiber and Fiber glass)
9. Acrylic scales

Vol.5 No. II Tahun 2022, 134 - 146
P-ISSN: 2621-0215, E-ISSN: 2621-489X

RESULTS AND DISCOUSINS

The results of the manufacture of the wing structure of the vehicle in this study are in the form of specifications for some of the parts used, the design of making the wing structure of the vehicle using the solidworks application. In the picture below, you can see the making of the wing structure of the vehicle which was designed using solidworks. UAV Skywalker engineering drawings can be seen in Figures 2 and 3

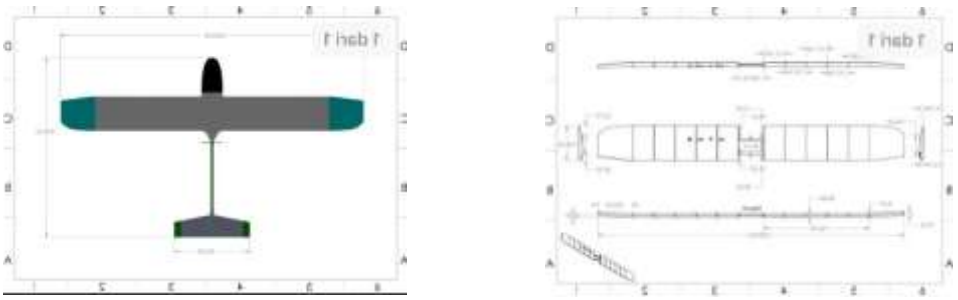

(a) (b)

Figure. 2 (a) Top view design (b) Long wing design

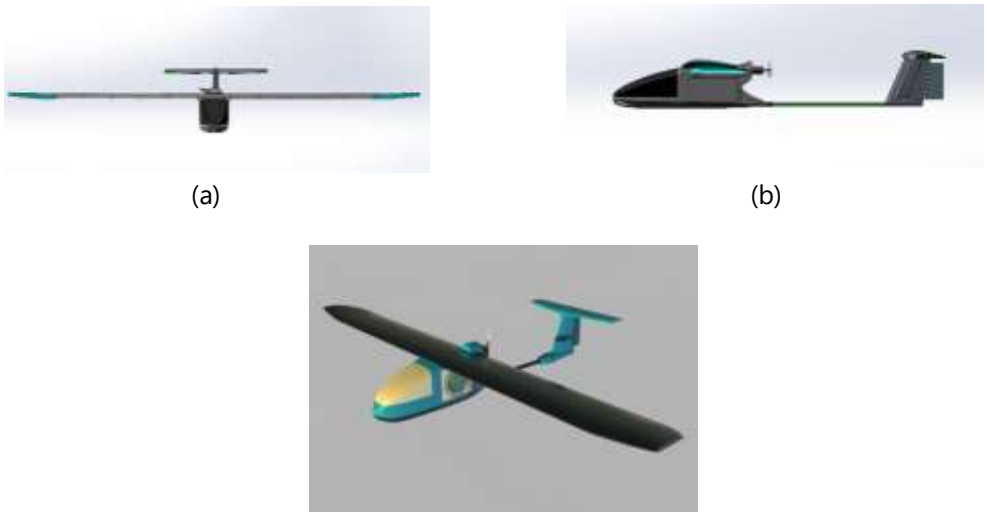

(a) (b)

(c)

Figure. 3 (a) Front view design (b) Side view design (c) Visual 3D Design

The design uses solidworks in the picture above, designed as needed to make wings. At this stage complex digital designs are converted into detailed physical models, this aims to simplify the manufacture of wings.

Vol.5 No. II Tahun 2022, 134 - 146
P-ISSN: 2621-0215, E-ISSN: 2621-489X

1. Manufacturing Process of Wings SkyWalker 1900

a. Master Wing 3D Printing to make prints, besides using 3D Printing on Wings, Styrofoam is also used. The selected styrofoam is then cut with a manual styrofoam cutter according to the design on the solidwork and added with epoxy so that the results that have been obtained become strong after that it is sanded to refine the part. In the Wing tip section using 3D Printing. The process of making wing parts can be seen in Figure 4.

(a) (b)

Figure 4. (a) Process of refining parts (b) Process of refining wing tip

b. Master molding is made after the phase where the Styrofoam has been cut using a cutter according to the shape designed using solidwork and the selected rip-like airfoil shape. The Mamo (Master Molding) process is added using PA Resin and Matt. The results of making molding can be seen in Figure 5.

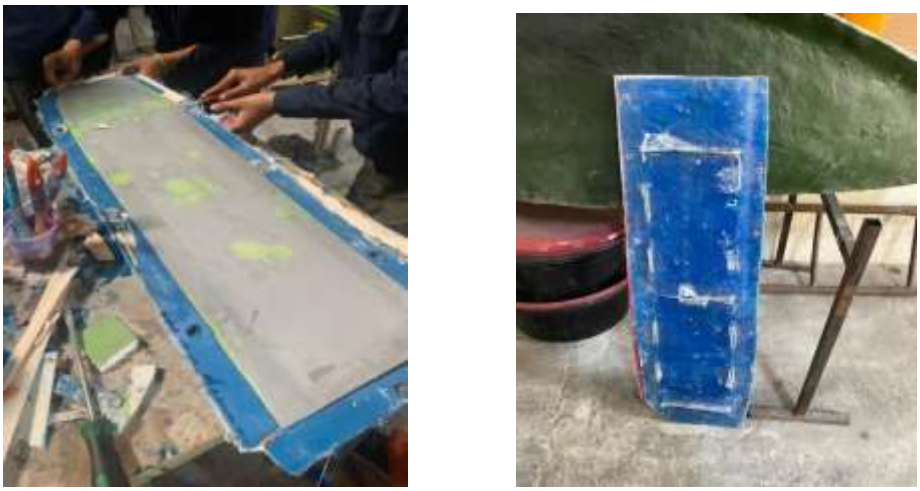

(a) (b)

Figure 5. (a) Master molding process (b) Moulding result

c. After the Master Molding is complete then putty and sandpaper using coarse and fine sandpaper to remove the pores and adjust the size according to the design on the solidwork and added with epoxy filler to coat the surface and cover the pores of the putty then clear (paint protector). The results of finishing parts for master molding can be seen in Figure 6.

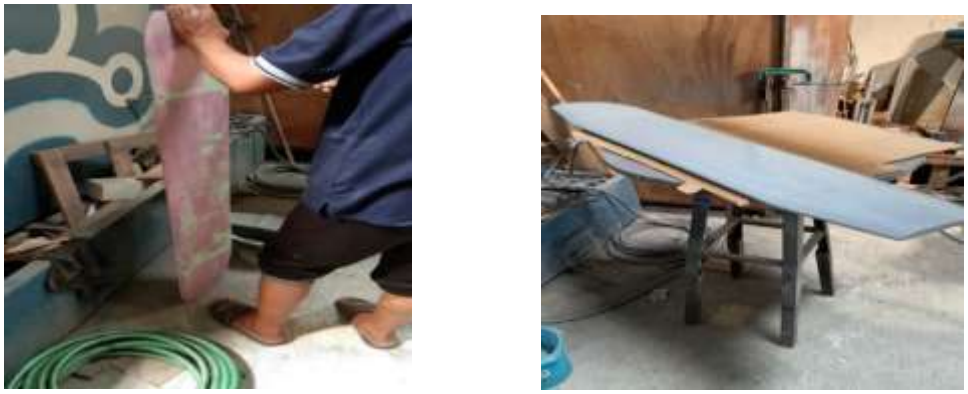

(a) (b)

Figure 6. (a)Pendentation Process (b) Finishing Part Result

d. In the process of making Wings mold using resin, matt and powder. The master that has been putty and cleared is used as a benchmark to form the printout. Then given a miracle gloss to the entire surface of the master evenly. master molding mold for the vacuum bagging process can be seen in figure 7.

(a) (b)

Figure 7. (a) Molding making process (b) Result

e. After the mold is finished, the mold is given a compound to make it smooth and then given a kit so that the mold is smoother and given a miracle gloss so that during the process of printing the wings resin does not stick. In this process, glass fiber, resin and satin cloth are added with plastic so that they can carry out the vacuum process. The wing printing process with vacuum bagging can be seen in Figure 8.

(a) (b)

Figure 8. (a) Procces Vacuum (b) vacuum bagging print results

f. In the finishing stage, after the wings are printed, the wings are sandpaper to reduce the weight on the wings themselves and also washed to make them clear and in this process the wings are combined into one and several rips are added inside. the results of the wing after assembly can be seen in Figure 9.

Figure 9. wing after assembly

2. Manufacturing Process of Fuselag and Tail SkyWalker 1900

a. At the time of conducting literature studies, observations, and data collection, it was decided that the flying vehicle to be made was the Skywalker 1900 UAV which is of the fixed wing type. composite materials are used, as well as carbon fiber as the main material.
b. The design using Solidworks will also be adjusted to the needs for which the design is made. At this stage the complex digital design is converted into a detailed physical model, this aims to make it easier to make the body of the drone flying vehicle physically.
c. At first the Design Results in Solidworks were then transferred to an application called QURA because this application can simplify the printing process on 3D Printing tools. The 3D printing process can be seen in Figure 10.

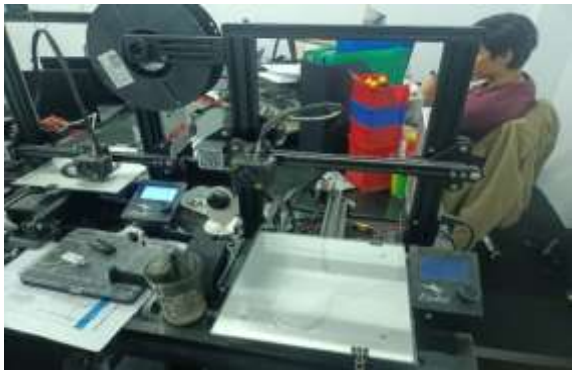

Figure 10. 3D Printing Process

d. After the 3D print is complete, it will be followed by a coarse and fine sanding process on the 3D print part until the outer surface of the part is not sharp and porous. The 3D printing assembly process for making molding can be seen in Figure 11.

Vol.5 No. II Tahun 2022, 134 - 146
P-ISSN: 2621-0215, E-ISSN: 2621-489X

Figure 11. Assembly Result and Sandpaper process

e. The next process is the manufacture of molding, the 3D printed body will be carried out with an epoxy filter process to coat the surface and cover the caulking pores and then clear (paint protector). After that, the 3D printed body will be made by master molding by coating all parts using resin. PA and Matt. The manufacture of fuselag molding can be seen in Figure 12.

Figure 12. Moulding Process

f. In this process the mold that has been given a miracle gloss will be coated with carbon fiber which is cut to the size of the mold and sprinkled with carbon powder on all sides and then sprayed with scotch spray which functions as an adhesive between the carbon fiber and the mold, then added another piece of carbon fiber for the second layer. .At the top of the carbon fiber coated with peelply and coated again with PVC Plastic Mesh, in the last layer the entire surface of the mold is covered with plastic and on the sides is added Rubber Butly Tape in order to prevent air from entering during the vacuum process. the process of printing fuselag and tail can be seen in Figure 13.

Figure 13. Step of Vacuum Process

g. At the finishing stage, the wings are sanded again and cleaned if any vacuum-generated material is carried away or sticky. Then the right and left sides of the body will be combined into one, followed by the checking process and ready to proceed for the next process, namely adding a motor and installing avionics. system , also combines with wings and tail. the results of the fuselage assembly from the vacuum bagging prints can be seen in figure 14.

Figure 14. The Result of Vacuum Bag After Assembly

3. Assembly Part and Manufacture UAV

After all the parts have been made using fiber glass for the wings and carbon fiber on the fuselage and tail then assembled and vacuumed using vacuum bagging. The results of the Skywalker 1900 UAV manufacture can be seen in Figure 15.

Figure 15. UAV Skywalker Flight Test

4. Wing and Body Result Analysis and Simulation

a. Dimensional comparison analysis between design results and product results on wings and fuselags can be seen in Tables 1 and 2 below.

Table 1. Wing Comparison of Design Drawings and Product Dimension Value

Parameter Result	Design Dimension Value	Product Dimension Value	Wings Size Deflation and Simulation
fiber thickness (mm)	0.68	0.68	0
weight of wings (gram)	378.94	576	52%
Long wings (mm)	2200	2254	2,45%
wings width (mm)	248	250	0.80%
wings height	37	30	-18%

Table 2. Body Comparison of Design Drawings and Product Dimension Value

Parameter Result	Design Dimension Value	Product Dimension Value	Wings Size Deflation and Simulation
fiber thickness (mm)	1	1.23	23%
weight of body (gram)	450	765	70%
Long body (mm)	550	590	7.2%
body width(mm)	102	120	17.8%
body height (mm)	207.69	210	0.98%

The difference between the results in the design and the value of the product dimensions are as follows: Weight, Length,Width andHeight have different values because the design and product results have different materials due to consideration of the strength of the material when the flying vehicle operates. and the last one is in the process of making this flying vehicle which has not fully used the engine, so that in the manufacturing process there are several parts or parts that must be sanded and putty to cover the pores on the part or part which can later make the final product of the flying vehicle less maximum.

a. Simulation aerodynamics of body

a. This simulation was carried out 3 times with different speeds, namely 5 m/s, 20 m/s, and 40 m/s in order to see the difference in pressure on the body of the Skywalker UAV, so that it can be determined at what speed the Skywalker UAV can function efficiently. And can fly optimally. aerodynamic simulation can be seen in figure 17

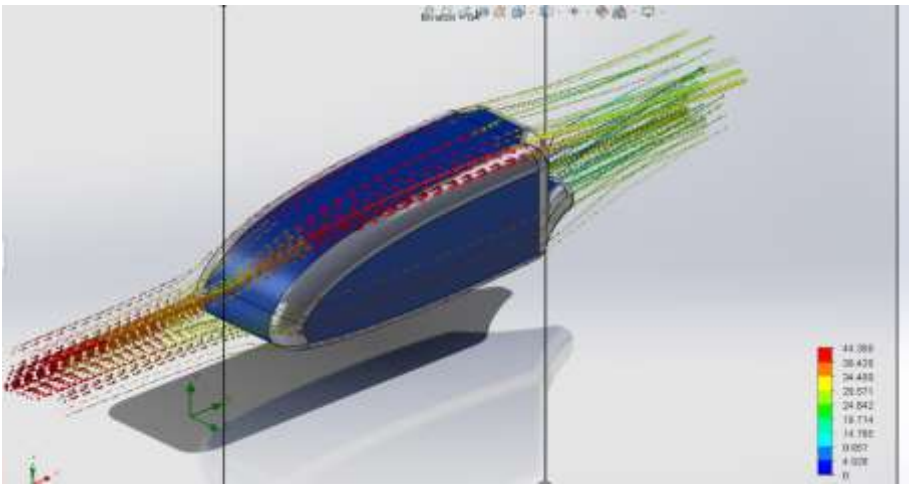

Figure 17. (a) analysys aerodynamics

CONCLUSIONS

The research that has been carried out on the manufacture of the wing structure of the following rides to determine the results of the image design of the wings and to determine the design results with the best product results using solid work software can be concluded as follows:

1. The result a deviation with weight and size in the design compered to the product result on the wings and body of the first UAV in terms of weight, this is due to the process of making this UAV sendpaper, putty in several parts, and coating resin on all parts of the body.This causes an increase in the weight of the Sywalker UAV, causing a difference in weight to the design. Then the difference in dimension is caused by several factors, namely the thickening that occurs due to the process described above, then there is a revision to the material, for example wings, which initially used composites replaced with fiber glass, the last is the addition of length in several parts so that this UAV can fly efficiently.
2. From the results of the simulation of the aerodynamics body from the results of the design and product using solid work software, flying limits UAV is 20 m/s to get best flying result.

REFERENCES .

[1] R. N. A. P. Finda Luthfiany Ustidivanissa*, "Tinjauan Yuridis Pengoperasian Pesawat Tanpa Awak Terhadap Keselamatan Penerbangan Di Wilayah Negara Kesatuan Republik Indonesia (Studi Pada Pt. Uavindo Nusantara, Bandung)," *Diponegoro Law J.*, vol. 6, no. 2, pp. 1–14, 2017, [Online]. Available: https://ejournal3.undip.ac.id/index.php/dlr/article/view/17365.

[2] B. Alemour, O. Badran, and M. R. Hassan, "A review of using conductive composite materials in solving lightening strike and ice accumulation problems in aviation," *J. Aerosp. Technol. Manag.*, vol. 11, pp. 1–23, 2019, doi: 10.5028/jatm.v11.1022.

[3] U. Fasel, D. Keidel, L. Baumann, G. Cavolina, M. Eichenhofer, and P. Ermanni, "Composite additive manufacturing of morphing aerospace structures," *Manuf. Lett.*, vol. 23, pp. 85–88, 2020, doi: 10.1016/j.mfglet.2019.12.004.

[4] M. H. R. Arifin, "Institut teknologi nasional, PENGERTIAN DRONE," pp. 4–11, 2021.

[5] Muhamad Royan AL Faris, "Visualisasi Pengaruh Sudut dan Kecepatan Aliran Udara Terhadap Stall Airfoil NACA 2415 dan NACA 4424," vol. 16, pp. 56–62, 2019.

[6] Susanti, "Materi Komposit," *J. Chem. Inf. Model.*, vol. 53, no. 9, pp. 1689–1699, 1981.

[7] G. Kanesan, S. Mansor, and A. Abdul-Latif, "Validation of UAV wing structural model for finite element analysis," *J. Teknol.*, vol. 71, no. 2, pp. 1–5, 2014, doi: 10.11113/jt.v71.3710.

[8] A. Rahadiyanto, "Perbaikan Proses Pembuatan Produk Komposit Dengan Metode Vacuum Bagging," *Tugas Akhir, Univ. Islam Indones. Yogyakarta*, p. 9, 2018.

[9] S. K. Moon, Y. E. Tan, J. Hwang, and Y. J. Yoon, "Application of 3D printing technology for designing light-weight unmanned aerial vehicle wing structures," *Int. J. Precis. Eng. Manuf. - Green Technol.*, vol. 1, no. 3, pp. 223–228, 2014, doi: 10.1007/s40684-014-0028-x.

[10] S. Billy Suugondo, A. Purna Irawan, and E. Siahaan, "Analisis Kekuatan Komposit Berpenguat Serat Karbon Dengan Matriks Resin Lycal 1011 Terhadap Sifat Mekanis," *J. Heal. Sains*, vol. 3, no. 7, pp. 905–913, 2022, doi: 10.46799/jsa.v3i7.452.
[11] M. R. Sirojuddin, S. B. Wibowo, and G. Nugroho, "Perancangan dan Pengujian Terbang Pesawat Tanpa Awak Lokeswara," *Semin. Nas. Inov. dan Apl. Teknol. di Ind.*, pp. 334–338, 2019.

Available online at:
Al-Fiziya: Journal of Materials Science, Geophysics, Instrumentation and Theoretical Physics
Website: http://journal.uinjkt.ac.id/index.php/al-fiziya
Vol.5 No. II Tahun 2022, 147 - 156

The Analysis Of Micromechanic On Creating Of Gypsum Board Strengthened By Bintaro Fruit Fiber (Cerbera Manghas) With 3d Orientation

Tri Adelia [1,] , Delovita Ginting [1†], Romi Fadli Syahputra [1]

[1]Physics Study Program, Faculty of Mathematics, Natural Science, and Health , University of Muhammadiyah Riau, Tuanku Tambusai Street, Pekanbaru City, Pekanbaru 28291, Indonesia

† delovita@umri.ac.id

Submitted: September 2022; Revised: Oktober 2022; Approved: November 2022; Available Online: Desember 2022

Abstract. This research succeeded in modifying the manufacture of gypsum board with the addition of natural fiber, namely bintaro fruit with the 3D orientation arrangement method. The raw materials for this research are gypsum flour and Bintaro fruit fiber as a matrix and filler. Bintaro fruit fiber previously carried out an alkalization process where the fiber was soaked in a solution of NaOH and distilled water for 24 hours. The manufacture of composites using the ratio of the matrix mass fraction and the filler mass fraction is as follows 100: 0, 99: 1, 98: 2 and 97: 3. The characterizations carried out include density test, moisture content test, flexural strength test and micromechanical analysis. Gypsum board composite based on micromechanical calculations resulted in the highest density value in the control sample, in the best density value was at the filler fraction of 3%, the best moisture content value in the control sample, the flexural strength test value the best of the control sample, but the filler fraction is 3% of the sample with the best fracture resistance. 3D orientation in theory and practice has fulfilled the principle that it is able to increase the physical and mechanical value of gypsum board.

Keywords: *Gypsum, Bintaro fruit, 3D orientation, composite, micromechanical analysis*

DOI : *10.15408/fiziya.v5i2.29783*

INTRODUCTION

Increasing global concern for environmental sustainability has emerged the greater opportunities for the use of natural fibers as reinforcement or bio-fillers in the manufacture of composites. There are many advantages of using natural fibers to make composite materials such as being made from renewable sources, low price, high specific strength, good bond between fiber and matrix, environmental friendliness, so that it results the superior mechanical-thermal-physical properties of composites. Natural fibers

containing lignocellulosic are a good alternative source to replace synthetic fibers in the manufacture of composite materials [1]. One of the natural fibers that has the potential as a biofiller material in the manufacture of gypsum board is bintaro fruit (Cerbera manghas) which has a high content of cellulose, lignin and fiber. On the other hand, bintaro fruit also contains cerberin, especially in the part of the fruit which belongs to the class of saponins, alkaloids, flavonoids and tannins which are toxic and which are used as termite repellents [2].

Gypsum is one of the earliest types of building materials and the history of its application can be traced back 4000 years [3]. Gypsum has a variety of extraordinary advantages, one of which is easy fabrication, low price and energy consumption as well as good aesthetic appearance, good recycling, good fire resistance, good thermal and sound insulation properties, in residential buildings currently gypsum is one of the most important construction materials used. Its application is often preferred over other building materials (plywood, wood etc.) [4]. Gypsum does not have good mechanical properties. This is a limiting factor in the use of gypsum board so that it is necessary to increase the mechanical strength of gypsum. Gypsum has several weaknesses, such as being more brittle, less strong, and less water resistant when it is compared to wood [5].

The occurrence of failure and damage to composites is generally related to the location of the fibers and their binders in the material [6]. The 3D orientation of the composite results in higher damage tolerance and resistance to delamination [7], as well as sealing of damage between the matrix and filler in the composite [8]. Making gypsum board by adding natural fibers with a 3D orientation where the fibers will be arranged from 3 different directions will affect the increase in compressive strength, tensile resistance, and elastic modulus of gypsum board [1]. According to Muntangkaw (2021) the best fiber orientation efficiency (K) parameter is 3D with a value of K = 1/5 when compared to 1D K = 1 and 2D K = 3/8.

This study aims to examine the mechanical and physical properties of bintaro fiber reinforced gypsum composites. The 3D orientation method is used to arrange bintaro fibers in a gypsum matrix as described by Muntongkaw (2021). The mass fraction of bintaro filler to gypsum will be varied to determine the mass fraction that gives the best mechanical properties. The reference for the mechanical and physical properties of gypsum composites in this study used SNI 03-6384-2000 regarding gypsum board.

RESEARCH METHOD

Research Tool and Material

The tools used in this study were knives, aluminum molds measuring 40 cm x 20 cm x 2.5 cm, glass as covering the molds 40 cm x 20 cm x 2 mm, mixing containers, spatulas, scissors, beakers, digital balances, calipers. shovel, screw micrometer, scroll saw model RSSS 125, electric oven and sacks. The materials used in this study were bintaro fruit (Cerbera Manghas), gypsum flour, sodium hydroxide (NaOH), distilled water and water.

Preparation of Bintaro fiber

Bintaro fruit is separated between the fiber and the seeds, the fiber that has been separated is then dried in the sun for 5 days. The dried fibers were cut into lengths of 6 cm. The fibers were alkalized with NaOH solution and distilled water while the concentration of the solution was 5% by weight of the distilled water for 2 hours to

remove the lignin content in the Bintaro fruit fiber [9]. The fiber that has been alkalized is then dried in the sun for 8 hours.

The Production of Gypsum Board

Gypsum board was created through a mixture of gypsum flour and bintaro fruit fiber with a ratio of matrix mass fraction and filler mass fraction of 100 : 0, 99 : 1, 98 : 2 and 97 : 3 for a clearer comparison of the gypsum board composition levels can be seen in Table 1. Mixture Gypsum flour is the matrix for making this gypsum board and Bintaro fruit fiber is a filler in this study. The gypsum mixture is made from gypsum flour and water in a ratio of 3: 1 which is stirred using a spatula until it is homogeneous. Preparation of control gypsum samples was made by mixing gypsum flour and water with the comparison in Table 1 which was stirred using a spatula until homogeneous and then poured into a mold and the sample was covered with glass so that the surface of the sample was smooth and flat. This process can be seen more clearly in Figure 1. Preparation gypsum sample 1, gypsum sample 2, gypsum sample 3, made with a mixture of gypsum flour and bintaro fruit fiber. The gypsum mixture is divided into two parts, namely the first coating and the second coating. The first layer is put into the mold first, then the fibers that have been mass calculated and arranged in 3D orientation are put into the mold, then coated with the second layer and then covered with glass so that the sample surface is smooth and flat. The sample was allowed to stand for 5 hours and then removed from the mould. To make this process clearer, it can be seen in Figure 2. Furthermore, the samples were allowed to stand at room temperature for 28 days before cutting the samples.

Table 1. Comparison of gypsum board composition

Sample Code	Extract of bintaro fruit (%) + gypsum flour (%)	Mass of bintaro fruit extract (gram)	Mass of gypsum flour + water (3:1)		Composite of total gipsum (gram)
Control*	0 : 100	0	1575	525	2100
Sampll 1†	1 : 99	21 : 3	1559	520	2100
Sampll 2	2 : 98	42 : 3	1544	515	2100
Sampll 3	3 : 97	62 : 3	1527	509	2100

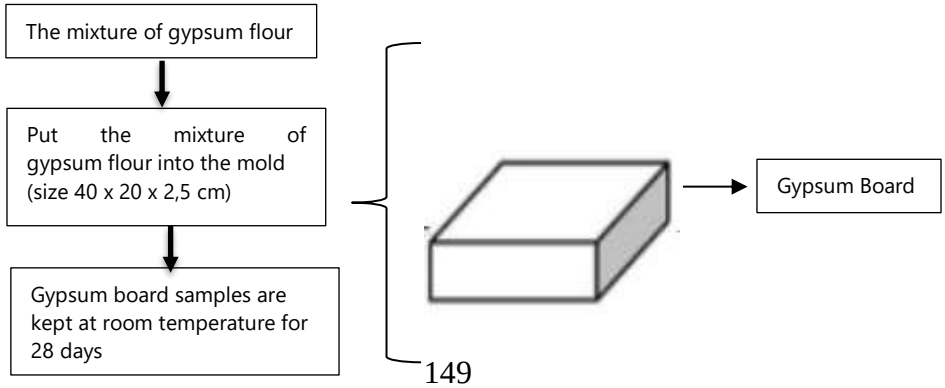

Figure 1. The Production of control gypsum board samples

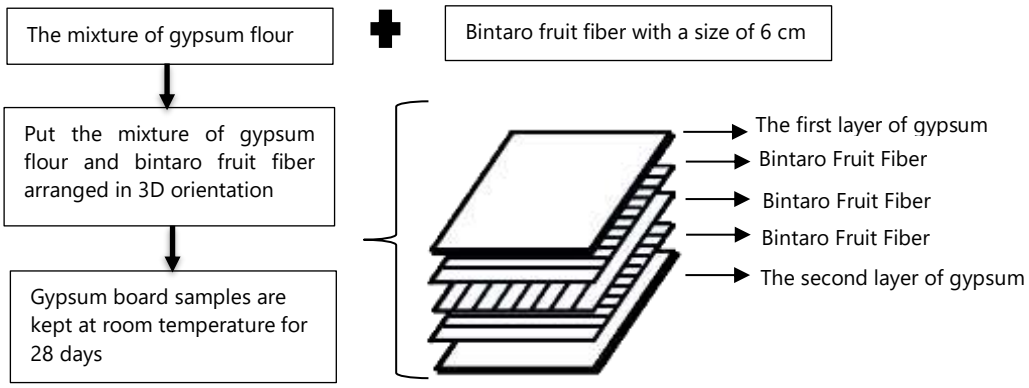

Figure 2. The Production of Gypsum Board with 3D orientation

Testing Process

Micromechanical Analysis

Micromechanical analysis shows that the relationship between the physical and mechanical properties possessed by the matrix and fibers and the composites which they form. Fiber and matrix are considered as separate elements that bind each other which is a separate composite property [10].

Filler Density and Matrix

Calculation of Filler Density and Matrix can be seen in Equation (1).

$$\rho_f = \frac{m_f}{v_f} \quad ; \quad \rho_m = \frac{m_m}{v_m} \tag{1}$$

Description: ρ_f = Mass of filler; m_f = Mass of filler; v_f = volume filler; ρ_m = Mass of matrix ; m_m= Mass of matrix ; v_m = Volume matrix

Mass fraction

The mass fraction of the composite consists of the mass fraction of the filler and the matrix. The calculation of the mass fraction can be seen in equation (2) [11].

$$M_f = m_f\, m_c \; ; M_m = m_m\, m_c \tag{2}$$

Description: M_f ==Mass fraction of filler ; m_f = Filler mass ; m_c = Composite mass ; M_m= Mass fraction matrix ; m_m = matrix mass ; m_c = Mass configuration

Fractional volume

Composite volume consists of filler volume ($\boldsymbol{v_f}$) and matrix volume ($\boldsymbol{v_m}$). The filler and matrix volume fractions are defined in equation (3).

$$V_f = v_f\, v_c; V_m = v_m v_c \tag{3}$$

Description: V_f = volume fraction of filler; v_f = Volume of filler; v_c = Composite volume; V_m = volume of fraction matrix; v_m= Volume matrix; v_c = Composite volume

The Relationship between mass fraction and volume fraction

Relationship between $m_c = \rho_c v_c$; $m_f = \rho_f v_f$; $m_m = \rho_m v_m$ s thus it can be concluded according to Equations (4) [12] and (5).

$$V_f = \frac{(\frac{m_f}{\rho_f})}{\left(\frac{m_f}{\rho_f}\right)+\frac{m_m}{\rho_m}} \quad (4)$$

$$V_m + V_f = 1 \quad (5)$$

Description: V_f= volume of filler fraction ; m_f = Mass of filler; ρ_f= Mass of filler; V_m = mass volume fraction ; V_m = Mass of volume fraction ; ; p_m= Mass of matrix

Composite Mass

Composite mass can be asserted in terms of mass fraction and volume fraction. In the form of volume fractions can be seen in Equation (6) [13] :

$$\rho_c = \rho_f V_f + \rho_m V_f \quad (6)$$

Description: ρ_c = Mass of the composite; ρ_f = Mass of filler; ρ_m = Mass of matrix ; V_f = volume of filler fraction

Gypsum Board Composite Testing

Composite tests to be carried out include density testing, moisture content testing and flexural strength testing.

Density Test

Density is a measure of the compactness of a particle in a volume. In this study, the density tested was filler, matrix and composite. This test is carried out to see the density: filler, matrix and composite. The size of the density test object made is (10 x 10) cm in accordance with SNI 03-6384-2000. Density calculation can be seen in Equation (7).

$$\rho = \frac{m}{V} \quad (7)$$

Information : ρ = Density of composite $\frac{g}{cm^3}$) ; m = Composite mass (g) ; V = (cm^3)

Water Content Test

The moisture content of the composite board is calculated based on the initial weight (Ba) and oven dry weight (Bk). Gypsum board moisture content is calculated based on SNI 03-6384-2000. Calculation of water content can be seen in Equation (8) :

$$\text{Water Level (\%)} = [(Ba-Bk)/Bk] \times 100\% \quad (8)$$

Note: Ba = initial weight of the test sample (g) ; Bk = oven dry weight of the test sample after drying (g)

Flexural Strength Test

Flexural strength test is the ability of a material to withstand bending forces in a direction perpendicular to the cross section until the test sample fractures. The flexural strength value of gypsum board is determined using Equation (9) based on ASTM C 473.

$$KLMN = \frac{S^3 \Delta B}{4lt^2 \Delta D} X\ 100 \quad (9)$$

Description: : $KLMN$ = Flexural toughness modulus of elasticity (kgf/cm2) ; S = length of stretch (cm) ; l = Width of fiberboard test sample (cm) ; t = Thickness of the fiberboard test sample serat (cm) ; ΔB = Difference in load (B1- B2) taken from the curve (kgf) ; ΔD = Deflection (cm) that occurs at the difference in load (B1 – B2)

FINDING AND DISCUSSION

The Calculation of Composite Density in accordance with Micromechanical Theory

The results of the micromechanical analysis of the gypsum board sample reinforced by Bintaro fiber with a 3D orientation can be seen more clearly in Figure 3 (a). The highest composite density micromechanical analysis value was found in the control sample without filler mass fraction, while in sample 2 with 1% filler mass fraction and sample 3 with 2% filler mass fraction decreased, sample 4 with 3% filler mass fraction the density value increased again .

Micromechanical analysis of composite density resulted from the calculation of matrix volume fraction, filler volume fraction, matrix density and filler density used in this study. In the control sample without the addition of filler mass fraction the resulting composite density value is 1.67 (g/cm3), the addition of 1% filler mass fraction the composite density value is 0.4 (g/cm3), the addition of 2% filler mass fraction the composite density value is 0.48 (g/cm^3) and the addition of a filler mass fraction of 3% composite density value is 1.53 (g/cm^3). The higher the filler volume of the composite, the greater the composite density value. The results of micromechanical analysis show that the addition of filler with a 3D orientation can increase the density of the composite, at 3% filler mass fraction the value of composite density increases by 2% and 2.1% when it is compared to 1% and 2% filler mass fractions. However, the volume of filler used was not large enough so that the density of the composite in the mass fraction of 1%, 2% and 3% was not higher than the density of the composite in the control sample.

The Test Result of Composite Density

The results of testing the density of the gypsum board samples reinforced by bintaro fiber with a 3D orientation for more details can be seen in Figure 3 (b). This value is the measurement value for each fraction which is carried out in triplicate (three times). The gypsum board density value decreased from the control sample to the sample with a filler mass fraction of 1%, 2% and increased in the sample with a filler mass fraction of 3%.

The results of the density of the gypsum board composite in the control sample obtained a value of 1.02 (g/cm^3), the addition of a 3% filler mass fraction the composite density was 1.20 (g/cm^3), the 2% filler mass fraction the composite density value was 0.96 (g/cm^3) and the filler mass fraction 1% composite density value of 1.00 (g/cm^3). The composite density values for the 3% filler mass fraction increased by 0.25%, 0.20% and 0.17% from the 1%, 2% filler mass fraction and control samples. The density value of the 3% filler mass fraction is much greater when compared to the 1%, 2% filler mass fraction

density value and the control sample, the composite height in the 3% filler mass fraction is smaller when compared to the 1%, 2% and 1% filler mass fraction. control sample. This is due to the 3% filler mass fraction of the composite matrix entering the filler cavity, so that the resulting volume is smaller.

Micromechanical Analysis

The comparison of the results of micromechanical theory and practice can be seen in Figure 3 (c). The results of micromechanical theory and direct practice tend to have in common, namely the highest density value with the control sample, samples with 1% and 2% filler mass fractions the density value tends to decrease and the 3% filler mass fraction of density value increases again.

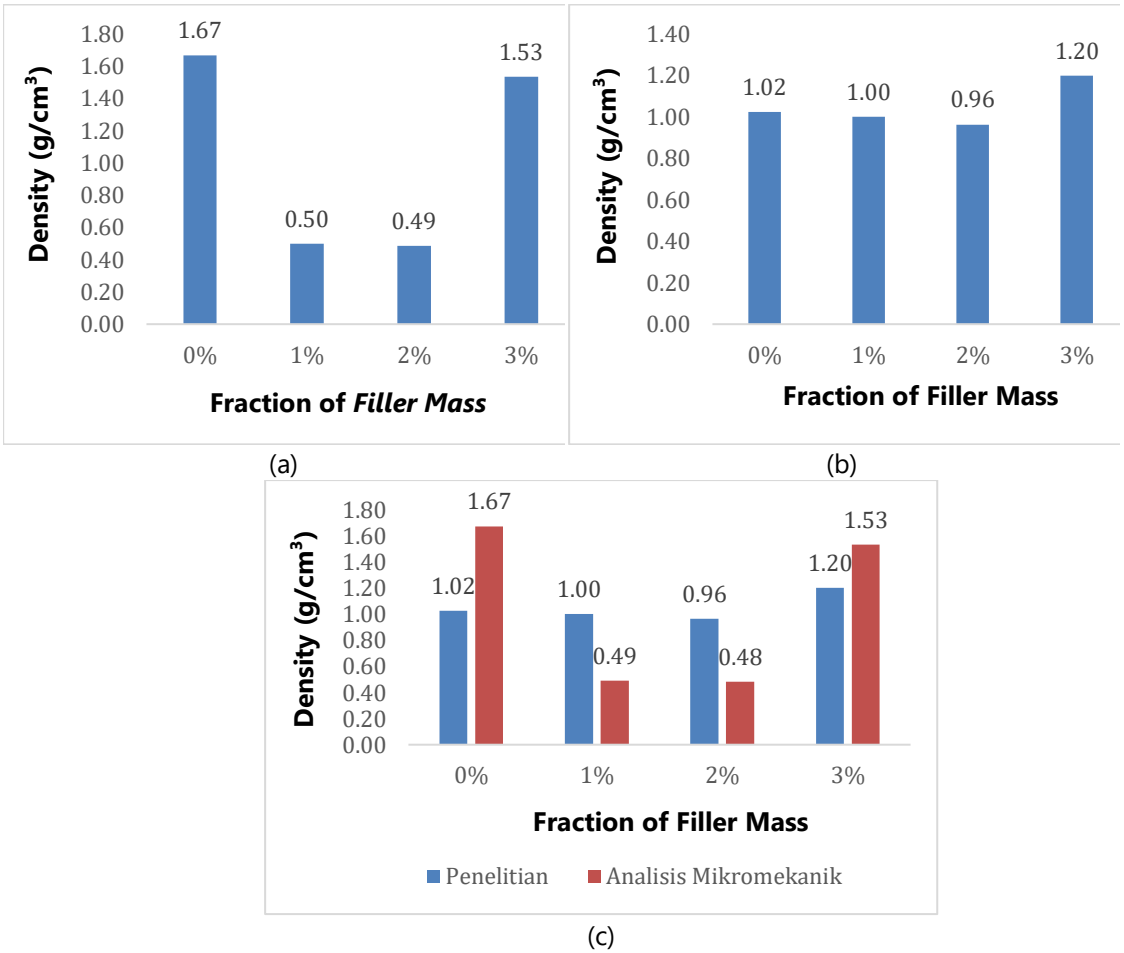

Figure 3. (a) Density Testing Results Based on Micromechanical Theory, (b) Practical Density Testing Results, and (c) Density Test Combined Results Based on Micromechanical Theory and Practice

The results of micromechanical theory and practice have the same trend, the highest density value is found in the control sample in micromechanical theory, while in direct practice the highest density value is in the 3% filler mass fraction, samples with 1% and 2% filler mass fractions experience a decrease in density values, samples with a filler mass fraction of 3% the density value increased again. Samples with a filler mass fraction of 1% and 2% in practice decreased, this was due to the presence of voids or cavities. Voids are a type of defects that appear in composite materials due to the loss of some elements during the fabrication process. The presence of voids can affect the mechanical

properties and increase the potential for composite damage [14]. The difference in results from micromechanical theory and practice is due to one of the factors that there are cavities that are not calculated in the micromechanical density calculation.

The Test Result of Water Content

Water content is the amount of water contained in a composite [15]. The water content is highly dependent on the surrounding air conditions. The results of testing the water content of the gypsum board sample reinforced by Bintaro fruit fiber with a 3D orientation for more clarity can be seen in Figure 4.

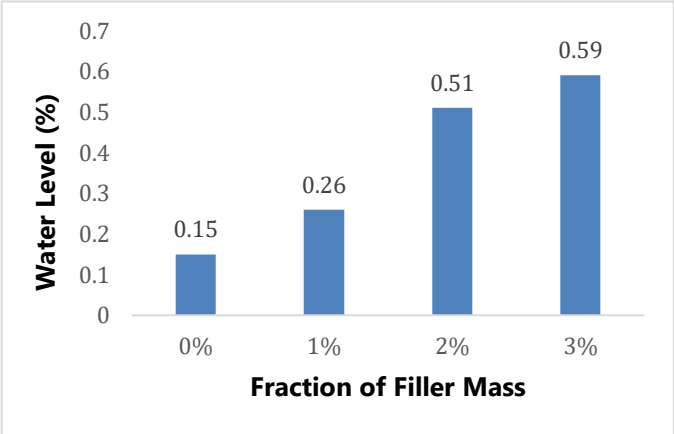

Figure 4. Gypsum Board Water Content Test Results

Dealing with Figure 4, it can be seen that the water content value of gypsum board has increased, the more bintaro fruit filler used, the higher the water content value. This is due to the higher ratio of bintaro fruit filler, besides that the higher gypsum matrix fraction can fill the space between the bintaro fruit fillers. In this study the lowest levels were in the control sample. The more matrix used, the lower the water content, this is because the bonds between the matrices will be tighter so that water will be difficult to enter between the matrices. The water content tends to be higher in the filler mass fraction of 1%, 2% and 3%. The use of more and more matrix can cause fewer cavities in the composite filled with water because these cavities have been filled with matrix that has frozen [16].

The Test Result of Flexural Strength

The flexural strength test of gypsum board was carried out using the UTM (Universal Testing Machine) tool. The principle of flexural strength testing is that the sample is given a force, when the sample breaks, the flexural strength value is recorded on the testing computer. The results of the flexural strength test of the gypsum board sample can be seen more clearly in Figure 5.

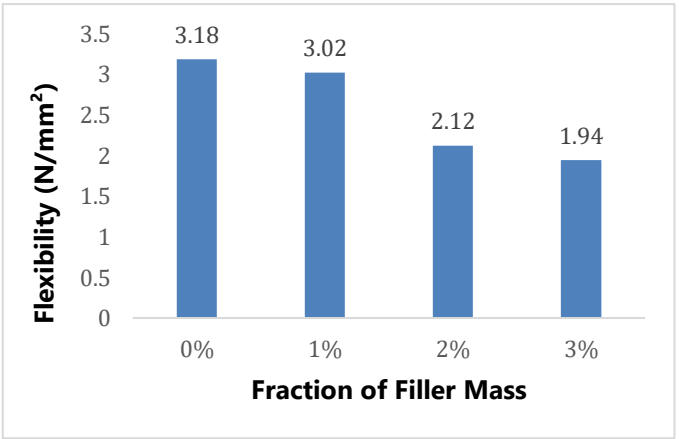

Figure 5. Results of the Flexural Strength Test of Gypsum Board

Regarding to Figure 5, it can be seen that the control sample with the highest flexural strength value while the gypsum sample with a filler mass fraction of 1%, 2% and 3% has decreased. decrease in flexural strength. This is due to the sample with a filler mass fraction of 1%, 2% and 3% using less matrix when compared to the control sample. Referring to Figure 2, the force exerted on the composite is the same, but the amount of matrix in the first layer is much less according to the mass fraction of the matrix used. In the test after the compressive force was transferred to the fiber in the 3% filler mass fraction, the fiber was able to survive stronger than the 1% and 2% filler fractions. It was concluded that the mass fraction of 3% filler, the fracture time from the first layer to the fiber was faster, but the fracture time to the second layer was longer, the mass fraction of the 1% and 2% filler was also the same. When the control sample is given a compressive force, will break completely due to there are no fibers binding the matrix.

CONCLUSION

The finding of micromechanical analysis research on the manufacture of gypsum boards reinforced by bintaro fiber with a 3D orientation, it can be concluded that:

1. In theory and practice, 3D orientation fulfilled the principle that 3D orientation could increase the physical and mechanical value of gypsum board.
2. In the micromechanical analysis, the density and flexural strength have increased in line with the increase in the filler fraction. However, in this study, the amount of filler fraction added was still insufficient due to the value of the filler fraction was a constant which affected the value based on the micromechanical analysis formula.

SUGGESTION

The results of micromechanical analysis research on the manufacture of gypsum board can be suggested as follows:

1. Dealing with the calculation, it indicates that the micromechanical value will increase if the used amount of filler fraction increases.
2. The 3D orientation arrangement must be updated, the fiber arrangement used can be alternated with gypsum flour.

REFERENCES

[1] S. Muntongkaw, S. Pianklang, dan N. Tangboriboon, "Modifications to improve properties of gypsum ceiling composites as multifunctional construction by embedding Typha angustifolia fiber and natural rubber latex compound," *Case Study. Constr. Mater.*, vol. 15, no. August, hal. e00658, 2021, doi: 10.1016/j.cscm.2021.e00658.

[2] G. Iman dan T. Handoko, "Pengolahan Buah Bintaro sebagai Sumber Bioetanol dan Karbon Aktif," *Pros. Semin. Nas. Tek. Kim. "Kejuangan,"* vol. 2005, hal. 1–5, 2011.

[3] L. Boccarusso, M. Durante, F. Iucolano, D. Mocerino, dan A. Langella, "Production of hemp-

gypsum composites with enhanced flexural and impact resistance," *Constr. Build. Mater.*, vol. 260, hal. 120476, 2020, doi: 10.1016/j.conbuildmat.2020.120476.

[4] A. Erbs, A. Nagalli, K. Querne de Carvalho, V. Mymrin, F. H. Passig, dan W. Mazer, "Properties of recycled gypsum from gypsum plasterboards and commercial gypsum throughout recycling cycles," *J. Clean. Prod.*, vol. 183, hal. 1314–1322, 2018, doi: 10.1016/j.jclepro.2018.02.189.

[5] H. Fathurrahman, A. Neolaka, dan R. Arthur, "Comparison of Pineapple Leaves (Ananas Comosus L. Merr) Gypsum Board On Commercial Gypsum Board Seen From Physical and Mechanical Properties Based On Sni Specification of Panel or Gypsum Board 03-6384-2000," vol. 3, hal. 121–130, 2020.

[6] P. J. Callus, A. P. Mouritz, M. K. Bannister, dan K. H. Leong, "Tensile properties and failure mechanisms of 3D woven GRP composites," *Compos. Part A Appl. Sci. Manuf.*, vol. 30, no. 11, hal. 1277–1287, 1999, doi: 10.1016/S1359-835X(99)00033-0.

[7] M. Pankow, B. Justusson, M. Riosbaas, A. M. Waas, dan C. F. Yen, "Effect of fiber architecture on tensile fracture of 3D woven textile composites," *Compos. Struct.*, vol. 225, no. January, hal. 111139, 2019, doi: 10.1016/j.compstruct.2019.111139.

[8] N. Tableau, Z. Aboura, K. Khellil, F. Laurin, dan J. Schneider, "Multiaxial loading on a 3D woven carbon fiber reinforced plastic composite using tensile-torsion tests: Identification of the first damage envelope and associated damage mechanisms," *Compos. Struct.*, vol. 227, hal. 111305, 2019, doi: 10.1016/j.compstruct.2019.111305.

[9] S. Prasojo, S. M. B. Respati, dan H. Purwanto, "Pengaruh alkalisasi terhadap kompatibilitas serat sabut kelapa (Cocos Nucifera) dengan matriks polyester," *J. Ilm. Cendekia Eksakta*, vol. 2, no. 2, hal. 25–34, 2018.

[10] J. Diniarto, "Analisis Struktur Material Laminasi Untuk Lambung Kapal Kayu Tradisional," hal. 46, 2011.

[11] A. K.Kaw, *Mechanics of Composite Materials*, First edit. America, 1997.

[12] A. Nurhidayat dan D. D. Susilo, "Pengaruh Fraksi Volume Pada Pembuatan Komposit Hdpe Limbah- Cantula," *Program. Pascasarjana. Tek. Mesin Univ. Sebel. Maret Surakarta*, vol. 14, no. 02, hal. 1–70, 2013.

[13] w K. H. Altenbach, J. Aitenbach, *Mechanics of Composite Struct[1] w K. H. Altenbach, J. Aitenbach, Mechanics of Composite Structural Element, First edit. Germany, 2004.ural Element*, First edit. Germany, 2004.

[14] L. M. RACHMAWATI, "Pengolahan Citra Digital untuk Identifikasi Void pada Permukaan Komposit dan Pengaruh Void Tersebut Terhadap Sifat Mekanik Komposit," Universitas Telkom, 2020.

[15] N. Nuryati, R. R. Amalia, dan N. Hairiyah, "Pembuatan Komposit Dari Limbah Plastik Polyethylene Terephthalate (Pet) Berbasis Serat Alam Daun Pandan Laut (Pandanus tectorius)," *J. Agroindustri*, vol. 10, no. 2, hal. 107–117, 2020, doi: 10.31186/j.agroindustri.10.2.107-117.

[16] H. Wardhana dan N. H. Haryanti, "Variasi Komposisi Serat Purun Tikus (Eleocharis dulcis) dan Waktu Perendaman KMnO4 terhadap Sifat Fisik Komposit Papan Semen," *Semin. Nas. Tah. VI*, hal. 30–38, 2019.


9 772621 489007


9 772621 021009